LIGHT COLLECTION EFFICIENCY SIMULATIONS OF THE XENON1T EXPERIMENT AND COMPARISON TO DATA

MASTER THESIS

Lutz Althüser

Westfälische Wilhelms-Universität Münster
Institut für Kernphysik
AG Prof. Dr. C. Weinheimer

First Referee: Prof. Dr. C. Weinheimer
Second Referee: Dr. M. Selvi

Münster, November 2017

Declaration of Academic Integrity

I hereby confirm that this thesis on **Light Collection Efficiency simulations of the XENON1T experiment and comparison to data** is solely my own work and that I have used no sources or aids other than the ones stated. All passages in my thesis for which other sources, including electronic media, have been used, be it direct quotes or content references, have been acknowledged as such and the sources cited.

Münster, 6. November 2017 _____

I agree to have my thesis checked in order to rule out potential similarities with other works and to have my thesis stored in a database for this purpose.

Münster, 6. November 2017 _____

Contents

1 Introduction

Over the last 100 years improved the understanding of how our universe is structured and composed by observations in cosmology and astronomy, revealing an increasing number of evidence that only 5 % of the universe is made from baryonic matter. While baryonic matter can be described by the standard model of particle physics, the contribution of 25 % of the mass-energy content of the universe is made from a new form of non-luminous and non-baryonic matter, the *dark matter*. The remaining 70 % is due to dark energy. The weakly interacting massive particles (WIMPs) constitute one class of dark matter particles. Their direct detection is the goal of many experiments around the world using the interaction of WIMPs and ordinary matter. However, none of these experiments could detect WIMPs so far. The final identification and characterization of a dark matter particle would reveal new insights into the evolution of the universe and expand the understanding of physics beyond the standard model.

The international XENON *Dark Matter Project*, located deep underground in the Laboratori Nazionali del Gran Sasso (LNGS) in Italy, is designed to detect WIMPs using dual phase xenon Time Projection Chambers (TPCs) in the prior experiments XENON10 and XENON100 as well as in the current development stage XENON1T. In this stage, the TPC is the first WIMP detector operating with a liquid xenon target mass above the ton-scale, utilizing 3.2 t in total and 2 t in the target volume. The XENON1T experiment started to take science data in November 2016 and published with 34.2 live days of data the most stringent exclusion limits on the spin-independent WIMP-nucleon interaction cross section for WIMP masses above $10\,\mathrm{GeV/c^2}$. Interactions of WIMPs with the xenon target produce scintillation light and ionization charges. Both signals are measured with photomultiplier tubes (PMTs), converted to digital data and processed by the Processor for Analyzing XENON (PAX).
Simulations of the estimated background level and WIMP-nucleon cross section sensitivity were important during the research and development phase, including a complete model of the detector. This detailed model was generated in GEANT4 and made up the base of the full Monte Carlo (MC) chain. The full chain consists of several software stages and allows to simulate the actual detector response. Events simulated by Geometry and Tracking (GEANT4) are converted to electronic signals of the PMTs and stored in the same way as measurements.

This work will validate and improve the full XENON1T MC chain with a main focus on optical simulations in comparison to the response of the actual experiment using a ^{83m}Kr calibration source. This improvement will have influence on further simulations and data processing. The position reconstruction methods used in the data processing are based on photon detection probabilities obtained by optical simulations.
The second chapter will introduce the field of direct dark matter detection, followed by a presentation of the XENON *Dark Matter Project* which includes a description of the dual phase TPC working principle in general as well as used in XENON1T.
Chapter four will give an overview of the GEANT4 package and its application for optical simulations. The implemented detector design and simulation models with implications on the optical response of the modeled detector are discussed. An investigation of the dependence of optical simulations on various material properties is performed. These dependencies are used in chapter five to improve the optical simulations. Prior simulations were based on assumptions made before the experiment was assembled in 2015. This work will consider the data taken by the XENON1T experiment between November 2016 and August 2017, which allows to obtain the actual optical response of the detector. A direct comparison of optical simulations and the actual optical response is presented, revealing the necessity of improving the simulations by fitting optical parameters to calibration data.
The sixth chapter will focus on the generation of per-PMT Light Collection Efficiency (LCE) maps with the fitted optical parameters, that are used in the full MC chain to distribute photons. An introduction to the full simulation will be given and its performance will be determined by comparing to data measurements, which are previously used to fit the optical parameters.
A new approach of simulating S2 photons will be motivated in the last chapter. This will allow further simulations to imitate the actual S2 generation as motivated by measurements and electric field models.

2 Direct dark matter detection

This chapter will introduce the concept of dark matter, including a selection of evidence in astronomy and cosmology. While this work will focus on direct detection of WIMPs, other particle hypotheses are also tested by trying to produce dark matter particles in accelerators (production) and searching for signals from annihilation products (indirect). Possible direct detection methods are discussed with considerations of the WIMP signature in corresponding experiments. The last section will introduce the XENON Dark Matter Project, an direct detection experiment utilizing the largest liquid xenon dual phase Time Projection Chamber.

2.1 Evidence for dark matter

First evidence for dark matter were reported in 1922 by Kapteyn [2] and 1932 by Oort [3]. They were studying the motion of astronomical objects and found that the mass of these objects must be greater than what was observed before. The term *dark matter* was introduced 1933 by Fritz Zwicky [4] who has used the brightness and number of galaxies in the Coma Cluster to estimate a mass distribution and compared it

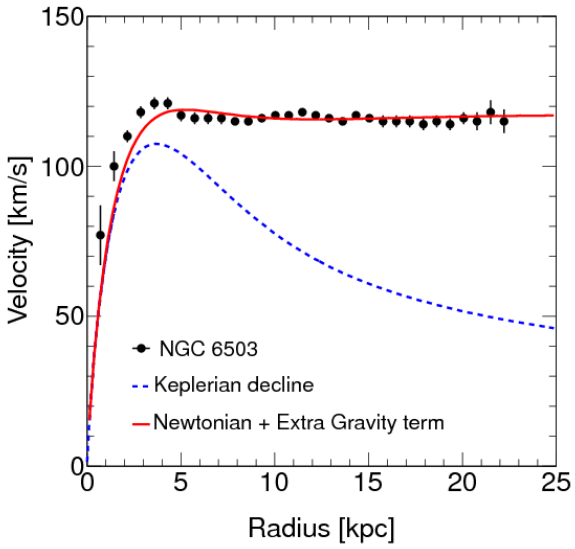

Figure 2.1: The predicted relationship between the galactic rotation speed v and the distance r from a combined influence of the Newtonian force and gravitational force as generated by a dark matter halo. [1]

to the result based on the motion of galaxies near the edge. He concluded that the high velocities of these galaxies near the edge of the cluster cannot be explained by taking only the visible matter into account and that unseen matter with a certain mass and gravitation attraction must form the cluster. Further evidence from galaxy rotation curves is given by the observations of Vera Rubin [5], stating that the rotational velocities of stars v in galaxies are not following the expected Keplerian decline $v \propto \frac{1}{\sqrt{r}}$ for high radii r. The velocity is measured as approximately constant with increasing radius which could be explained by introducing a uniformly distributed dark matter halo that extends beyond the edge of the visible galaxy and dominates the total mass as seen in figure 2.1.

Zwicky already considered that galaxies could act as gravitational lenses [7] where the observer can see multiple images (strong lensing) or a distorted image of the object (weak lensing) behind the gravitational lens. This effect takes place when a gravitational field by a massive object is in the line between observer and object and is able to bend the light along its path. This observed deformation of the object can be used to reconstruct the gravitational potential of the lens and thus the mass including dark matter. The term microlensing is used when no distortion of the object is visible but the amount of received light is a function of time (known as *microlensing*

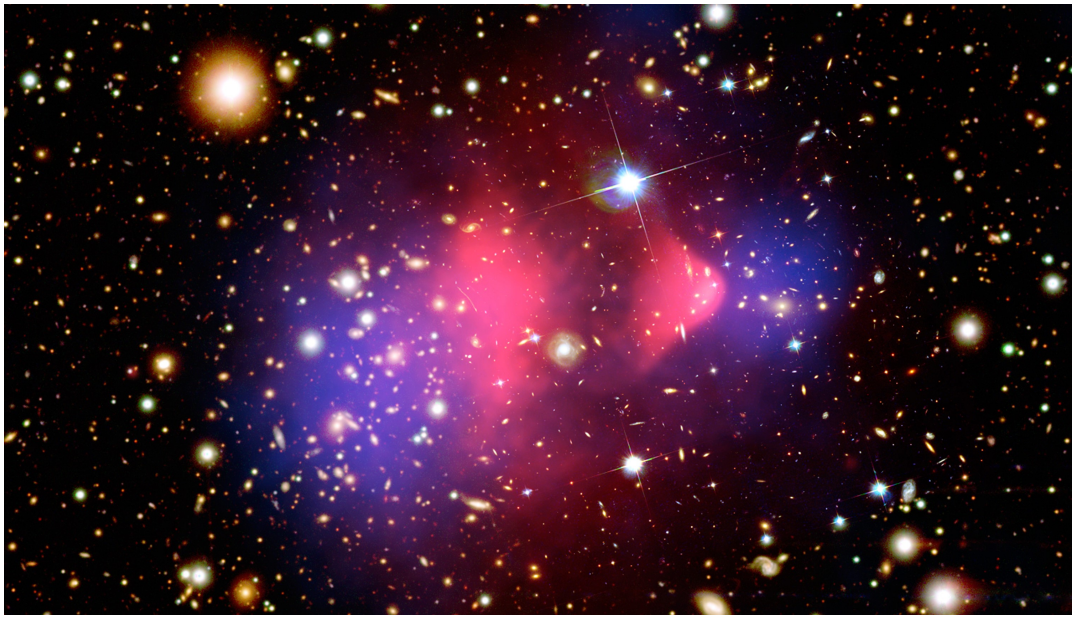

Figure 2.2: Composited image of the Bullet Cluster from X-ray, optical and lensing maps. An optical image from Magellan and the Hubble Space Telescope shows the galaxies in orange and white. Hot gas (pink) detected by Chandra in X-rays contains most of the visible or baryonic matter. The bullet-shaped clump on the right is hot gas from one cluster, which passed through the hot gas from the other larger cluster during the collision. The blue areas depict the concentration of mass, determined by analyzing the effect of gravitational lensing. [6]

lightcurve). A common example for gravitational lensing studies is the Bullet Cluster (1E0657-558) given in figure 2.2.

The Bullet Cluster was formed by the collision of two galaxy clusters and is studied with several approaches. The visible light image is taken by the Magellan and Hubble Telescopes, the pink colored hot gas is observed by the Chandra X-ray Observatory and the blue areas depict the mass as analyzed by gravitational lensing [8]. After the collision of the smaller galaxy passing trough the larger one, the hot gas in each cluster was slowed down and formed the bullet like shape, while the mass concentration (blue) was not influenced. This leads to a separation of the visible and not visible centers of mass and implies that the not visible or dark matter is not interacting with itself or the gas except with gravitational force. These lensing studies show, that dark matter is mainly composed by non-baryonic matter. This assumption is strengthened by the cosmic microwave background (CMB) power spectrum obtained with the satellite missions WMAP [9] and PLANCK [10]. They measured the temperature anisotropies in the CMB which allows to study the universe back to the recombination epoch, about 379 000 years after the Big Bang.

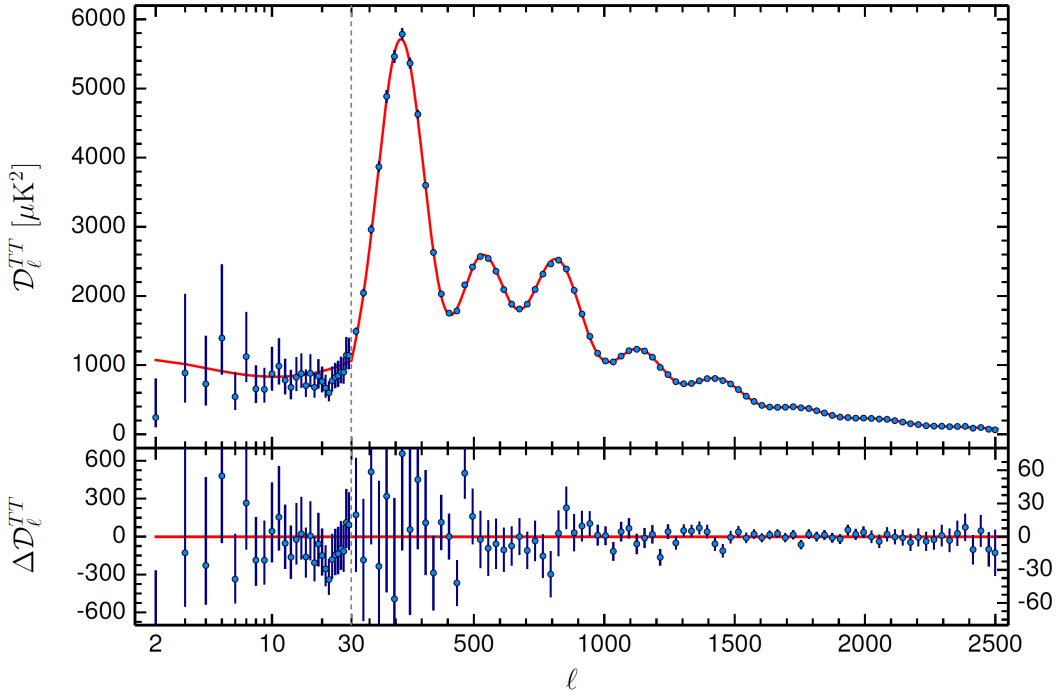

Figure 2.3: Planck 2015 power spectrum analysis by multipole moment l with fitted ΛCDM model and corresponding fit residuals. The error bars represent 1σ-uncertainties. [10]

The peak structure of the CMB power spectrum, showed in figure 2.3, generated by oscillations of baryons and photons in a gravitational potential, can exhibit information about the universe composition. The spectrum is therefore fitted with the Λ cold dark matter (ΛCDM) cosmological model that gives an estimation of the baryonic matter, dark matter and dark energy distribution. A detailed description of the CMB

and ΛCDM model can be found in [10]. The showed spectrum corresponds to the densities of $\Omega_{\mathrm{DM}} = 0.265$, $\Omega_{\mathrm{baryon}} = 0.049$ and $\Omega_{\Lambda} = 0.686$. [10]

These observations lead to specific description of dark matter where it is composed of weakly interacting massive, neutral, not visible and non-relativistic particles. Possible candidates like the sterile neutrinos [11] and axions [12] are not discussed within this thesis.

2.2 Dark matter detection channels

The most promising dark matter candidate, the WIMP, which is not part of the standard model, is assumed to be stable, neutral and massive as observed in the given evidence. Its mass can range from GeV/c^2 to TeV/c^2, depending on the given model. All of them have in common, that WIMPs are described as thermal relic particles that were in thermal equilibrium with the plasma in the early universe but freezed out when the temperature of the plasma dropped below the assumed WIMP mass [13].

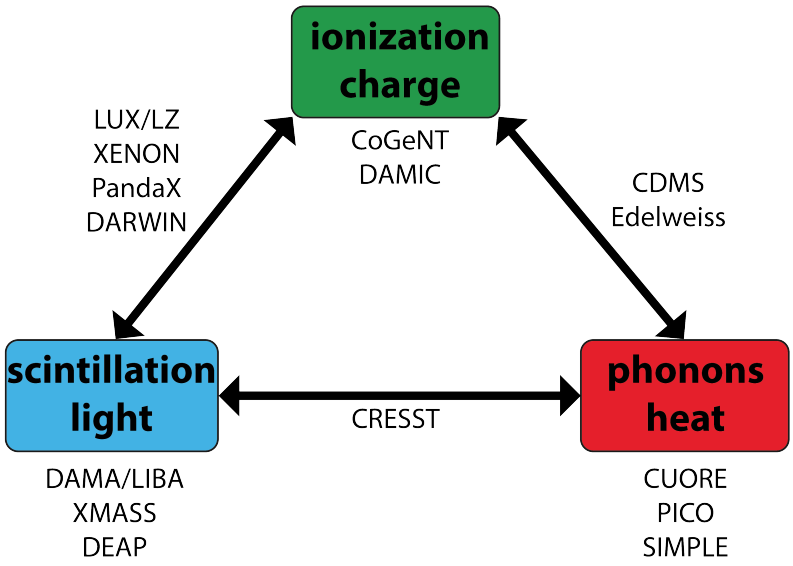

Figure 2.4: Sketch of the three most common ways to directly detect dark matter as described by the WIMP model. Examples of experiments for each signal channel are given, where the experiment on the arrows exploits both channels.

The aim of direct detection experiments is to identify collisions between the dark matter, here WIMPs, and a detector target nuclei. Such collisions leads to nuclear recoils in the range of keV, which requires detailed knowledge on the signal signatures in the experiment. Possible signal signatures in direct detection experiments, described in [14], are the energy, time or direction dependence of the single scatter recoil spectrum. The dark matter particle exhibit such a low interaction strength so

that multiple collisions within the detector are negligible. Following [15], the recoil spectrum resulting from dark matter interactions can be written as:

$$\frac{dR}{dE}(E,t) = \frac{\rho_0}{m_\chi \cdot m_A} \cdot \int v \cdot f(\mathrm{v},t) \cdot \frac{d\sigma}{dE}(E,v) d^3v, \tag{2.1}$$

where m_χ is the dark matter mass, v the dark matter velocity, $\frac{d\sigma}{dE}(E,v)$ the dark matter differential cross-section and m_A the nucleus mass. Astrophysical parameters, the local dark matter density ρ_0 and $f(\mathrm{v},t)$, account for the WIMP velocity distribution in the detector, which is time dependent due to the revolution of the Earth around the Sun. The WIMP cross-section σ and m_χ are the two observables of dark matter experiments. In direct detection experiments, the most common approach is to measure the energy dependence of dark matter interactions as described in [14]. Numerous experiments around the world are using a selection of the main detection channels, scintillation, ionization and heat, as shown in figure 2.4, to directly detect dark matter particles. The XENON Dark Matter Project exploits the scintillation and ionization channels to search for WIMPs by using the liquid xenon (LXe) dual phase TPC as described in the next chapter.

3 The XENON Dark Matter Project

The XENON Dark Matter Project aims to directly detect WIMP dark matter particles with a liquid xenon (LXe) dual phase Time Projection Chamber (TPC). The first stage of the project was the XENON10 experiment in 2005. This small scale detector featured a target LXe mass of 14 kg (25 kg in total) and was built to test the possibility to realize a dual phase TPC. The experiment was located at the Laboratori Nazionali del Gran Sasso (LNGS) in a depth of 1400 m, equivalent to 3600 m of water. Due to promising results the project was continued to the next stage, XENON100, which utilizes a target mass of 62 kg (161 kg in total) and lead to competitive results in 2012. Therefore, the design of the XENON1T experiment started in 2010. The current stage is the largest LXe dual phase TPC in the world with a target mass of 2 t (3.2 t in total) and has started data taking in 2016.

Figure 3.1: Stages of the XENON Dark Matter Project with first predictions for XENONnT science run and the initial DARWIN project start in comparison.

The XENON1T experiment, shown in figure 3.2, consist of several subsystems, needed to operate the dual phase TPC presented within this chapter. A full overview of the subsystems in given in [16]. The TPC is mounted on a support frame inside of the water tank, which is used as an additional shielding and is equipped with photosensors to detect muons. The water provides shielding against γ rays and neutrons from natural radioactivity in the laboratory. It is also possible to use a belt system with holders to place radioactive sources or small instruments close to and around the TPC. The cryogenic system (*Cryogenics*) is located in the third floor and directly connected to the TPC with a vacuum-insulated pipe, in which the liquefied xenon gas runs back to the TPC. This pipe also hosts the high voltage and photosensors signal cables. The xenon gas or liquid can be stored in the *ReStoX* system (first floor), also used for recovery and filling in of xenon. It is capable of storing 7.6 t xenon in liquid or gaseous state within the 2.1 m sphere. Electronegative impurities, such as water, can be removed by the *Purification* system close to the *Cryogenics*. The amount of natural krypton in the xenon can be removed by *Cryogenic Distillation*

with a distillation column, located in the first and second floor. The data acquisition, electronics and computing is installed in the second floor, next to the shifters office.

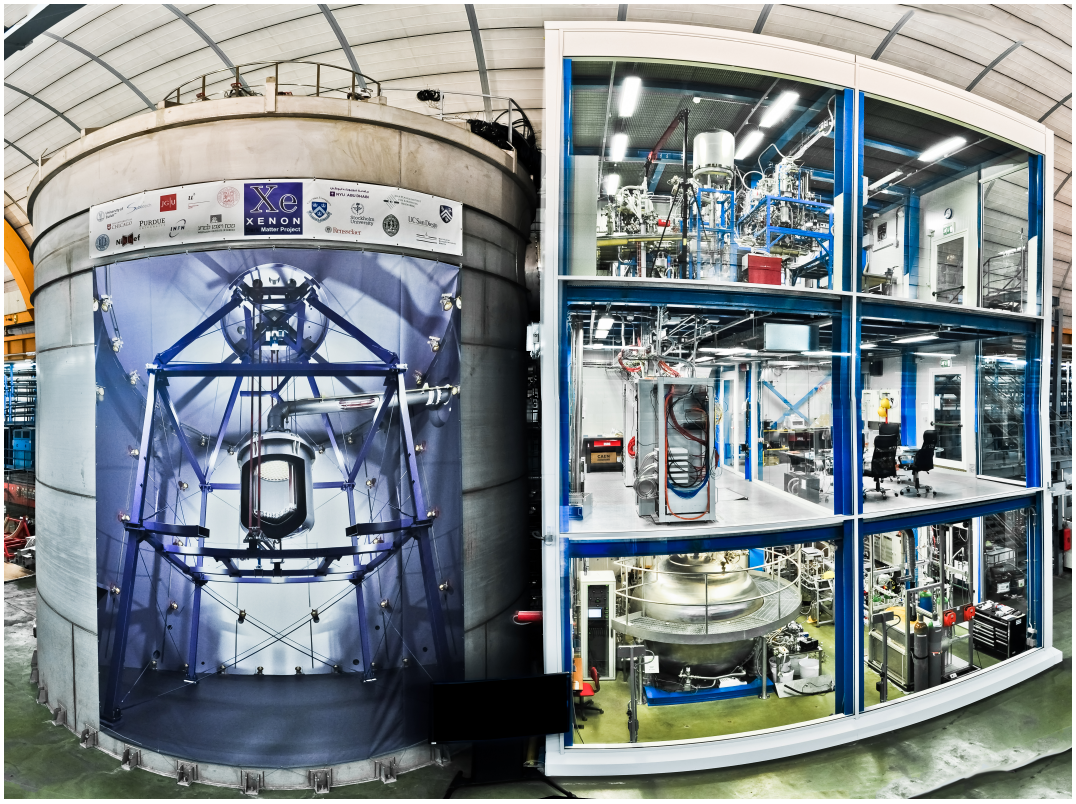

Figure 3.2: Overview of the XENON1T experiment in Hall B of the Laboratori Nazionali del Gran Sasso (LNGS). The LXe dual phase TPC is mounted on a support frame in the water tank (left) next to the support building (right). The building hosts all subsystems like the *ReStoX* (fist floor), the *Cryogenic Distillation* (first and second floor), *Computing* (second floor) and *Cryogenics* (third floor).

3.1 Dual phase xenon Time Projection Chamber detection principle

The LXe dual phase xenon TPC is the most important part of each XENON experiment and follows the detection principle as illustrated in figure 3.4.

A particle entering the LXe volume can scatter off the xenon nuclei or interact with the atomic electrons, generating ionization and scintillation signals. The mechanism for LXe is shown in figure 3.3, where Xe^{+} is an ionized atom, Xe^{*} and Xe^{**} are the first and second excited levels, Xe_2^{*} is an excimer (excited dimer) and $h\nu$ is the vacuum ultraviolet (VUV) scintillation photon. The generation of scintillation light ends for both channels in a de-excitation of Xe molecules. Therefore, the light is generated by dimers of a different energy level configuration, which leads to scintillation light that is not re-absorbed by Xe atoms, making the xenon transparent to its own

scintillation light. The emitted light has a broad spectrum (Full width at half maximum (FWHM) of 14 nm) with a typical wavelength of 178 nm which corresponds to a 7 eV photon. The average energy that is needed to produce one scintillation photon is given as the W-value. Typical W-values for LXe and gaseous xenon (GXe) are $W_{LXe} = (15.6 \pm 0.3)\,\text{eV}$ and $W_{GXe} = 22\,\text{eV}$. [17]

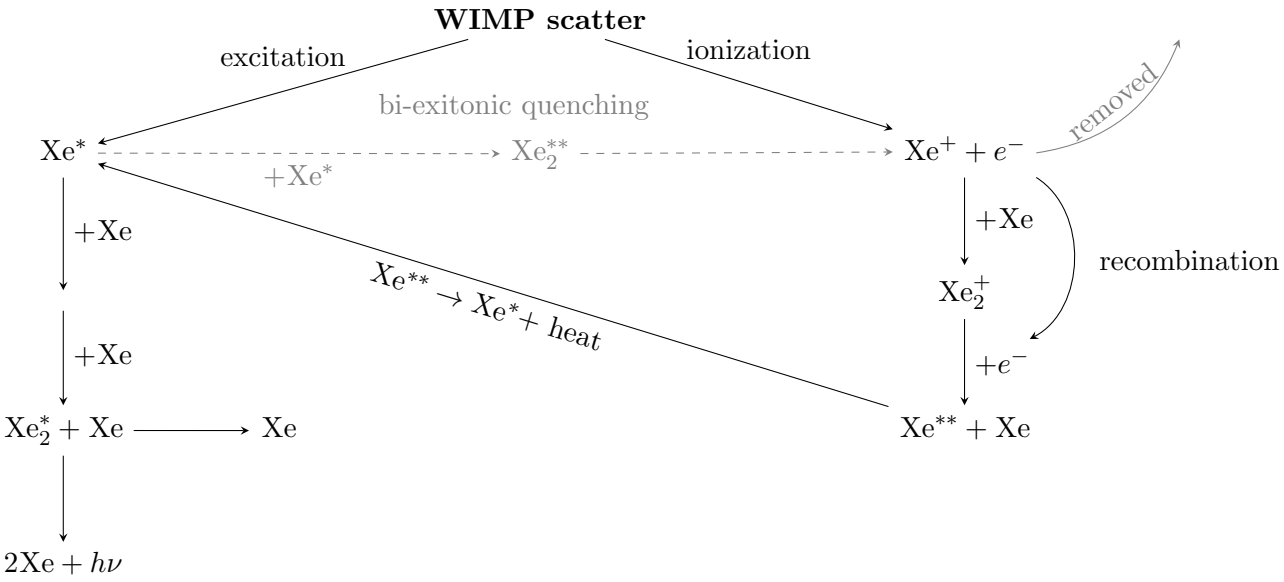

Figure 3.3: Scintillation mechanism in LXe. The gray reaction describes the bi-exitonic collisions in which two excitons collide giving an electron with a certain kinetic energy that recombines producing only one photon. Bi-exitonic quenching only appears in high excitation densities, as described in [18].

The scintillation mechanism of LXe can be split in two separate detection channels by suppressing the recombination and extracting the electrons with an electric field. The first detection channel, photons from the scintillation signal (S1), is observed by photosensors above and below the target mass (LXe and GXe). The second signal, the ionization signal, is generated by amplification of the electrons. A first electric field (E_{drift}) which drifts the electrons towards the LXe/GXe interface is applied in the LXe region, while a second stronger field ($\text{E}_{\text{extraction}}$) extracts these electrons into the gas phase. Here, the electrons create a second light signal (S2) due to electroluminescence, which is thus proportional to the number of initial electrons. The two channel readout allows a three-dimensional position reconstruction, where the x-y-position can be determined by the S2 light pattern in the photosensors at the top array and where the z-position is reconstructed by measuring the time between the S1 and S2 signal. This difference depends on the drift velocity of the electrons in the electric field. Another important feature of dual phase detectors is the background discrimination by using the S1 and S2 signals. It is assumed that WIMPs produce nuclear recoils (NR) while most of the background radiation produces electronic recoil (ER). [19] In case of NR,

the incident particle is interacting with the atomic nucleus and the momentum is transfered to the nucleus as a whole, while for ER the particle is interacting with the electrons of xenon. Due to the higher recombination rate of nuclear recoils than for electronic recoils is a lower S2 and a higher S1 signal for WIMPs expected. The S2/S1 ratio implies an anti-correlation between ionization and scintillation signal.

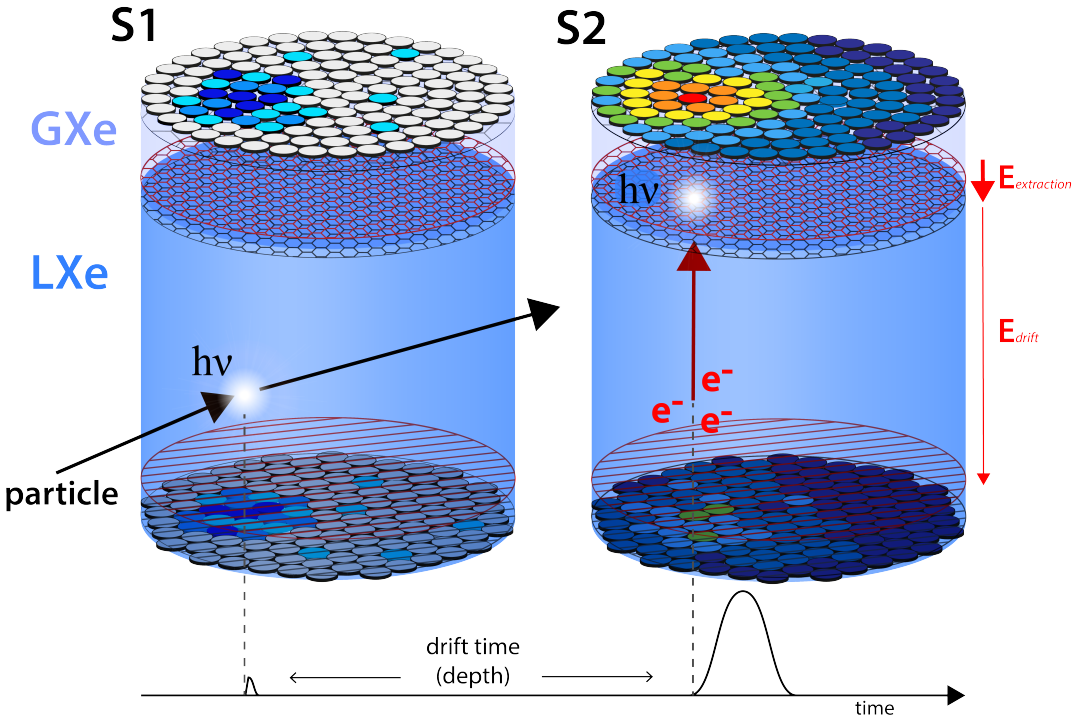

Figure 3.4: Working principle of the XENON1T LXe dual phase TPC. The TPC is equipped with 248 photosensors in a hexagonal and circular pattern. On the left side, the generation of the prompt scintillation signal (S1) by an incident particle scattering off the LXe, which gives a broad light signal on both photosensor arrays. On the right side, Electrons (e^-) from the ionization signal drift in the electric field E_{drift} from the interaction position towards the LXe/GXe interface. These electrons are extracted from the LXe by a second stronger electric field ($E_{extraction}$). Both electric fields are generated by fife meshes, from which one is placed in front of each photosensor array to protect them. The second scintillation signal (S2) is generated due to electroluminescence of the extracted electrons and exhibits a localized signal pattern on the top array, while the bottom array is uniformly illuminated. The position of the interaction can be determined by the depth (z), given as the drift time of the electrons between the two scintillation signals, and the S2-signal pattern (x-y).

3.2 XENON1T detector design

The XENON1T TPC, as described in [20], is the largest LXe dual phase TPC with a cylindrical detection volume of 97 cm length and 96 cm diameter, containing 2 t of LXe target where the light and charge signals are generated as described above. The volume of LXe in which an interaction can occur is called active region. A technical drawing of the TPC is given in figure 3.5 and an overview of the full XENON1T setup is shown in figure 3.2. The detection or active volume is enclosed by 47 polytetrafluoroethylene (PTFE) panels which are optimized to reflect VUV light. Two electric fields, the drift field (E_{drift}) and the extraction field ($E_{extraction}$), that are used to extract the ionization signal from the LXe are applied by electrodes (meshes). Two electrodes are placed in front of the photosensor arrays to protect them from the applied field, which is generated between the cathode (red mesh in the bottom TPC), gate mesh (gray hexagonal mesh) and anode (red hexagonal mesh). The uniformity of the overall electric field is ensured by 74 field shaping electrodes made of low-radioactivity oxygen-free high thermal conductivity (OFHC) copper, interconnected with a resistor chain. Further information about the mesh shape and material is given in section 4.2.2. The height of the LXe above the gate is defined by the diving bell made of stainless steel (SS) which is controlled by a vertically-adjustable gas-exhaust tube and ensures a stable liquid-gas interface.

The TPC is equipped with 248 Hamamatsu R11410-21 PMTs with a diameter of 76.2 mm installed in two different PMT pattern for the top and bottom array which

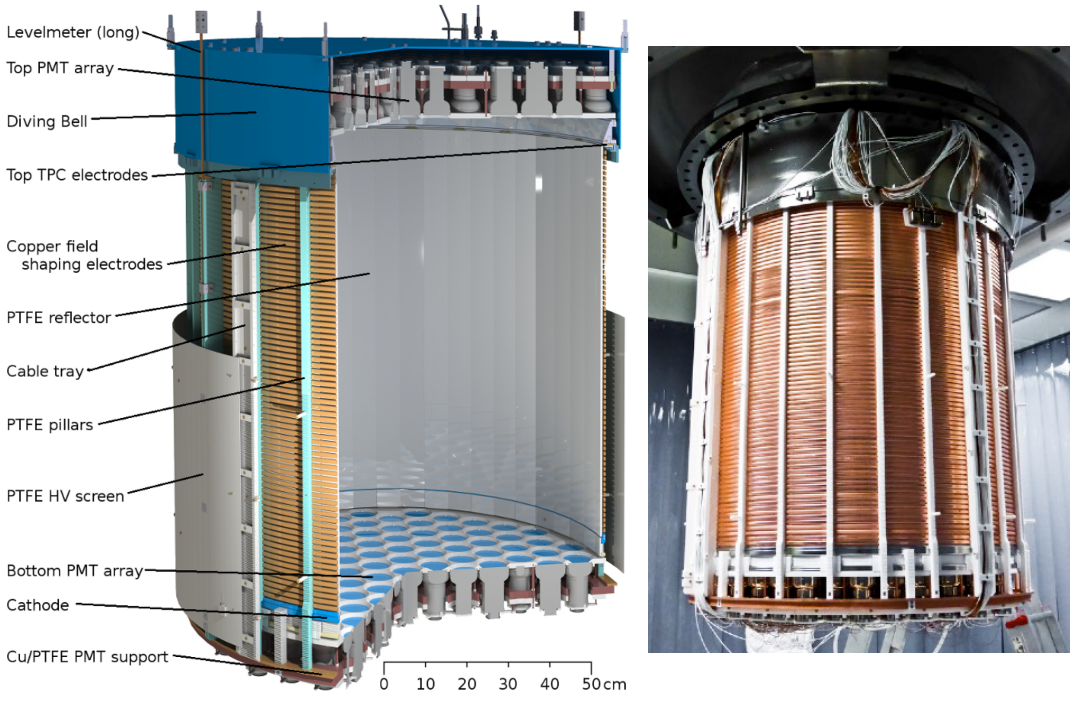

Figure 3.5: Technical drawing of the XENON1T TPC (left) and the actual TPC in the clean room inside of the water tank (right). [16]

achieves a better radial position reconstruction in the radially top array of 127 PMTs and a maximized scintillation light collection in the tightly packed bottom array of 121 PMTs. These PMTs are chosen to have a high quantum efficiency (QE) and a low background rate as described in section 4.2.3. Surrounded by a double-walled cylindrical SS cryostat is the TPC installed in a SS support frame inside the 10 m height water tank, as seen in figure 3.2.

An upgrade of the XENON1T TPC to the future XENONnT TPC can be achieved by replacing the inner cryostat with a bigger one. The outer cryostat was built such that a new inner cryostat with 476 PMTs will also fit. This upgrade will increase the active LXe target volume by a factor of three to 6 t (7.5 t in total).

4 Optical simulations of the XENON1T detector

Simulations of the detector response are essential for the development steps from the initial design and material selection to commissioning and during the science run. Each simulation is performed with a different level of detail and scope. While early simulations focus on average estimations of background radiation and signals, later simulations, e.g. for a *science run*, aim to reproduce the detector signals as closely as possible, aiming for an understanding of each interaction occurring in the detector and to correct the data handling and analysis.

Therefore, the XENON1T simulation includes a detailed description of the detector geometry. Which allows to perform studies like the estimation of the internal backgrounds or the optical response of the actual detection volume, as presented in this chapter. The Monte Carlo (MC) methods or Monte Carlo experiments are a class of algorithms that are based on randomized sampling to determine an answer for complex problems based on statistics. These simulations are used for modeling systems with high degrees of freedom in which other mathematical methods are not suitable. For physics-related problems, several simulation toolkits based on Monte Carlo algorithms have been developed. The XENON1T MC has been realized with GEANT4 and is extended with own algorithms to fully describe the detector response. This also includes a *waveform* generation from the GEANT4 output featuring electronic noise and other effects of the photo sensors, discussed within this thesis.

This chapter will focus on the optical simulations of XENON1T, presenting the GEANT4 package and describing the actual simulated detector design, which also includes information about the *surface models* in GEANT4 and simulations of PMTs. In the end, optical simulations of the XENON1T detector are performed investigating the influence of various simulation parameters on the light collection of the PMTs.

4.1 GEANT4 simulation package

The XENON1T simulation is based on the GEANT4 simulation toolkit by Cern [21]. It is invented as a platform for "the simulation of the passage of particles trough matter" [21] and is used in the fields of high energy physics, nuclear experiments, medical solutions, accelerator and space physics as well as for direct detection dark matter experiments.

The XENON1T simulation toolkit is built with respect to several use cases. The following optical photon simulations are generated with GEANT4 version 9.5, which is currently used for all simulations. A new *PhysicsList* for the use with GEANT4 version 10.3 is also developed and tested during this thesis, but not used in favor of a directly comparable simulation. Other features like a Noble Element Simulation Technique (NEST) mode that includes the signal calculation are described later (see section 6.1).

In general, a GEANT4 simulation implementation is divided into the main parts of handling the detector *geometry*, *tracking* and *propagating particles*, detector response of *sensitive volumes*, *run management*, *visualization* and an *user interface*. While GEANT4 can precisely simulate any particle propagating in the total area, the algorithm is not optimized for optical simulations. The propagation of a particle and also photons on a Track is divided in steps, in which a particle may encounter several detector parts. An intersection of the particle with sub-volumes is tested for each mother volume with the smart voxel technique [21] where virtual division along a chosen axis is performed and subdivisions through the same volumes are gathered into one. This division has to be done in two or three cartesian axis depending on the refinement of the volumes. The smart voxels are computed during the initialization and thus allow a complex detector geometry, that will be described in the section. Several solutions for only optical simulations with an improved tracking algorithm are available but not considered in favor of an unified simulation for all use cases. This ensures also the validation of the optical parameters in simulations of the background estimation or for calibration sources.

4.2 XENON1T detector design

The implementation of the detector is done with respect to the possibility of performing optical and background simulations of every component and material. Therefore, the MC geometry is built from technical drawings of each component. The implementation is also reconciled with actual detector part measurements and hierarchically structured by the containing parts. Several differences of the MC geometry from the real detector are found during this thesis, as well as wrong refraction index values for the top meshes thin disks which have mainly influenced S2 simulations. These

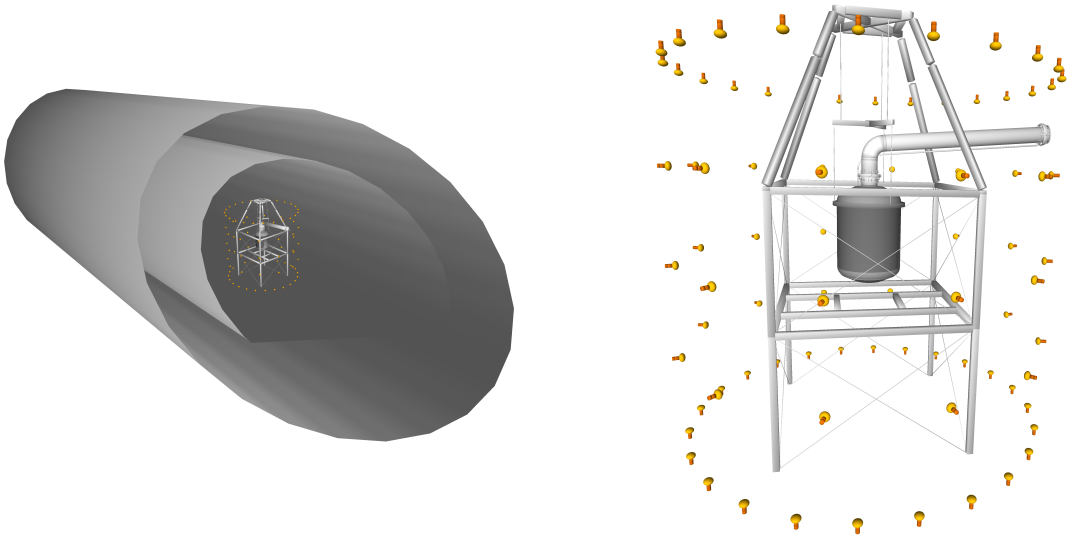

Figure 4.1: Implementation of the XENON1T detector geometry in GEANT4. The rock of the Gran Sasso d'Italia is considered as well as the concrete of the hall B of the Laboratori Nazionali del Gran Sasso LNGS (left). Some parts of the detector design are implemented to be not visible (right), therefore the size of the water tank can only be assumed by the outer Muon Veto PMTs colored in orange and yellow. All components of the detector inside the water tank, like the support structure and pipes, are fully included.

adjustments are already included in the XENON1T MC version 1.0.1, used in the following unless noted different.

Beginning with the Gran Sasso d'Italia rock (*Rock*, name of the detector part in GEANT4), the detector construction includes also the concrete (*Concrete*) of the underground laboratory in the Laboratori Nazionali del Gran Sasso (LNGS), as seen in figure 4.1. The hall B in which the XENON1T experiment is located has a length of 100 m, a diameter of 20 m and a height of 18 m. The XENON1T detector also includes an active Muon Veto which consist of a water tank (*WaterTankTube*) containing 740 m^3 deionized purified water, equipped with 84 PMTs (Hamamatsu R5912ASSY, named *WaterPMT**). The water tank has a height of 10.2 m and a diameter of 9.6 m. The cryostat is installed with a SS support structure that can be converted into a cleanroom. The materials in the simulation are implemented with their measured material composition and colored with an individual color applied on all components.

The outer cryostat (*SS_OuterCryostat*) shown in figure 4.2 is connected with a vacuum-insulated cryogenic pipe and a smaller (*Pipe_SS*) one for high voltage (HV) feedthroughs to the support building outside the water tank. The cryogenic pipe contains smaller pipes for gas circulation, PMT signal and HV supply cables. The pipes as well as the cryostat are made of low radioactive SS and are vacuum-insulated to separate from external environment temperature. The cryostat is built as a double vessel structure to insulate the LXe filled into the inner cryostat (*SS_InnerCryostat*) with a vacuum

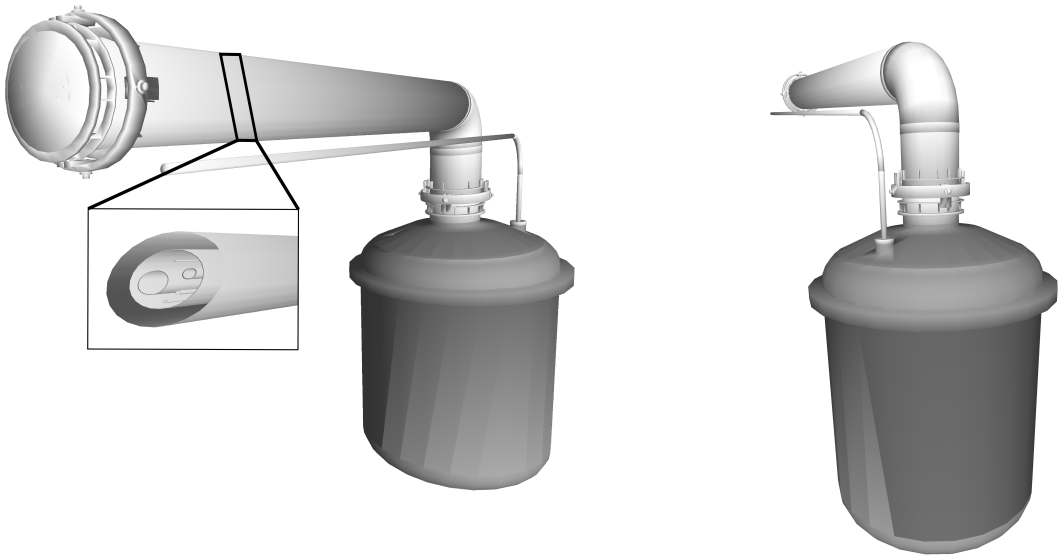

Figure 4.2: Implementation of the outer cryostat connected to the support building with a 6 m long vacuum-insulated cryogenic pipe, through which all connections to the TPC are made. A smaller additional pipe hosts the high voltage connection of the meshes.

jacket from the water tank. Both, the inner and outer cryostat, have the same geometrical structure, a central cylindrical body enclosed with two domes on top and bottom. The outer cryostat has a thickness of 5 mm, an outer central diameter of 1630 mm and a height of 1687 mm, while the inner cryostat has an outer central diameter of 1110 mm and a height of 1420 mm. The bottom domes are directly connected to the cylindrical bodies and the top domes are attached with flanges, which allows to exchange the inner cryostat and upgrade the XENON1T detector to XENONnT (see chapter 3).

Most important for the XENON1T experiment is the double phase TPC hosted inside the inner cryostat (see figure 4.3). The TPC is built to detect dark matter interactions in the LXe target volume of about 2 t. This volume is designed to maximize the chance of detecting light and charge signals, which requires a light tight and highly reflecting chamber as well as a uniform electric field. The main chamber, which is called the TPC volume, is made of 24 interlocking PTFE panels with a thickness of 5 mm. This interlocking structure avoids the loss of photons through holes at LXe temperature after a shrinkage of 1.5 % [22] and is simplified in the MC simulation to a cylinder of 5 mm with a radius of 479 mm and a height of 967 mm after shrinkage. This active LXe TPC volume is enclosed on top and bottom by the gate mesh and cathode. Electrons in this region can drift in a well defined electric field towards the liquid-gas interface (2.5 mm above the gate mesh), where they will be extracted into the GXe region by a stronger extraction field. The PTFE cylinder above the gate mesh is

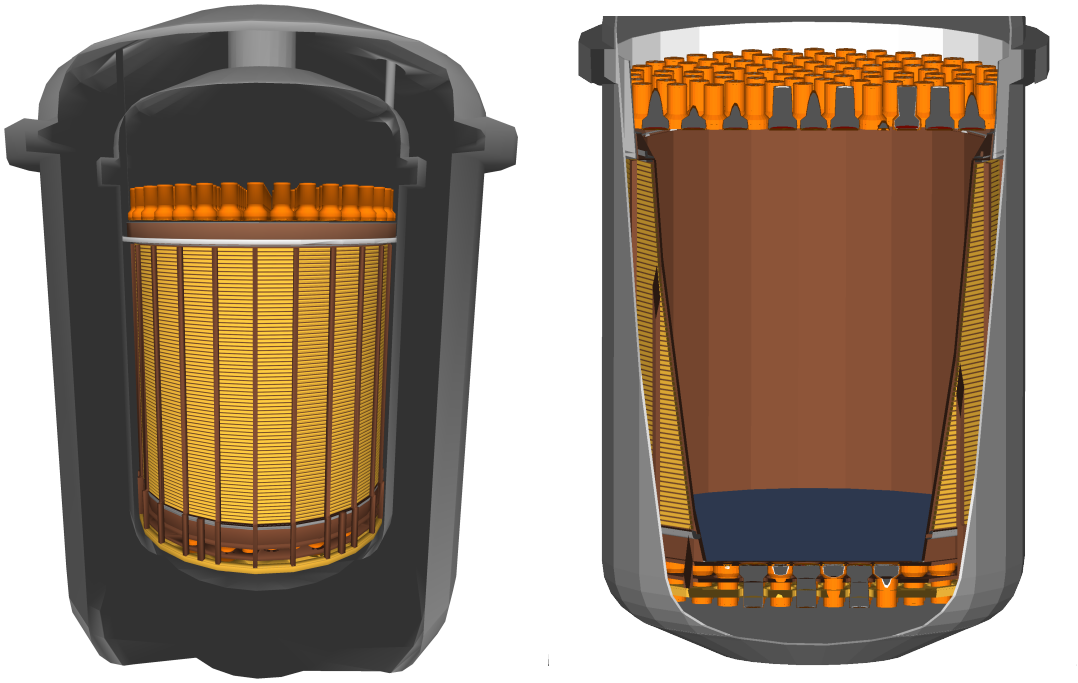

Figure 4.3: Direct view (left) on the XENON1T TPC with a top and bottom PMT array, a PTFE support structure (brown) and copper field shaping rings (yellow). The active LXe volume of the TPC is enclosed by a PTFE cylinder (right), the gate mesh (not visible, located right before the widening of the PTFE cyclinder on top) and cathode (blue disk).

widened towards the top PMT array in order to have a high S2 signal efficiency (see figure 4.5). The uniformity of the electric field along the drift region is generated by field shaping rings around the PTFE cylinder. These 74 thin copper rings are placed equally spaced along the vertical axis, see figure 4.3. The copper rings, the cathode and gate mesh are connected with a resistor chain, giving a uniform drift field in dependence of the mesh high voltage settings. The copper rings, held by an outer PTFE support structure, have a thickness of 5 mm and a height of 10 mm. The implementation of the physical electric field is not included in the GEANT4 simulation and can be studied with COMSOL Multiphysics® simulations.

4.2.1 Polytetrafluoroethylene surface model

PTFE is the main component of the XENON1T TPC and thus responsible for the amount of detected scintillation light. This material was chosen because of its high reflectivity for xenon scintillation light (178 nm with FWHM of 14 nm [23, 24]) and a manufacture process that yields to a highly radio-pure material [25, 26] with a low outgassing rate [27]. The strong bound between carbon and fluorine leads to a high stability for temperatures between −200 °C and 260 °C. PTFE which is immersed in LXe and kept at temperatures around −100 °C has a total reflectivity of more than 97 % [24, 28, 29, 30] at the wavelength of interest. The surface of PTFE, which is a

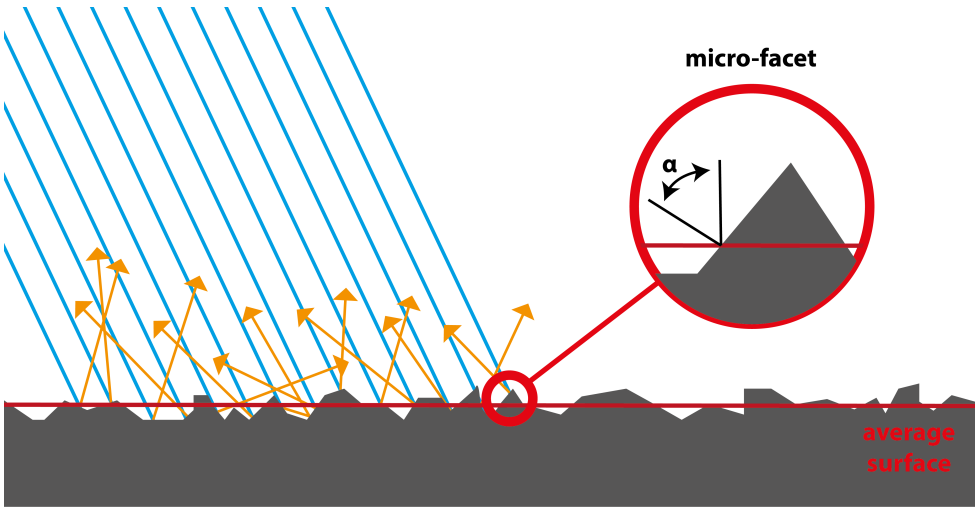

Figure 4.4: Sketch of a surface model used in GEANT4 defined by a *sigmaalpha* parameter, the standard deviation of the micro-facets orientation distribution. A micro-facet is randomly selected each time an interaction occurs and a specular reflection is thereafter calculated based on its orientation (adapted from [31]).

polished pressed powder, leads to mainly diffuse reflection as illustrated in figure 4.4. Additional information about reflectivity measurements of PTFE in vacuum, liquid and gaseous xenon can be found in [24].

The implementation of the PTFE surface model in GEANT4 is done with respect to measurements that report also a specular reflection component [24, 30]. The surface model is set to *Dielectric_dielectric* and *GroundBackPainted*, which defines the boundary processes in GEANT4 to be dependent on the wave length of each photon, the angle of incidence, (linear) polarization and the refractive index on both sides of the boundary. A photon that reaches the PTFE volume can be internally reflected, Fresnel refracted or Fresnel reflected. The *GroundBackPainted* surface finish adds the effects of spike reflection, lobe reflection, backscatter, lambertian reflection and absorption. The probabilities for these four reflection types must add up to 100% of the reflected light. One important design issue of the model is that GEANT4 assumes the four reflection type probabilities are constants and independent of the incidence angle. But a dependence of the incident angle is reported by [30] and [31], where the specular spike reflection becomes dominant for very high incident angles. The specular spike reflection is defined in a way that the photon is reflected about the average surface normal. This reflection is equivalent to a photon that would be reflected in a perfect mirror. For backscatter reflection, the photon is reflected back into the incident direction. In Lambertian reflection, the photon will be reflected with a Lambertian distribution probability around the average surface normal with a cosine distribution. The surface is assumed to consist of microscopic small surfaces (micro-facets) which are oriented around the average surface with a Gaussian distribution, as shown in figure 4.4. A *sigmaalpha* parameter defines the standard deviation of the

distribution of the micro-facets orientations. A micro-facet is randomly selected each time an interaction occurs and a specular reflection is thereafter calculated based on this micro-facet orientation. These surface models lead to diffuse lobe constant of 97 % and a specular lobe, specular spike and backscatter constant of each 1 %. It should be noted that only the total reflectivity has an influence on the total amount of photons collected, while the fraction of diffuse and specular reflection mainly has an impact on the amount of light seen by the top and bottom PMT arrays.

4.2.2 Mesh model

The XENON1T TPC uses three SS meshes, the cathode, gate mesh and anode, to generate the drift and extraction electric fields. The anode is placed 5 mm above the gate mesh with the LXe/GXe interface in the middle. The streamlines of both electric fields need to be closed to protect the PMT arrays, therefore a top and bottom screening mesh is implemented in front of each PMT array. All meshes are melted directly on electrode rings made of SS. The electrode rings are different in size depending on the mechanical tension that is applied by the various mesh geometries. This high mechanical tension is mandatory since any inhomogeneity of the distance will effect the field properties. This could cause a dependence of the S2 signal from the extraction point. Sagging of the meshes is neglected in the GEANT4 simulation. The electrode rings of all meshes are covered with PTFE, as seen in figure 4.5. This requires small Torlon® components to hold the PTFE in front of the anode electrode ring and also to prevent floating of the main chamber PTFE panels. Torlon® has a lower reflectivity than PTFE.

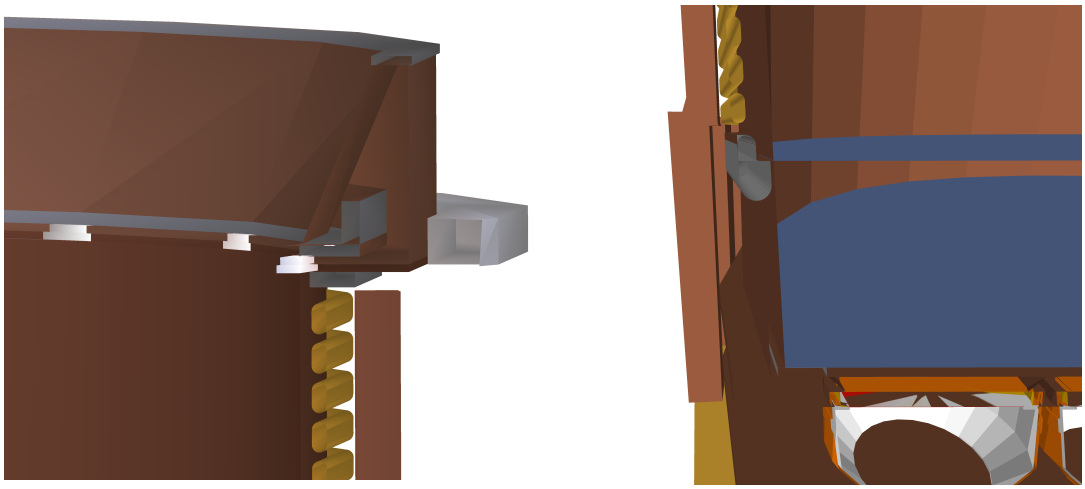

Figure 4.5: View on the upper (left) and lower (right) TPC part. The position of the top meshes is marked by the SS (gray) electrode ring structure covered by PTFE (brown). The PTFE around the anode is clamped with 23 Torlon® parts (silver). The bottom meshes are marked by blue disks directly connected to the bottom electrode rings.

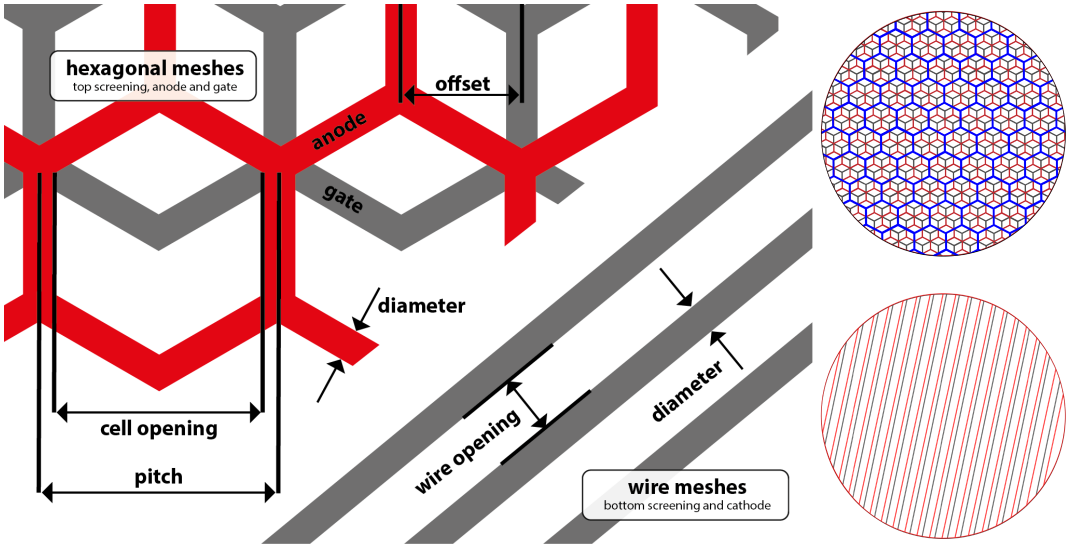

Figure 4.6: Definition of the two mesh types (left) and schematic representation of the mesh geometry in XENON1T. Right top, top screening mesh (blue), anode (red) and gate (gray). Right bottom, cathode (blue) and bottom screening mesh (red).

The upper meshes, anode, gate mesh and top screening mesh, have a hexagonal shaped structure, defined by its wire diameter and cell opening (see figure 4.6 and table 4.1). The anode and gate mesh are shifted in the x-y plane, so that the wire connection point of a anode cell is in the center of the gate mesh cell. This shift is motivated by COMSOL Multiphysics® simulation which showed that the extraction field in this configuration is most efficient and that the positions of the electrons is less effected [20]. Electrons that drift towards the upper meshes are focused by the gate mesh (see chapter 7). The bottom meshes, cathode and bottom screening mesh, are made of parallel wires with the same wire diameter and opening size (figure 4.6).

Table 4.1: Geometrical properties of the XENON1T meshes, as used in the MC simulation. The z-position is given as the middle of the meshes with 1.5 % PTFE shrinkage at LXe temperatures for all components of the main chamber (anode and top screening mesh are not connected to the PTFE). The position $z = 0\,\text{mm}$ is set to right below the gate mesh.

mesh name	mesh type	cell opening	wire diameter	z-position
top PMT windows	/	/	/	77.3 mm
top screening mesh	hexagonal	10.2 mm	0.178 mm	67.5 mm
anode	hexagonal	3.5 mm	0.178 mm	5.3 mm
LXe/GXe transition	/	/	/	2.6 mm
gate mesh	hexagonal	3.5 mm	0.127 mm	0.1 mm
cathode	wires	7.75 mm	0.216 mm	−967.3 mm
bottom screening mesh	wires	7.75 mm	0.216 mm	−1036.3 mm
bottom PMT windows	/	/	/	−1044.7 mm

Here is no complex mesh structure needed, since electrons will drift towards the upper meshes.

It is possible to switch between two different approaches of meshes implementations in the MC simulation, both are analytically equal. The default implementation uses thin disks with a fixed height of 0.2 mm for each mesh, see the blue disks in figure 4.5. These disks are generated in a way that their transparency match the real geometrical transparency [32]. Which is achieved by setting the refraction index of each mesh accordingly, allow to reduce the needed CPU time required by a detailed mesh structure. The dependence of the incident angle of a photon as given by following equation (4.1) is conserved as well as the geometrical transparency t for orthogonal photons ($\theta = 0$).

$$t(\theta) = \mathrm{e}^{-\frac{l(\theta)}{\lambda}} \tag{4.1}$$

Here, θ is the incident photon angle with respect to the mesh, l is the path length of the photon inside the mesh and λ a numerical factor defined by the initial geometrical transparency for orthogonal photons. The initial calculated and simulated [32] transparencies of the meshes are given in table 4.2. Both bottom meshes reveal the same transparency, since they have equal geometrical properties. The difference of 2.9 % between anode and gate mesh have its origin in the wire diameters, which also have a difference of 0.051 mm.

Table 4.2: Calculated transparency of each mesh with respect to the measured geometrical mesh properties as given in table 4.1.

mesh name	calculated transparency ($\theta = 0$)
top screening mesh	$(96.50 \pm 0.15)\,\%$
anode	$(89.8 \pm 0.4)\,\%$
gate mesh	$(92.7 \pm 0.5)\,\%$
cathode	$(97.2 \pm 0.3)\,\%$
bottom screening mesh	$(97.2 \pm 0.3)\,\%$

The second implementation of the meshes uses the actual geometry, as given by technical drawing and measurements. Geometrical properties used in the MC are given in table 4.1. The actual implementation of the meshes, developed within this thesis, is used for studies of the S2 scintillation simulation in chapter 7). In the simulation, the meshes are generated by using the G4VPVParameterisation GEANT4 class which creates copies of a specific volume using a given parameterization. The generated copies of the initial hexagonal cell are placed inside the TPC and cutted at the edges of the electrode rings. This procedure is repeated for each mesh, with parallel wires for the bottom meshes.

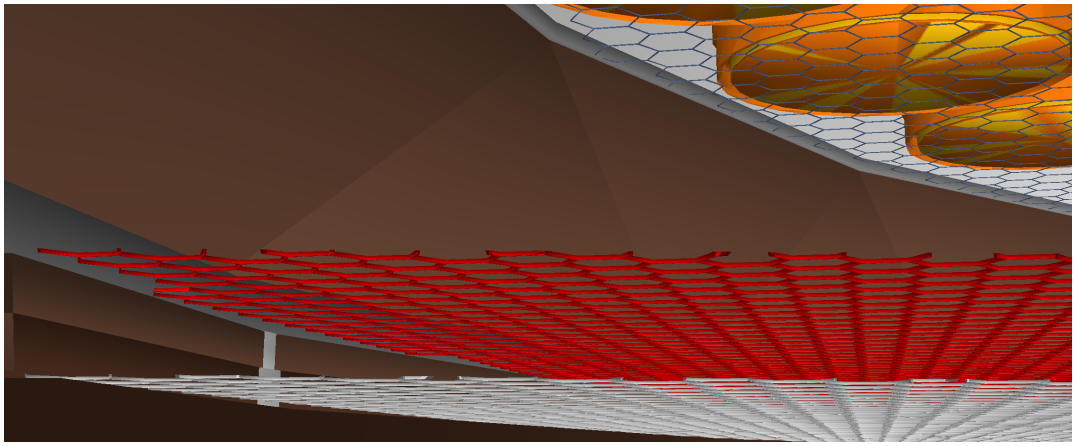

Figure 4.7: Implementation of the detailed meshes in GEANT4 for the upper part of the TPC. The anode (red) and gate mesh (gray) are shifted in the x-y plane as in the real detector with a z-distance of 5 mm.

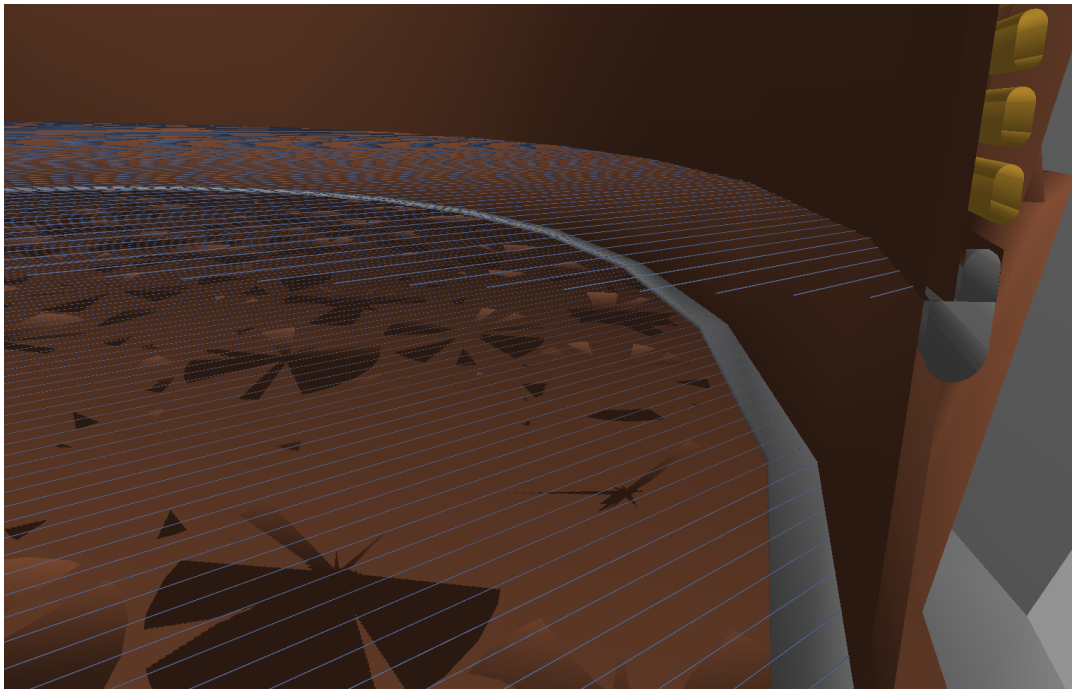

Figure 4.8: Implementation of the detailed meshes in GEANT4 for the bottom part of the TPC. The cathode and bottom screening mesh is shown by blue wires.

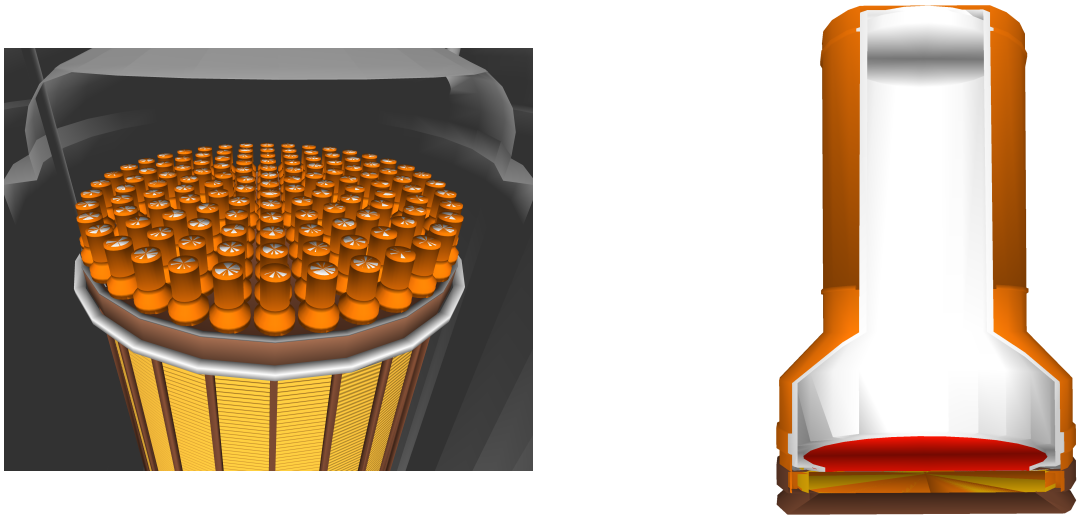

Figure 4.9: The top PMT array (left) and zoom on a single PMT as used in XENON1T (right). The simulation of a PMT includes a focusing PTFE structure (brown) right in front of the PMT quartz window (yellow), a photocathode (red) and a ceramic bottom (white) part. Each photon hitting the photocathode is registered and recorded for analysis.

4.2.3 Photomultiplier tubes

The XENON1T detector has two arrays of PMTs, one in the GXe region and one at the bottom in the LXe. A PMT type with a high quantum efficiency at UV light emitted by the xenon was chosen. The simplified structure of these 3-inch Hamamatsu R11410-21 is given in figure 4.9.

A single PMT consists of a quartz window, a photocathode and a bottom part made of ceramic and has a height of 114.1 mm. The interior of the PMT is under vacuum. Each PMT has a voltage divider circuit made of a simple 7 mm thick Cirlex® disk placed 14 mm apart. The PMT arrays are embedded in a PTFE and copper structure that reflect any photon not hitting directly a PMT window. The copper holder in between the PMTs will ensure that the PMTs are not moved while the PTFE structure is cooled down to −98 °C and shrinks. However, the PMTs are moved slightly inwards, which is neglected in the simulation. The top PMT array consists of 127 PMTs placed in a concentric ring pattern in a way that the outermost PMT ring exceeds the main chamber PTFE wall radius as described above. This will guarantee a better resolution of the x-y position for events close to the walls. The bottom PMT array has 121 PMTs in a hexagonal pattern, immersed in LXe. The PMT window is defined in the simulation as a sensitive volume that detects any particle hitting the volume and will register, absorb and record any photon. The values, which are then recorded and saved for analysis can be stored as simple number of total photon hits or in a detailed mode with additional PMT information such as the PMT ID that was hit.

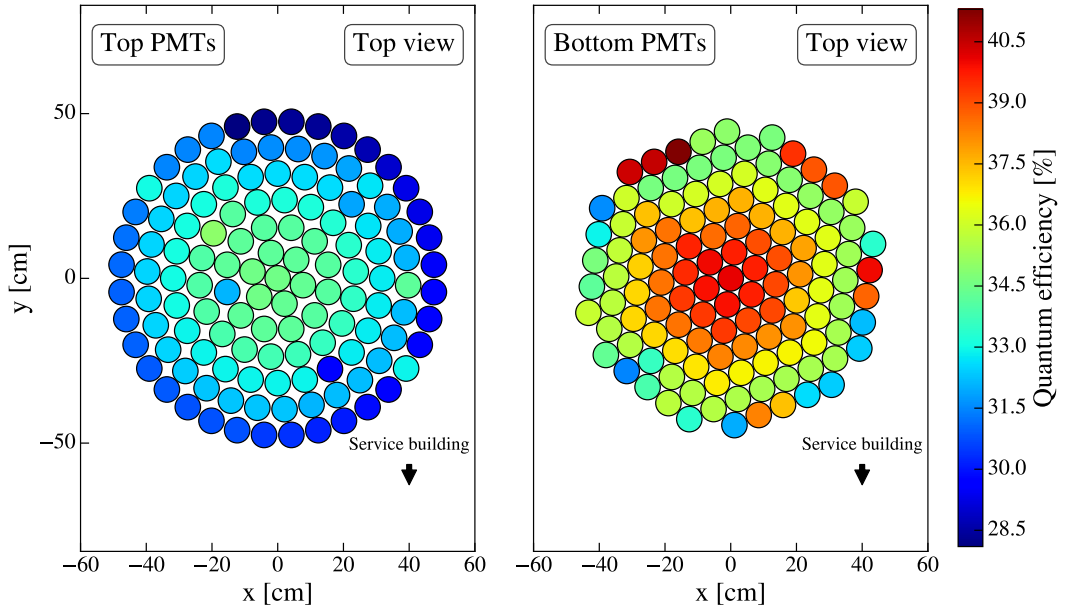

Figure 4.10: PMT QEs as given by Hamamatsu (see also [33, 16]) placed in a way that the best-performing PMTs are located at the center of the bottom array, where most of the scintillation light is collected.

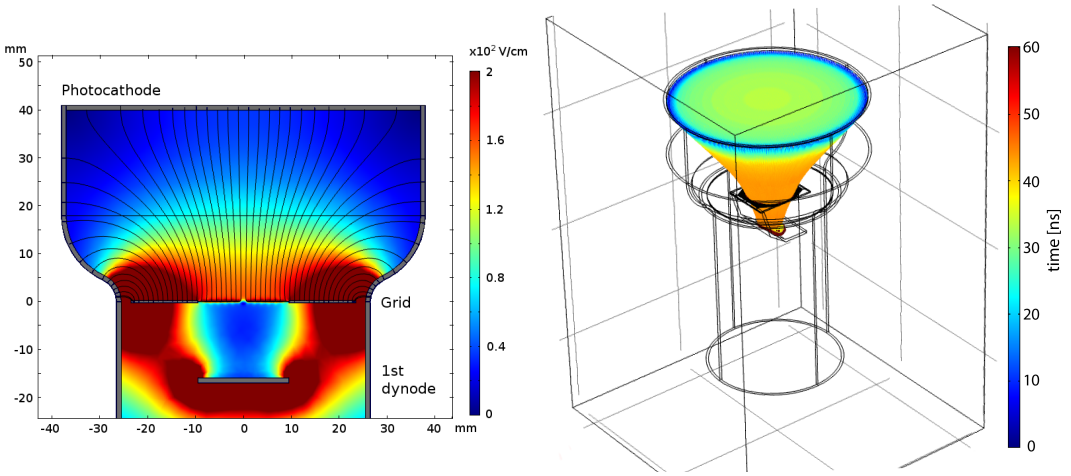

Figure 4.11: Simulation of the PMT electric field using COMSOL Multiphysics® (left), taken from [33]. The color scale indicates the field strength in V/cm. Electron transport has been simulated (right) in the generated field, allowing to estimate their transit times and the collection efficiency of the first dynode.

The quantum efficiency (QE) of a PMT is the ratio of electrons generated from incident photons hitting the photo cathode, also named as the photon detection efficiency. The XENON1T PMTs are chosen with the requirement of a QE around 30 % at a wavelength of 178 nm [33]. The selection of 248 out of 321 delivered PMTs is based on the rate of photons registered without incident light (dark count rate), the QE, the rate of counts following the main pulse mainly caused by ionization of residual gases (afterpulse rate), light emission by the PMT itself, long-term stability, peak-to-valley ratio and single photoelectron resolution [33]. The QE measurements are performed

at room temperature [34]. The selection of PMTs for XENON1T leads to an average QE of 34.5 %, as seen in figure 4.10. This QE value increases at LXe temperatures by a factor of 1.1 to 1.5 for 175 nm photons, within the FWHM of the xenon scintillation light [35].

Another crucial parameter of a PMT is the amount of electrons that is collected by the first dynode, the collection efficiency (CE). For a simulation of the CE, a model of the electric field and transport of electrons in the PMT was developed using COMSOL Multiphysics®. In the simulation, a homogeneous distribution of electrons is placed on the photocathode surface and drifted to the first dynode. These electrons are focused by the grid and collected with an efficiency of 95 % [33]. Another measurement by Hamamatsu reports a collection efficiency of 90 % [34] for the same PMT type. This difference of the simulation and measurement could be caused by different grid wire diameters in the simulation and the real PMTs (see [33, 34]).

4.3 Optical photon simulations

Optical photon simulations are divided into two different approaches for S1 and S2 signals, which imitates the origin of the photon generation. As described in chapter 3, the generation of S1 photons takes place in the LXe volume, while the S2 signals are generated in the GXe right below the anode (figure 4.12).

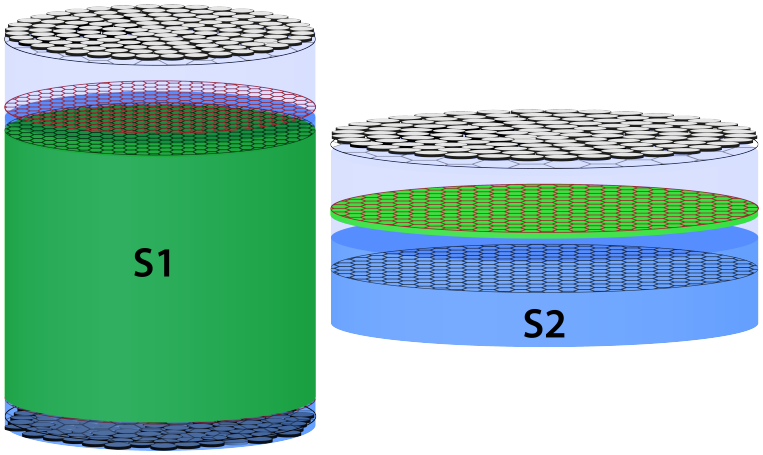

Figure 4.12: Visualization of the main S1 and S2 generation volume (green volume) as used in the MC simulations. The S1 volume is defined by the LXe between the gate mesh and cathode. The S2 volume is a 1 mm thin disk right below the anode.

Optical simulations are analyzed and quantified by using the Light Collection Efficiency (LCE), area fraction top (AFT) and light yield (ly). The number of detected photons strongly depend on several optical parameters like the attenuation length in liquid xenon and others as presented in section 4.4.
The LCE is defined as the percentage of photons that reaches a certain PMT out of a

given position in the simulated detector volume relative to the amount of generated photons. Therefore this value can only be calculated for optical photon simulations with:

$$\mathrm{LCE}(x,y,z) = \frac{N_{\mathrm{detected}}(x,y,z)}{N_{\mathrm{generated}}(x,y,z)}. \tag{4.2}$$

The *ly* can then be calculated assuming an average photon yield from NEST [36], where $\frac{1}{W}$ is the average energy that is required to produce one scintillation photon (e.g. W = 50 ph/keV, at 32 keV, at 150 V/cm):

$$ly(x,y,z) = \frac{1}{W} \cdot \mathrm{LCE}(x,y,z). \tag{4.3}$$

In addition to these values, which describe the total detection efficiency of all PMTs, the AFT is introduced in order to study the behavior of a single PMT array and is defined as the fraction of photons seen by the top PMTs to the total detected photons:

$$\mathrm{AFT}(x,y,z) = \frac{N_{\mathrm{detected\ by\ top\ PMTs}}(x,y,z)}{N_{\mathrm{detected}}(x,y,z)}. \tag{4.4}$$

Detailed information about each event in GEANT4 can be saved for analysis by setting the detailed PMT information parameter (*/analysis/settings/setPMTdetails*). With this, it is possible to determine which PMT was hit or where a photon is absorbed. This also allows the introduction of corrections to the perfect simulation data as described in chapter 5.

Optical photon simulations are performed by generating isotropic 7 eV photons (178 nm) uniformly throughout the active detection volume as seen in figure 4.12. The volume in which the photons are placed is generated by a slightly larger virtual cylinder that will be confined to the desired volume for the simulated signal type. Therefore, the generation of S1 photons is confined to the LXe volume between the gate mesh and cathode. Each GEANT4 event contains only one optical photon. These basic S1 simulations can directly show the fraction of light, which is seen by each PMT. The fraction depends on the amount of light or photons lost in various components of the TPC and is therefore mostly a geometrical effect but also includes the optical parameter settings as described in section 4.4. The PMTs are assumed to collect all light or photons hitting the PMT window, neglecting PMT effects like the QE and CE as described above.

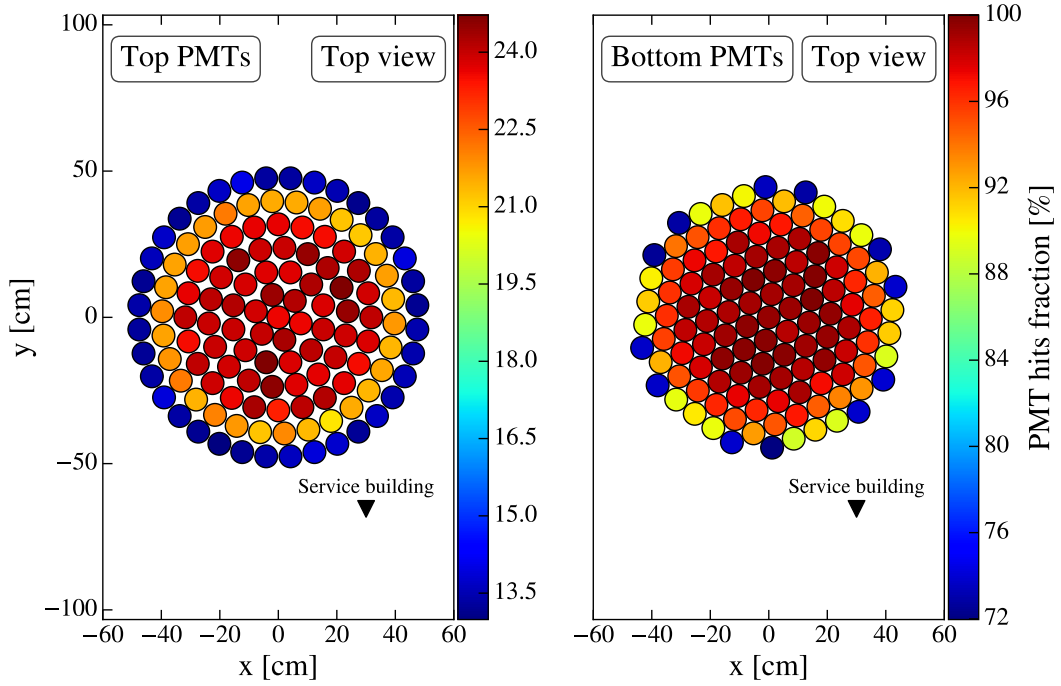

Figure 4.13: Fraction of S1 light or photons seen by each PMT for the top and bottom PMT array normalized to the PMT which sees the most photons, namely 25394 out of 10^7 for MC version 1.0.0.

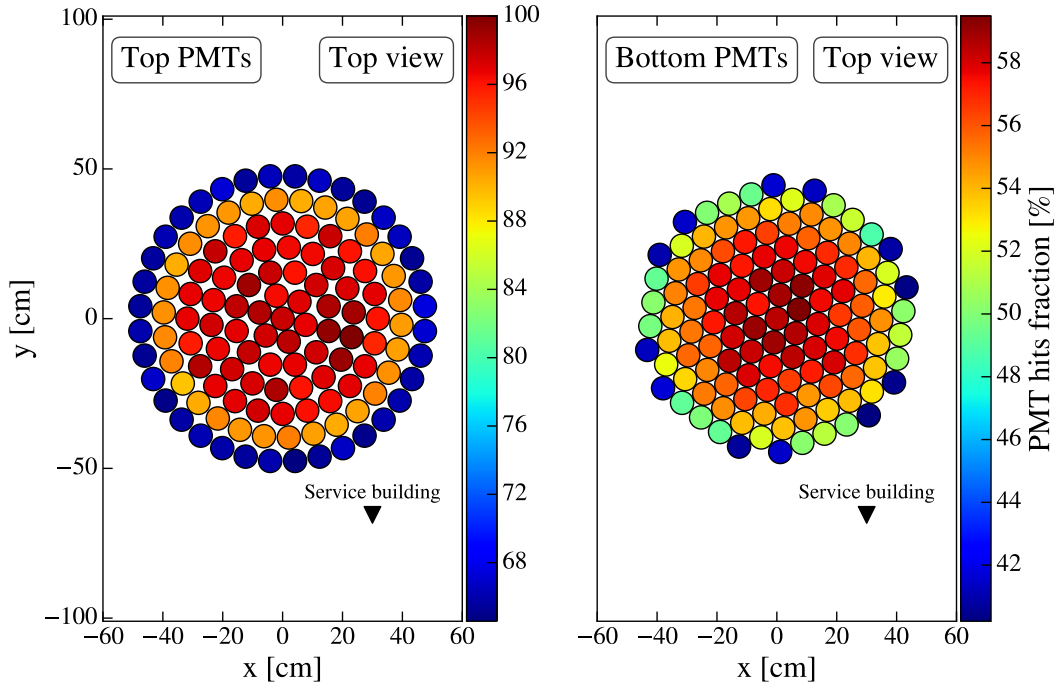

Figure 4.14: Fraction of S2 light or photons seen by each PMT for the top and bottom PMT array normalized to the PMT which sees the most photons, namely 12041 out of 10^7 for MC version 1.0.0.

It is clearly visible in figure 4.13 that most of the light is seen in the center of the PMT arrays. The small deviation of a few percentage are due to the limited statistics. In both arrays, top and bottom, the PMTs, which are located in the outer rings, get a smaller fraction of the S1 light. A few outermost PMTs in the bottom array see 30 % less light than the center PMT, which sees the most S1 photons. The fraction of detected photons in the outer ring is 10.5 % less than the most PMTs in the top array see, which can be explained by the radius of this PMT ring that is greater than the PTFE radius. The geometrical probability for S1 photons to reach this position is much smaller. The amount of photons detected in the bottom PMT array is 80 % higher than in the top array, due to reflection of the photons at the GXe/LXe interface. Detailed LCE maps that show the area from which each PMT is collecting light can be seen in section 6.1.

The S2 signal is generated in the GXe gap between LXe/GXe interface and the anode, which is a much smaller region than for the S1 signal. A detailed description of this generation volume is given in chapter 7. The results for a basic S2 simulation with the same settings as the previous S1 simulation is shown in figure 4.14. This simulation obtains a fraction of S2 light pattern which is similar to the one for the S1 simulations. Most of the light is seen by the center top array PMT, while still 58 % of the light is detected in the center bottom PMTs.

The previous simulations reveal that photons are stopped in several MC material volumes before they reach a PMT window. A list of these volumes simulated with the same optical parameter settings as given in [37] is shown in table 4.3. This list only includes the top ten volumes in which photons are stopped, showing that about 30 % of the light is lost in the meshes. Only 31 % of the photons are detected by PMTs, while 13.57 % are absorbed in the PTFE PMT holders in top and bottom. The distribution of photons strongly depends on optical parameters, that are defining the amount of photons lost in a volume, as shown in the next section.

Table 4.3: List of the top ten volumes in which photons are lost during optical photon simulations with the optical settings as in [37].

GEANT4 process	volume	fraction
OpAbsorption	PMT (detected)	31 %
OpAbsorption	gate mesh	15.65 %
OpAbsorption	bottom screening mesh	6.17 %
OpAbsorption	cathode	5.93 %
OpAbsorption	LXe	5.24 %
OpAbsorption	anode	2.32 %
OpAbsorption	top screening mesh	1.45 %
Transportation	PTFE	15.6 %
Transportation	bottom PMT array	11 %
Transportation	top PMT array	2.57 %
...	...	...

4.4 Optical parameters

This section will introduce the optical properties of xenon and PTFE, which are important for detection of low intensity VUV light signals in the XENON1T TPC. Known measurements and early assumptions for XENON1T are given together with simulations showing the impact on the LCE and AFT.
All simulations presented in this section are made by generating 7 eV photons uniformly distributed in the S1 or S2 volume as described in figure 4.12. In each investigation only one optical parameter is changed, while all other parameters are set to default values as used in the studies given in table 4.4. These optical parameters were assumed before the XENON1T experiment was running in 2016. The reflectivity of PTFE in LXe and GXe is set to 99 %, the absorption length of LXe to 50 m and for GXe to 100 m, the Ray Scattering length to 30 cm and the refractive index to 1.63. In addition a validation of these optical parameters with real data from the XENON1T detector, taken during the first and second science run, is performed stating a new set of optical parameters for future MC simulations.

Table 4.4: Definition of the optical parameter values as used in [37], before construction of XENON1T. The given values for the mesh transparencies were early assumptions and thus different from the ones given in table 4.2.

parameter	name in GEANT4	assumption
LXe refraction index	*LXeRefractionIndex*	1.63
LXe Rayleigh scatter length	*LXeRayScatterLength*	30 cm
LXe absorption length	*LXeAbsorbtionLength*	5000 cm
GXe absorption length	*GXeAbsorbtionLength*	10 000 cm
LXe PTFE reflectivity	*TeflonReflectivity*	99 %
GXe PTFE reflectivity	*GXeTeflonReflectivity*	99 %
top screening mesh	*TopScreeningMesh*	94.5 %
anode	*AnodeMesh*	92.9 %
gate mesh	*GateMesh*	92.9 %
cathode	*CathodeMesh*	96 %
bottom screening mesh	*BottomScreeningMesh*	94.5 %

An important parameter, which was not further investigated, is the refraction index of the PMT window. As described before, the PMT window is made of quartz and thus defines the efficiency of the light collection. Measurements given in [38] and [39] suggest a refractive index of 1.59 for a wavelength of 178 nm. Photons entering the PMT window are absorbed by the photocathode modeled in the simulation as a fully-opaque thin layer on the inner side of the window. The amount of photons reflected on the PMT window depends on refraction index of GXe and LXe as described in the following. Other effects like the absorption of photons in the quartz window are already modeled by the QE.

4.4.1 Liquid xenon refraction index

The refractive index of LXe is important to model the reflection and refraction on the LXe/GXe interface in the upper part of the TPC. It is defined as

$$n = \frac{c}{v}, \tag{4.5}$$

where c is the speed of light and v is the phase velocity of light in a specific material. This relation also determines the refraction when a light ray reach a phase boundary, given by Snell's law of refraction as

$$n_1 \sin\theta_1 = n_2 \sin\theta_2, \tag{4.6}$$

where θ_1 and θ_2 are the incidence angles of a light ray to the interface of the two materials. It is also possible that the light is totally (internal) reflected if there is no angle θ_2 fulfilling Snell's law (equation (4.6)). The critical angle for total (internal) reflection is given as $\theta_c = \arcsin(\frac{n_2}{n_1})$. Therefore, a good description of the LXe refractive index is needed for modeling the interface of LXe/GXe correctly, matching the amount of light detected in the top PMT array of the experiment. A change of this value can lead to longer path of photons in GXe or to more reflected photons.

Measurements of the LXe refraction index are ranging between $1.565 \pm 0.002 \pm 0.008$ [40] and 1.69 ± 0.02 [41]. The GXe refraction index can be assumed as 1. As a default value for other optical simulations, the refractive index in the XENON1T simulation is set to 1.63, as also given in [37].

The evolution of the LCE in dependency of the refraction index for the XENON1T MC is shown in figure 4.15. A decrease of $\sim$4 % LCE is obtained for S1 photons detected by both PMT arrays while the LCE for S2 photons is not changed. This means that the amount of photons, that are total internal reflected and in LXe absorbed, is increasing with the refraction index. Photons generated in the GXe, as for S2 photons, are not total internal reflected and thus do not show this behavior. This can also be seen in figure 4.16, where the AFT dependence on the reflective index for S1 and S2 photons is shown. The AFT value for S1 photons decreases, while the AFT for S2 signals stays unchanged within a few percent. An evolution of the LCE and AFT versus z-position is given in figures A.1 and A.2, supporting this explanation. These figures also denote a strong evidence that reflections on the PMT quartz window (refraction index of 1.59) are affecting the LCE in a way, that less photons with small incident angels are detected for refraction indices greater than the one of the quartz window.

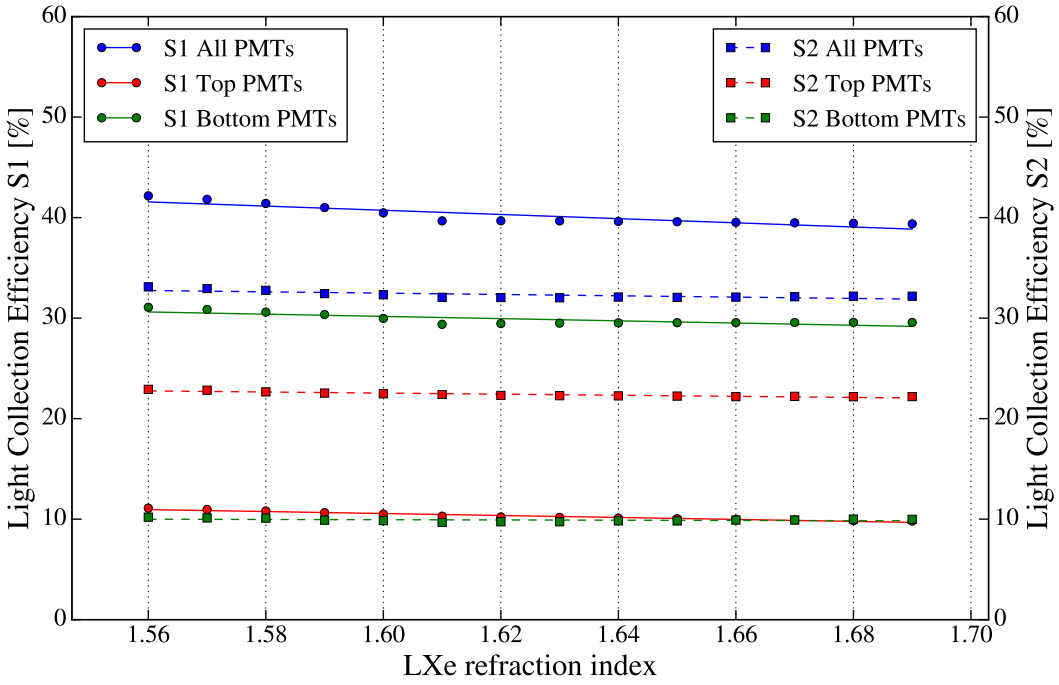

Figure 4.15: Evolution of the LCE with increasing LXe refractive index for S1 (left, dots) and S2 (right, squares) photons in optical simulations with 10^7 events for MC version 1.0.0. The signals are divided by the PMT array in which the photon is detected and are summed up in the blue data points. The data points are interpolated using a exponential function to guide the eye (dashed and solid lines).

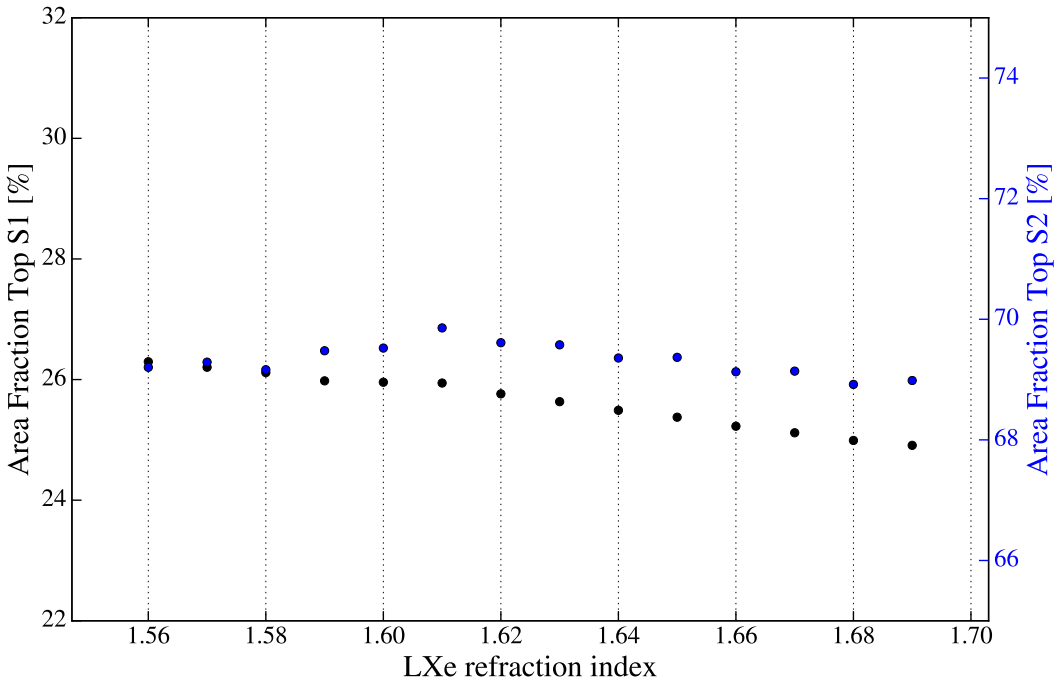

Figure 4.16: Evolution of the AFT with increasing LXe refractive index for S1 (black) and S2 (blue) photons in optical simulations with 10^7 events for MC version 1.0.0.

4.4.2 Liquid xenon Rayleigh scattering length

Another important optical parameter for experiments with novel detectors is the Rayleigh scattering length. Rayleigh scattering is an effect that takes place in transparent solids, liquids and gases, as in LXe and GXe. It can be described as an elastic scattering, where the state of the material with which the light is scattering is not changed. Photons are generated by particles of the material that act as small radiation dipoles induced by the electric field of the light wave traveling through the material. Due to this, the Rayleigh scattering is contributing to the attenuation of photons. A smaller scattering length corresponds to a higher fraction of attenuated photons. The value used in [37] is 30 cm based on theoretical assumptions [42], which defines the distance where the probability that a scattering takes place is $^1/_e$. Measurements report values ranging from 30 cm to 50 cm [41, 43, 44].

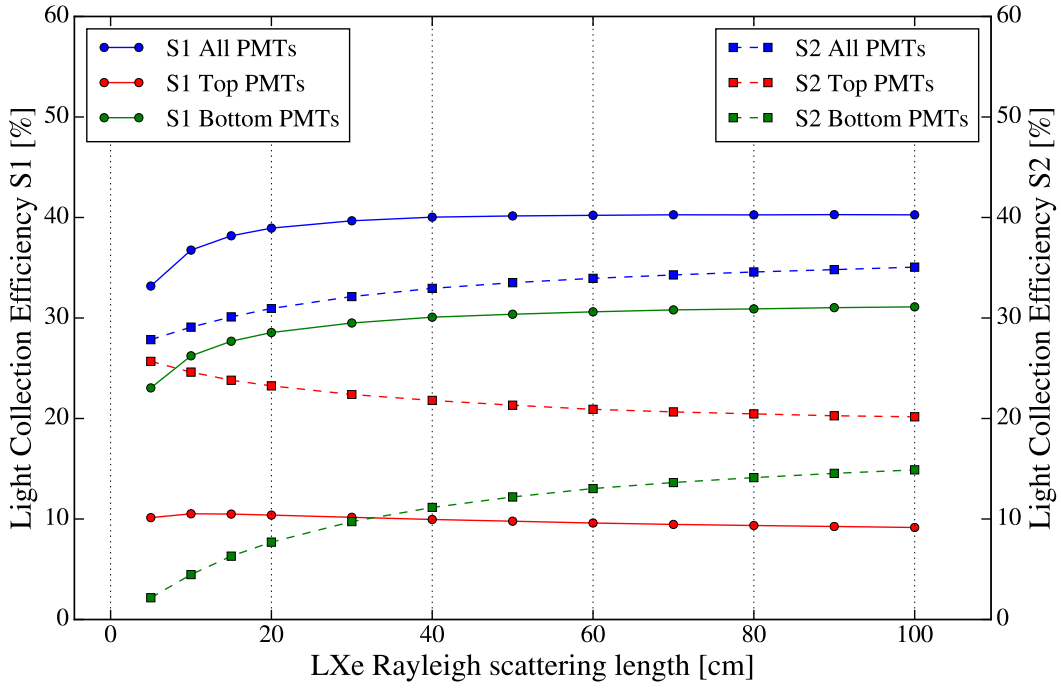

Figure 4.17: Evolution of the LCE with increasing LXe Rayleigh scattering length for S1 (left, dots) and S2 (right, squares) photons in optical simulations with 10^7 events for MC version 1.0.0. The signals are divided by the PMT array in which the photon is detected and are summed up in the blue data points. The data points are interpolated using a exponential function to guide the eye (dashed and solid lines).

As seen in figures 4.17 and 4.18, the LCE for S1 and S2 photons is decreasing for shorter Rayleigh scattering length, which corresponds to a higher probability of a photon being attenuated. Thus, this effect is proportional for photons, which have a longer path in LXe, such as in the middle of the TPC or on both ends pointing to the opposing end. While the amount of S1 and S2 photons detected in the bottom PMT array is decreasing with a shortened scattering length, the fraction of photons seen by

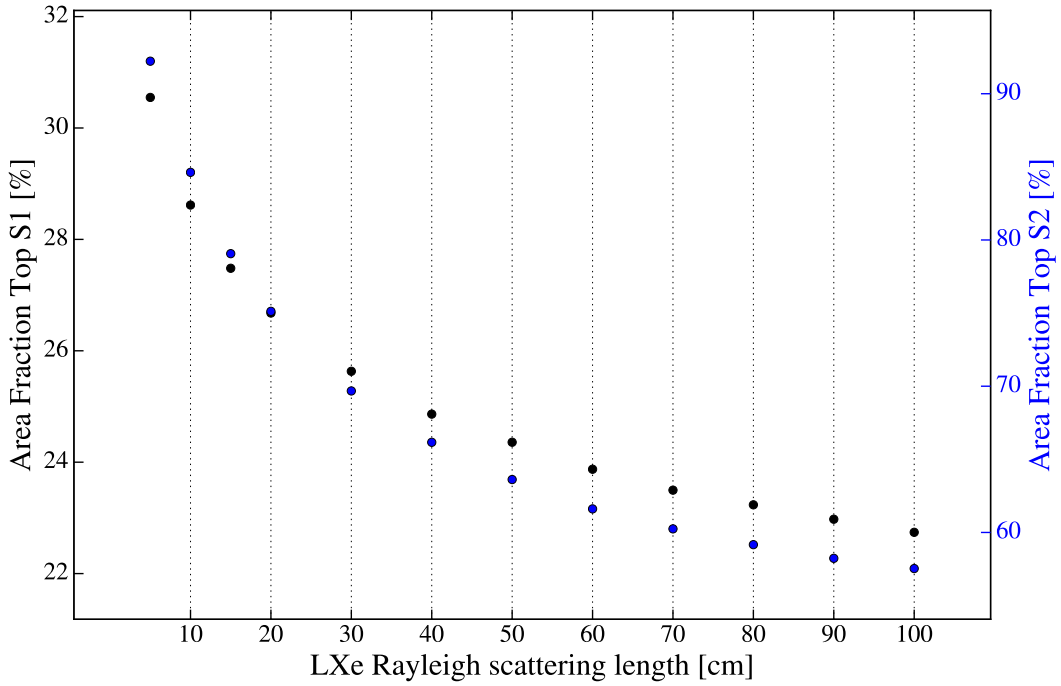

Figure 4.18: Evolution of the AFT with increasing LXe Rayleigh scattering length for S1 (black) and S2 (blue) photons in optical simulations with 10^7 events for MC version 1.0.0.

the top PMT array stays constant for S1 and increases for S2 photons. One hypothesis for this increase could be also directly related to Rayleigh scattering. Photons that undergo Rayleigh scattering in the LXe lead to an ionized and excited xenon atom which will result in an emission of an additional 7 eV photon. These additional photons are generated closer to the GXe/LXe interface with an uniform incident angle distribution and thus are more likely to be detected by the top PMT array. Therefore, the LCE is increased but also biased by photons with a position different from the initial generation. This kind of photons generated somewhere in the LXe will challenge the position reconstruction algorithms that rely on the amount of photons detected in each PMT. Accordingly, the fraction of the detected light seen by the top PMTs is increasing with decreasing Rayleigh scattering length for both, S1 and S2 photons. This can also be seen in the LCE against z-position trend for a selection of Rayleigh scattering length given in figures A.3 and A.4.

This effect of generating uncorrelated scintillation photons is discussed in [42] and is considered to be more important than impurities of the LXe, which is described in the next section.

4.4.3 Liquid xenon and gaseous xenon absorption length

The absorption length of LXe and GXe mostly depends on the amount of impurities and is therefore dependent on the purification of the detector material [37]. The absorption or attenuation length generally describes the distance λ in a given material, where the probability that a propagating particle has not been absorbed is $1/e$, or 36.8 %. This value is material and energy dependent. This parameter can also be seen as the combined effect of absorption, modeled by the absorption coefficient as given in figure 4.19. The absorption due to impurities is dominated by H_2O, O_2 and O. For example, liquid xenon containing 1 ppm of H_2O will absorb > 90 % of the scintillation photons within $\sim$10 cm (see figure 4.19).

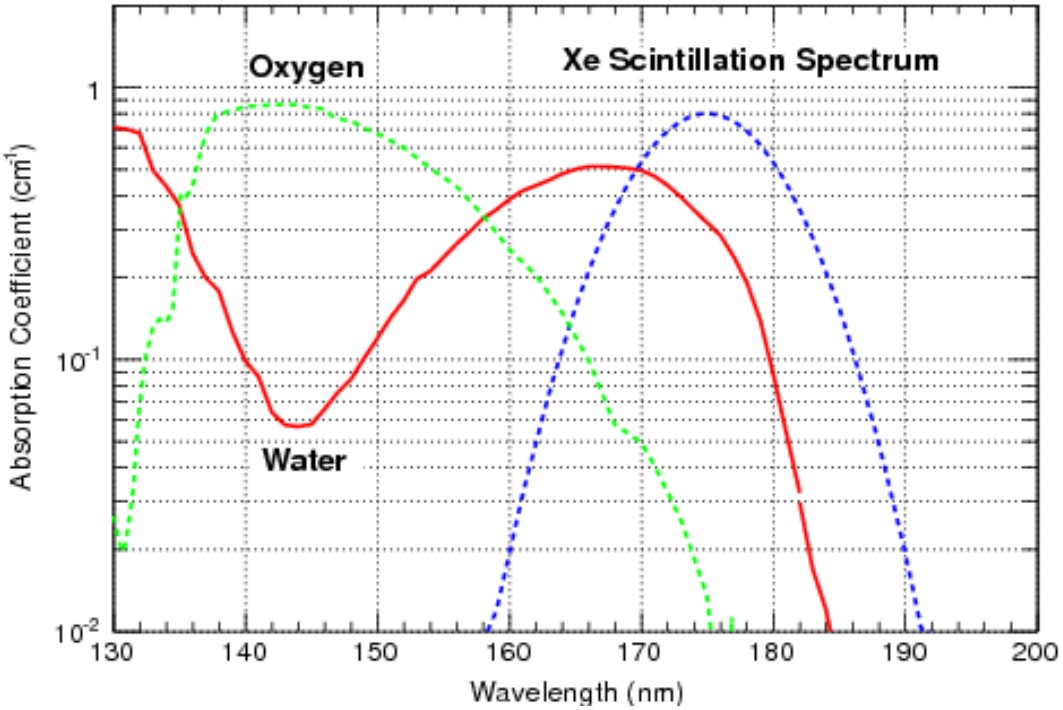

Figure 4.19: VUV absorption coefficients for 1 ppm water vapor and 1 ppm oxygen in liquid xenon. A typical spectrum of scintillation light in LXe is given for comparison [45].

The absorption length in XENON1T was conservative assumed to be 50 m, which was obtained by inversely proportional scaling from known values for 100 ppb level of H_2O to sub-ppb [37]. Therefore, a wide parameter space from $\sim$cm to 100 m is investigated by optical simulations. The simulations are performed independently for LXe and GXe assuming that a different level of impurities is possible in these material regions due to the xenon circulation in the detector, shown in figures 4.20 to 4.23. The total LCE for S1 and S2 photons increases with the absorption length of both, LXe and GXe, as expected above. However, the LCE for S2 photons detected by the top PMTs also increase with the LXe absorption length (figure 4.20) by a few percent. These S2 photons are reflected in the LXe region and propagate back through the

GXe to the top PMTs. This can also be noticed for photons detected by bottom PMTs while increasing of the GXe absorption length, shown in figure 4.22. The AFT for S2 photons in case of increasing LXe absorption length is decreasing (figure 4.21) as expected, while all other AFT values also increase. Additional information on the behavior of the LCE against Z-position is given in figures A.5 to A.8.

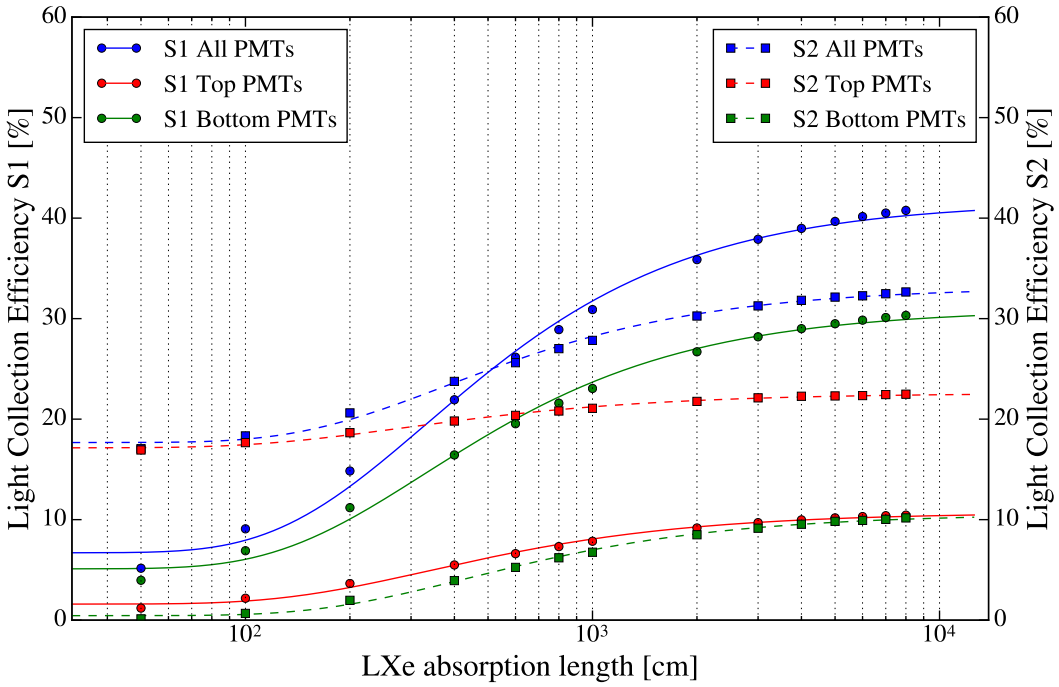

Figure 4.20: Evolution of the LCE with increasing LXe absorption length for S1 (left, dots) and S2 (right, squares) photons in optical simulations with 10^7 events for MC version 1.0.0. The signals are divided by the PMT array in which the photon is detected and are summed up in the blue data points. The data points are interpolated using a exponential function to guide the eye (dashed and solid lines).

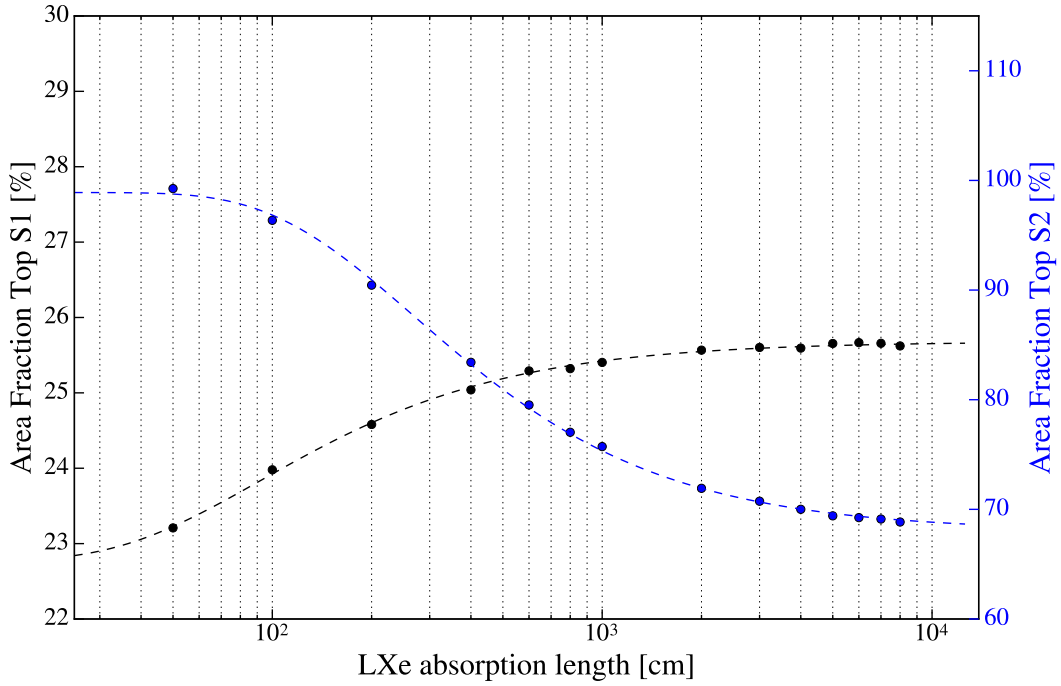

Figure 4.21: Evolution of the AFT with increasing LXe absorption length for S1 (black) and S2 (blue) photons in optical simulations with 10^7 events for MC version 1.0.0. The data points are interpolated using a exponential function to guide the eye (dashed and solid lines).

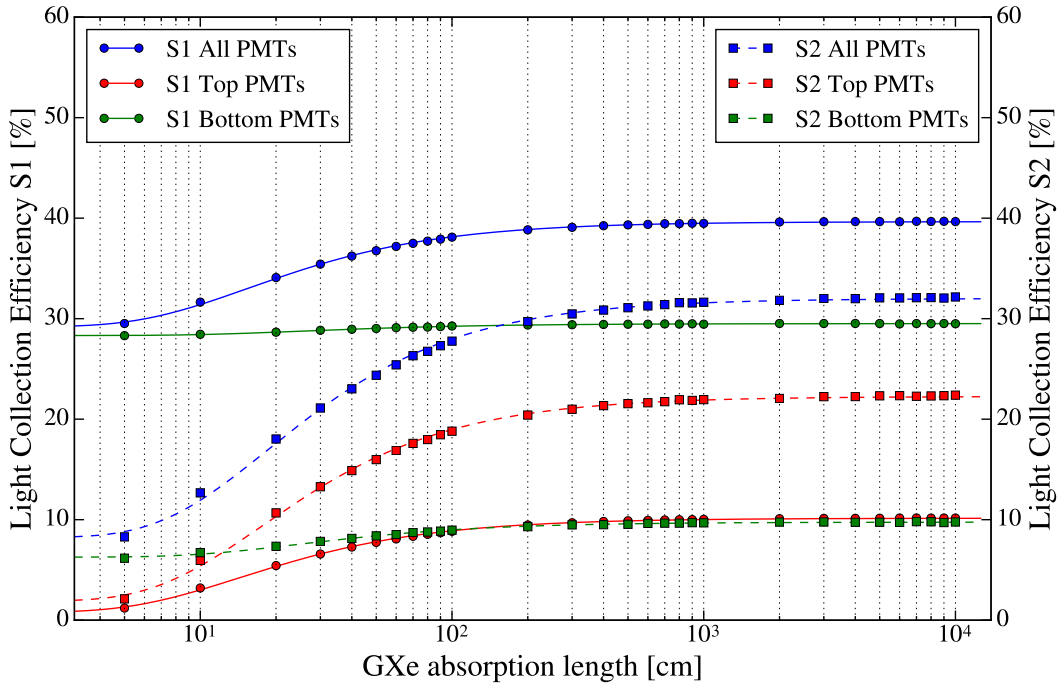

Figure 4.22: Evolution of the LCE with increasing GXe absorption length for S1 (left, dots) and S2 (right, squares) photons in optical simulations with 10^7 events for MC version 1.0.0. The signals are divided by the PMT array in which the photon is detected and are summed up in the blue data points. The data points are interpolated using a exponential function to guide the eye (dashed and solid lines).

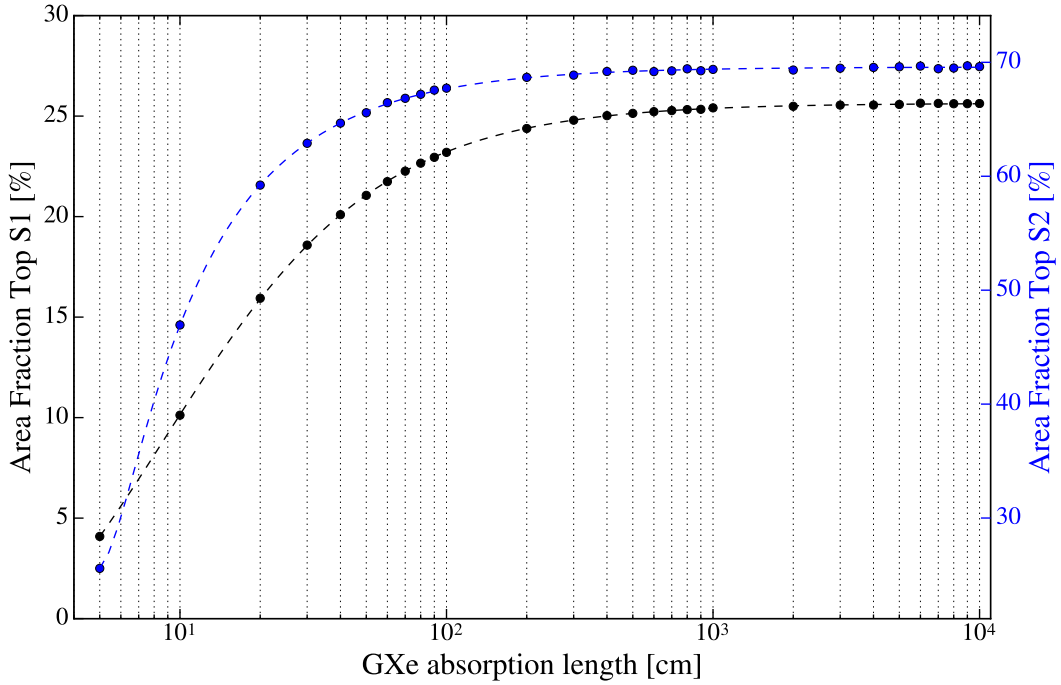

Figure 4.23: Evolution of the AFT with increasing GXe absorption length for S1 (black) and S2 (blue) photons in optical simulations with 10^7 events for MC version 1.0.0. The data points are interpolated using a exponential function to guide the eye (dashed and solid lines).

4.4.4 Polytetrafluoroethylene reflectivity

Another important part for the performance of the TPC is the inner PTFE surface, which is made to be highly reflective for VUV light. The real reflectivity strongly depends on the surface treatment, which allows to achieve reflectivity values above 99 % [37]. A detailed description of the PTFE reflectivity is already given in section 4.2.1. The XENON1T TPC has two main PTFE components, the main chamber, assembled by 47 PTFE parts, and the top part placed in the GXe. These two components could have a different reflectivity which leads to separate simulations for the GXe and LXe PTFE parts.

In case of the PTFE in LXe, the LCE for S1 and S2 photons is directly proportional to the reflectivity of the PTFE. The AFT value for S2 photons decreases by 25 %, while the S1 AFT value stays constant (figure 4.25). An increase of the GXe PTFE has only a small impact of a few percent on the amount of detected S1 photons (figure 4.26), while the increase of detected S2 photons cannot be neglected. Additional information on the behavior against z-position is shown in figures A.9 to A.12.

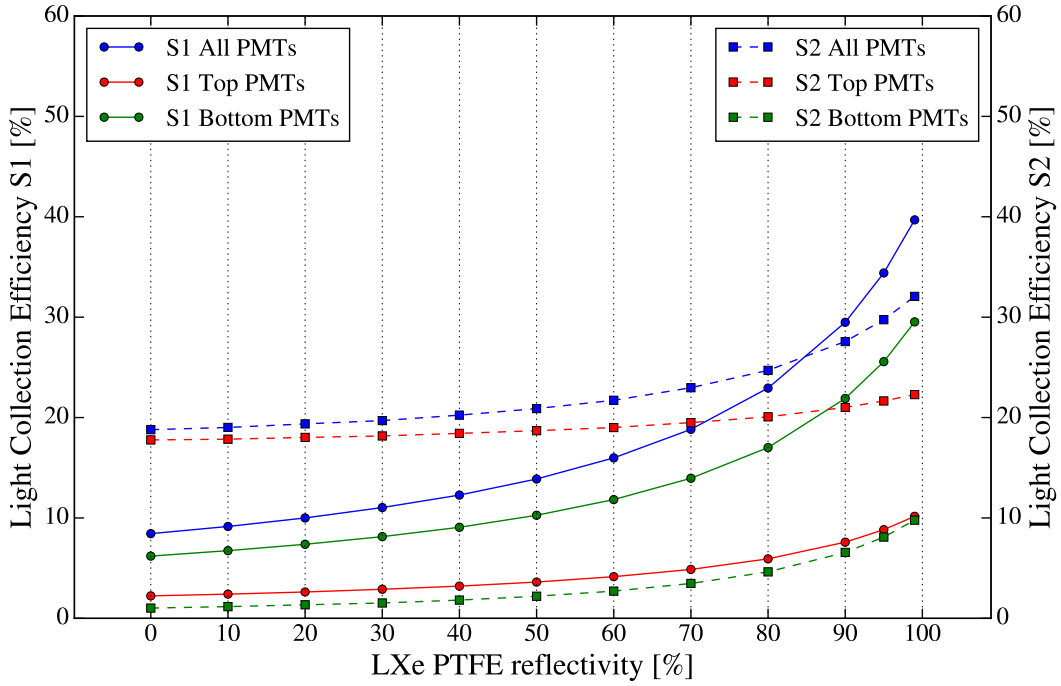

Figure 4.24: Evolution of the LCE with increasing LXe PTFE reflectivity for S1 (left, dots) and S2 (right, squares) photons in optical simulations with 10^7 events for MC version 1.0.0. The signals are divided by the PMT array in which the photon is detected and are summed up in the blue data points. The data points are interpolated using a exponential function to guide the eye (dashed and solid lines).

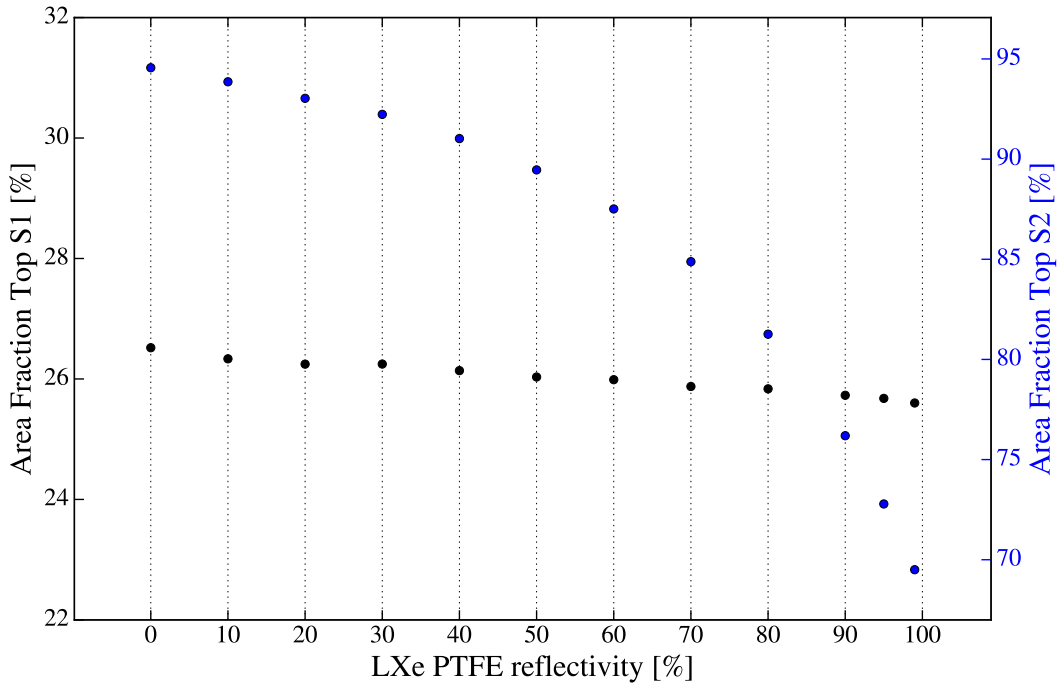

Figure 4.25: Evolution of the AFT with increasing LXe PTFE reflectivity for S1 (black) and S2 (blue) photons in optical simulations with 10^7 events for MC version 1.0.0.

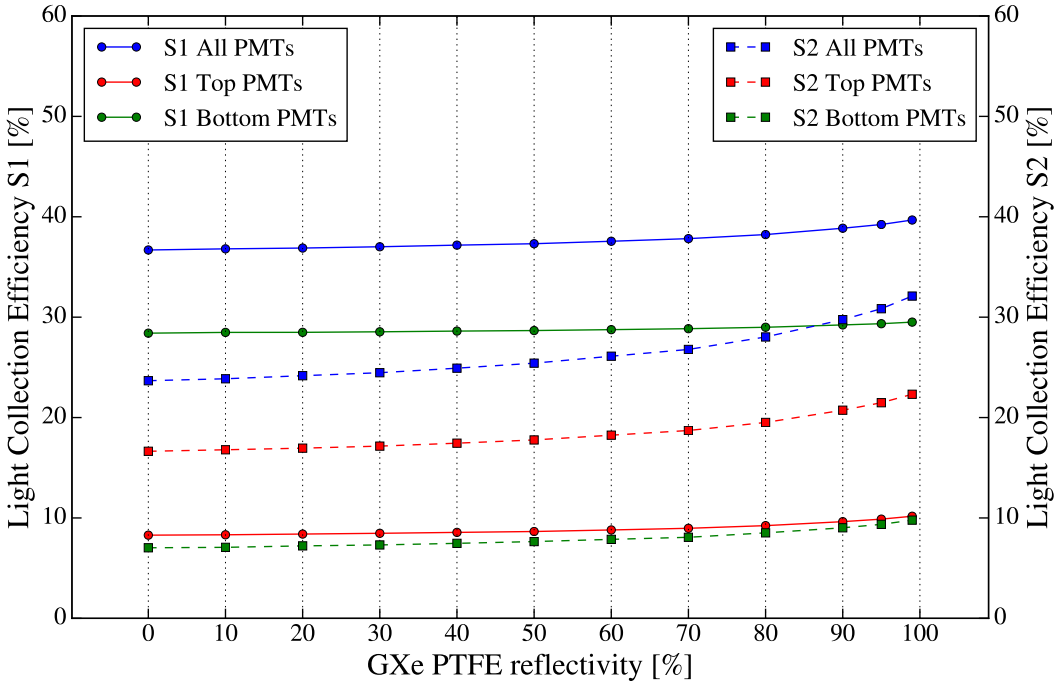

Figure 4.26: Evolution of the LCE with increasing GXe PTFE reflectivity for S1 (left, dots) and S2 (right, squares) photons in optical simulations with 10^7 events for MC version 1.0.0. The signals are divided by the PMT array in which the photon is detected and are summed up in the blue data points. The data points are interpolated using a exponential function to guide the eye (dashed and solid lines).

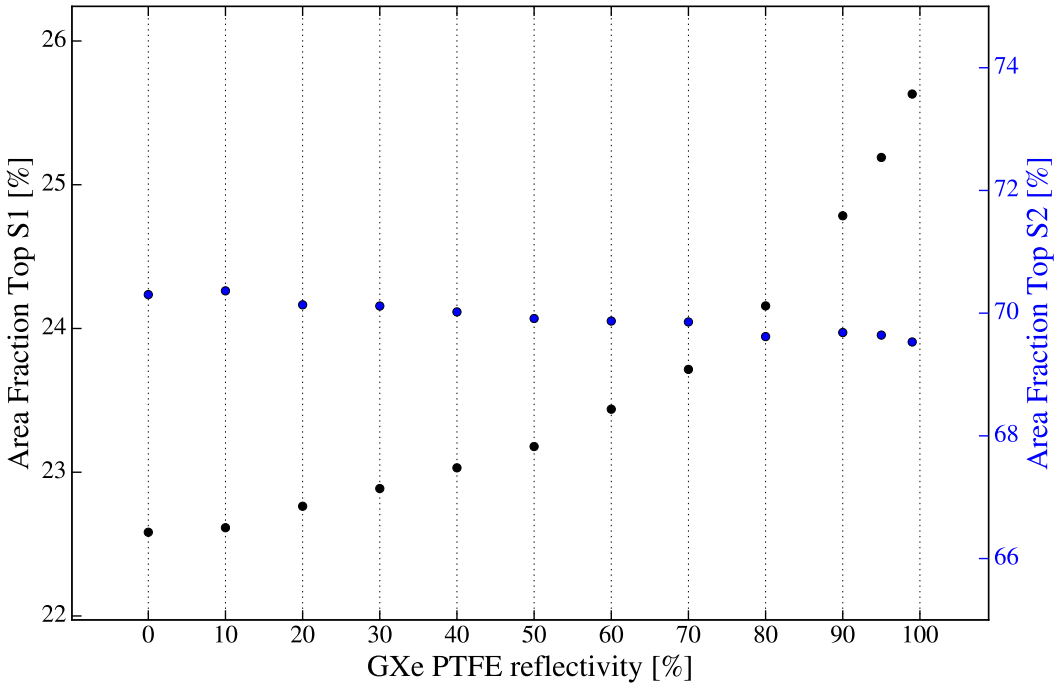

Figure 4.27: Evolution of the AFT with increasing GXe PTFE reflectivity for S1 (black) and S2 (blue) photons in optical simulations with 10^7 events for MC version 1.0.0.

5 Comparison of optical simulations to ^{83m}Kr measurements

This chapter will compare and adjust optical simulations with optical observables obtained from actual data of XENON1T. Therefore, the investigations of the optical parameter changes from the previous chapter are used to obtain a new set of optical parameters, after analyzing the performance of the current simulation configuration.

An initial simulated estimation of the LCE for the XENON1T detector is given in [37]. This simulation has been conducted before the detector assembly started, using 200 µm thick disks as meshes with absorption length calculated to match their respective transparency at normal angle [37] (see also section 4.2.2). In addition, the refractive index of each mesh is set to match the surrounding material, which makes reflectivity negligible. A LCE map, that gives the LCE as a function of the vertical

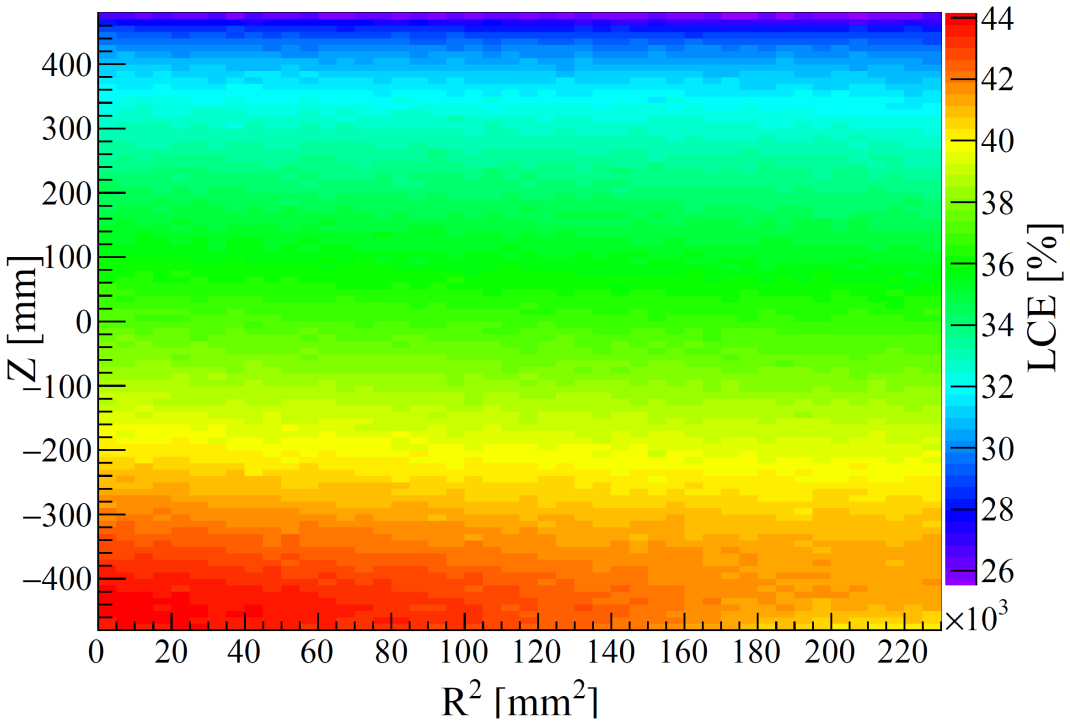

Figure 5.1: LCE map of XENON1T as a function of the position in the TPC, taken from [37]. The LCE is simulated and calculated using the optical parameters in table 4.4 and thin disk meshes. The position Z = 0 corresponds to the middle of the TPC region.

position Z and the radius squared R^2, is extracted using the optical parameters given in table 4.4, shown in figure 5.1. This LCE map is created by generating 178 nm photons uniformly and isotropically in the full volume of the TPC and calculating the LCE individually for each bin in R^2- and Z-direction. Due to the internal reflection of photons at the LXe/GXe interface, the LCE is higher close to the bottom of the TPC. The highest value is reached at the center of the bottom TPC, decreasing towards the top TPC region due to the increase in path length which increases the probability for photons of being absorbed in the LXe. The LCE map can also be converted into a *ly* map using equation (4.3):

$$ly(x, y, z) = f_{\mathrm{PE}}(x, y, z) \cdot W = \mathrm{LCE}(x, y, z) \cdot \mathrm{QE} \cdot \mathrm{CE} \cdot W, \tag{5.1}$$

where $f_{\mathrm{PE}}(x, y, z)$ is the probability for an emitted photon to produce a photoelectron (and is thus detected by a PMT) and QE and CE is defined as in section 4.2.3. The average *ly* extracted in [37] using a QE of 35 %, a CE of 90 % and a W value of 63.4 ph/keV is 7.7 PE/keV at zero field. The QE value quoted is not including an increase at LXe temperatures of about 10 %.

The aim of this chapter is to compare the initial simulated estimation of the LCE to actual data measurements of the XENON1T detector. This requires to correct the simulation output priorly as described in the following.

5.1 Introduction of corrections to the MC simulation

Since the MC simulation is assuming the designed detector, several effects are considered in this section that will correct the simulation results and makes it possible to directly compare the LCE maps of MC simulation and measured data. Effects that are not changing over time, like the implementation of additional detector parts or shape of components, are directly included in the MC simulation geometry and can be accessed by different versions of the MC package. The efficiency of the PMTs is implemented as 100 % light collection which means that all photons reaching the photocathode are saved as *PMThit*. Therefore PMT effects, such as the QE or CE, as described in section 4.2.3 needs to be considered.

The total amount of detected photons per PMT is therefore corrected by a CE of 90 % and the QE of each PMT (as shown in figure 4.10), where the QE is increased for LXe temperatures by 10 % as measured in [35]. Following equation (4.2), the corrected LCE is calculated as:

$$\mathrm{LCE}_{\mathrm{corrected}}(x, y, z) = \frac{(\sum_{\mathrm{PMT\ ID}}^{i} N_{\mathrm{detected\ hits}}(x, y, z, i) \cdot \mathrm{QE}(i)) \cdot \mathrm{CE} \cdot \mathrm{QE}_{\mathrm{increase}}}{N_{\mathrm{generated\ photons}(x,y,z)}}. \tag{5.2}$$

The corrected AFT value is obtained with:

$$\mathrm{AFT}_{\mathrm{corrected}}(x,y,z) = \frac{\sum^{i}_{\text{Top PMT ID}} N_{\text{detected hits}}(x,y,z,i)\cdot \mathrm{QE}(i)}{\sum^{i}_{\text{All PMT ID}} N_{\text{detected hits}}(x,y,z,i)\cdot \mathrm{QE}(i)}. \tag{5.3}$$

The major correction that needs to be applied is the amount of excluded PMTs which has an influence on the shape of the LCE map and lowers the average LCE value. Some PMTs could be included again into the analysis but a total of 35 PMTs (14.11 %) were excluded during the ^{83m}Kr measurements used in this thesis, as seen in figure 5.2 and described in the next section. Most of these PMTs showed a short light emission induced by xenon leaked into the PMT tube during operation. This behavior is observed when high voltage is applied to the PMT, which was the reason for turning off the PMTs during data taking. Several strategies to turn these PMTs on again without impact on measurements are currently under development. The fraction of S1 photons detected by each PMT (as seen in figure 4.13) including all mentioned effects and excluding 35 PMTs is given in figure A.14.

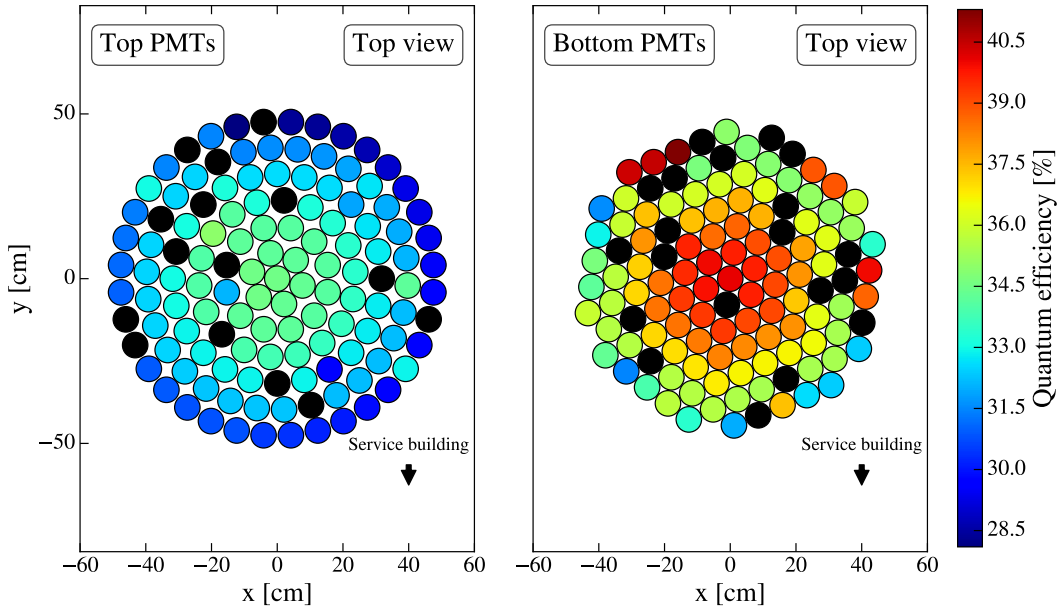

Figure 5.2: PMT QEs as given by Hamamatsu (see also figure 4.10) with 35 PMTs excluded from analysis in *ScienceRun_01* marked in black (see appendix A.3).

A comparison of the LCE as obtained in [37] and with the described correction is shown in figure 5.3. These simulations are performed using 10^7 photons. The dashed lines correspond to the case in which all photons reaching a PMT are detected without loss, while the solid lines represent the LCE with photon loss and 35 excluded PMTs. A reduction of 5.59 % total LCE (black lines) from 36.74 % to 31.15 % is visible. This reduction appears on the full S1 photon region with the most impact on the light collection of the bottom PMTs, where most of the PMTs are excluded (20 PMTs).

The exclusion of more bottom than top PMTs also impacts the AFT which is increased from 27.86 % to 29.06 %. A LCE map of the corrected simulation against R^2 is shown in figure A.15. The overall shape of the LCE map in figure 5.4 has not changed compared to figure 5.1.

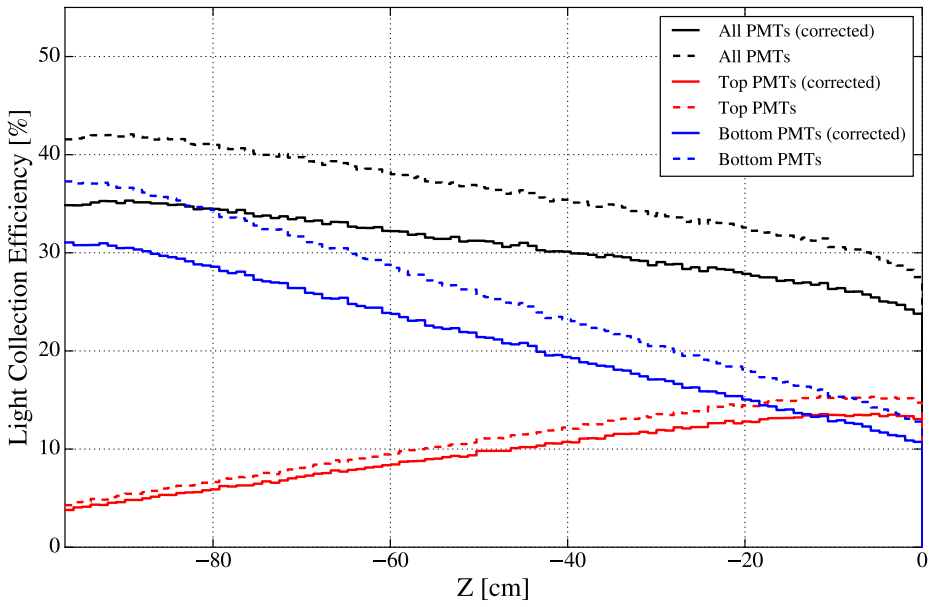

Figure 5.3: LCE obtained along Z-positions inside the TPC where $Z = 0$ corresponds to gate mesh position. Dashed lines indicates a LCE with *perfect* PMTs and solid lines for PMTs including the described correction (QE,CE and excluding 35 PMTs (figure 5.2)). The simulation is performed using MC version 1.0.0.

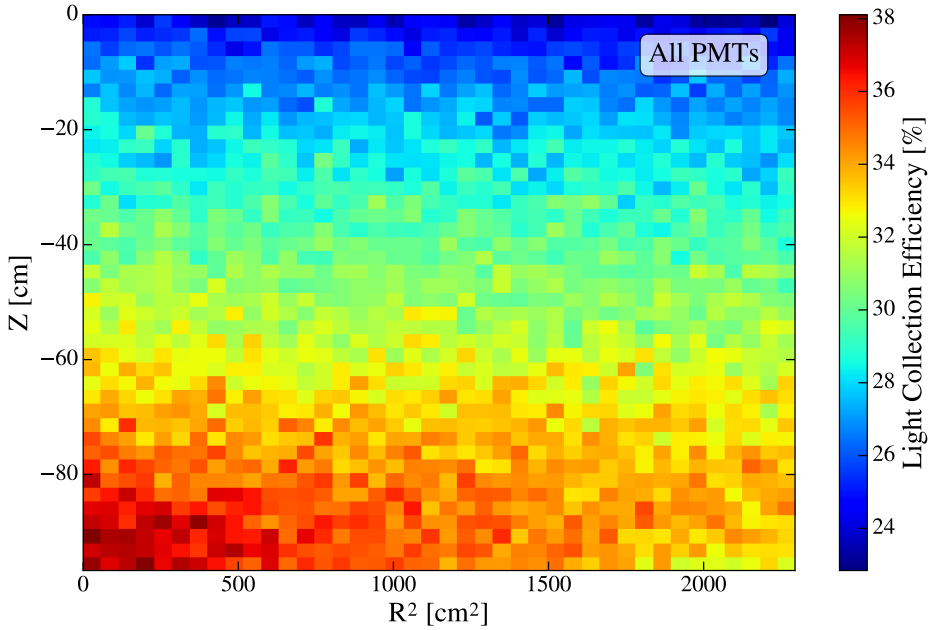

Figure 5.4: LCE map as a function of the position in the TPC calculated with respect to PMT effects and excluding 35 PMTs (figure 5.2). The label *All PMTs* denotes that both PMT arrays are included. The simulation is performed using MC version 1.0.0.

The corrected LCE map and other optical observables can now be directly compared to data measurements of XENON1T. A LCE map from actual data can be calculated using a ^{83m}Kr source, which is uniformly distributed in the TPC, such as the optical simulations.

5.2 ^{83m}Kr data analysis

The generation of a LCE map from measurements requires a light source which is uniformly distributed in the LXe as imitated in the previous simulations. This can only be achieved with an internal radioactive calibration source in XENON1T. Modern liquid noble detectors are therefore calibrated using the short-lived ^{83m}Kr without self shielding effects of xenon. This source disperses uniformly in the full detector volume and has suitable transitions at 9.4 keV and 32.1 keV as seen in figure 5.5, which makes it possible to search for irregularities in the detector response. The half-life of 1.83 h is short enough to not contaminate the xenon when inserted directly to the liquid xenon. XENON1T utilizes a method where ^{83}Rb is evaporated onto zeolite beads (2 mm), which is emitting ^{83m}Kr with a half-life of 86.2 days [46]. These beads can be inserted into the GXe that is circulating through the subsystems back to the TPC. The half-life between the 32.1 keV and 9.4 keV lines is 154 ns, which allows to extract the ^{83m}Kr signal background free as described in the following.

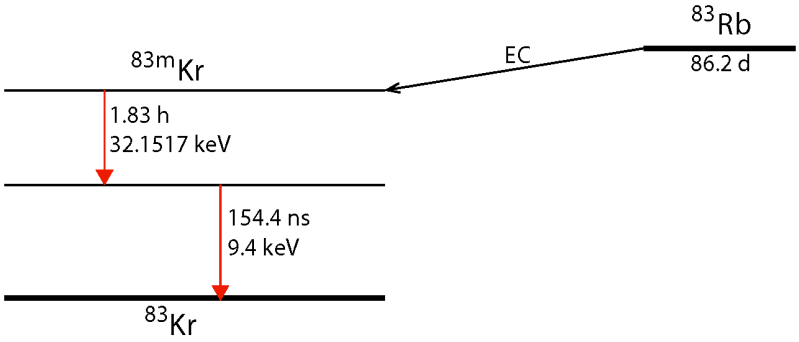

Figure 5.5: The decay scheme of ^{83}Rb and ^{83m}Kr (adapted from [47]).

The ^{83m}Kr calibration is not only used for LCE calculation, but also for position reconstruction algorithms, studies of non-uniformities in drift field, relative QEs of PMTs and absolute *ly* calculations.
Processing and analysis of data taken with XENON1T is performed by the PAX [48] and Handy Analysis for XENON (HAX). This open source software is designed to be highly customizable by implementing each step as a so called plugin. The following description of how the measured PMT signals are processed will only focus on main plugins, neglecting plugins like other position reconstruction algorithms, file format conversion or special signal corrections.

Interactions inside the TPC are recorded by the PMTs as *pulses*, which are defined as small regions of raw digitized data of each PMT *waveform*. Each *pulse* is treated as a PMT *hit* if a certain signal threshold in analog-to-digital converter (ADC) counts is exceeded.
This hit finding algorithm is calculating a *baseline* of the *waveform* from short *samples* at the beginning and end and setting two thresholds defined as 1σ and 5σ, using the standard deviation σ of the *baseline*. If a *pulse* is exceeding the lower threshold the algorithm starts to sum up the ADC counts until the threshold is undershot again. This summed signal is then stored as a *hit* if also the higher threshold was exceeded during the summation. The calculated ADC sum corresponds to the initial amount of photoelectrons detected by a PMT applying experimentally determined PMT gain values.
Hits appearing coincidental within a short time range are clustered as *peaks* using clustering algorithms, such as the *gap size*, which is based on the distance between *hits* [48]. These algorithms can identify PMTs that are detecting *hits* that are not coincident to other PMTs and exclude them from the clustering. The corresponding *peak* area calculated as the sum of all contributing PMT *hits* in photoelectrons is called *uncorrected* and needs to be classified and corrected depending on the initial interaction position.
Unclassified *peaks* can be observed in special cases during the classification and size-ordering of *peaks* in S1 and S2 signals, using the area and width. These signals are then paired to S1 and S2 *interaction* pairs reflecting the physical process of signal generation as discussed in chapter 3.
The initial position of an *interaction* can now be reconstructed using the S2 hit pattern and the time between the S1 and S2 signal. The obtained position allows to apply signal corrections such as the LCE or electric field dependence, which is indicated by the signal labels cS1 and cS2.

This data processing procedure is in case of ^{83m}Kr extended by an additional clustering and time-ordering step. The S1 signal of ^{83m}Kr reveals a special signature with a 32.1 keV and a 9.4 keV line, called $S1_a$ (first S1 signal) and $S1_b$ (second S1 signal), which appears due to the delayed coincidence with a half-life of 154 ns as shown in figure 5.5. This feature is used to extract only ^{83m}Kr events with a complete background suppression. The extraction of these events is performed by a *DoubleScatter* analysis toll, that discards all events with only one interaction in the target volume. The remaining events needs to be separated from background events, as discussed in appendix A.5.3. A full analysis of ^{83m}Kr in comparison to MC is given in section 6.2. The *ly* of these signals can then be extracted by dividing the observed peak area in photoelectrons with the corresponding energy of the ^{83m}Kr line in keV. For LCE studies typically the 32.1 keV line, the $S1_a$ signal, is chosen. The data used in this analysis was taken during *ScienceRun_1* of the XENON1T detector including 282

datasets from eleven ^{83m}Kr calibrations between February and July 2017. These are all datasets available for PAX version 6.6.5 leading to $1.51 \cdot 10^6$ events after cuts, which select events fulfilling certain signal conditions (see appendix A.5.3). The obtained LCE map using a position corrected $S1_a$ signal and excluding 35 PMTs (figure 5.2) is given in figure 5.6. A comparison of this map to the estimation calculated by MC simulations in shown in the next section.

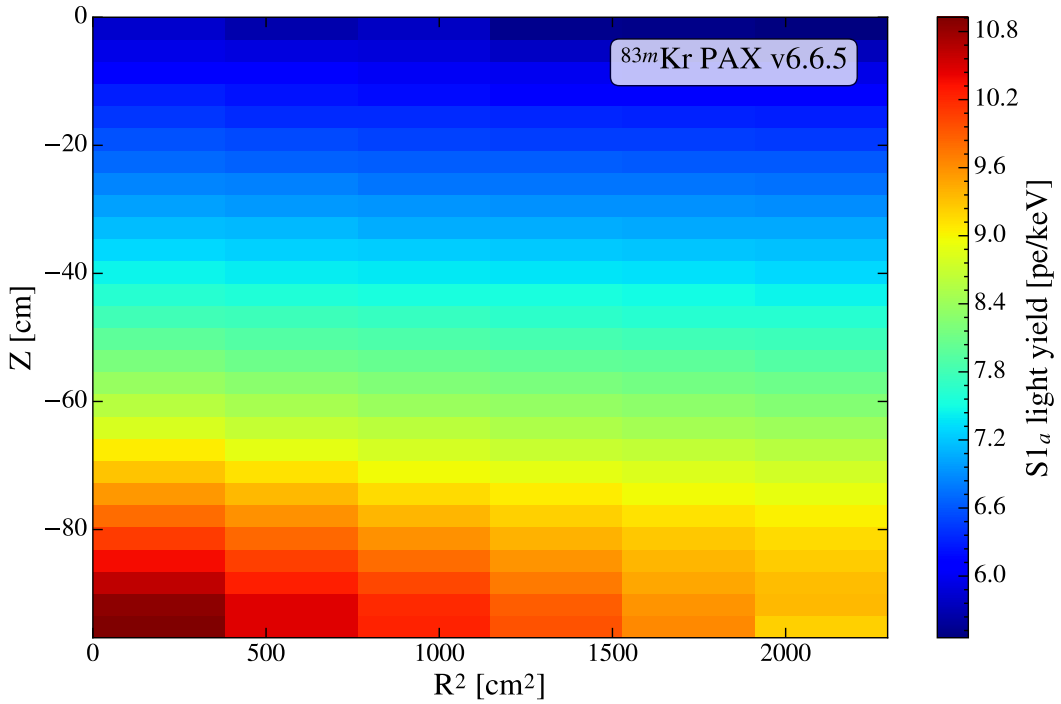

Figure 5.6: The *ly* map derived from the $S1_a$ signal of 282 datasets from eleven ^{83m}Kr calibrations during *ScienceRun_1* of XENON1T with an average *ly* of 8.07 pe/keV, excluding 35 PMTs (figure 5.2). The $S1_a$ signal was extracted using PAX 6.6.5 and the included *DoubleScatter* analysis tools. The corresponding relative Light Collection Efficiency (rLCE) map is given in figure 5.7.

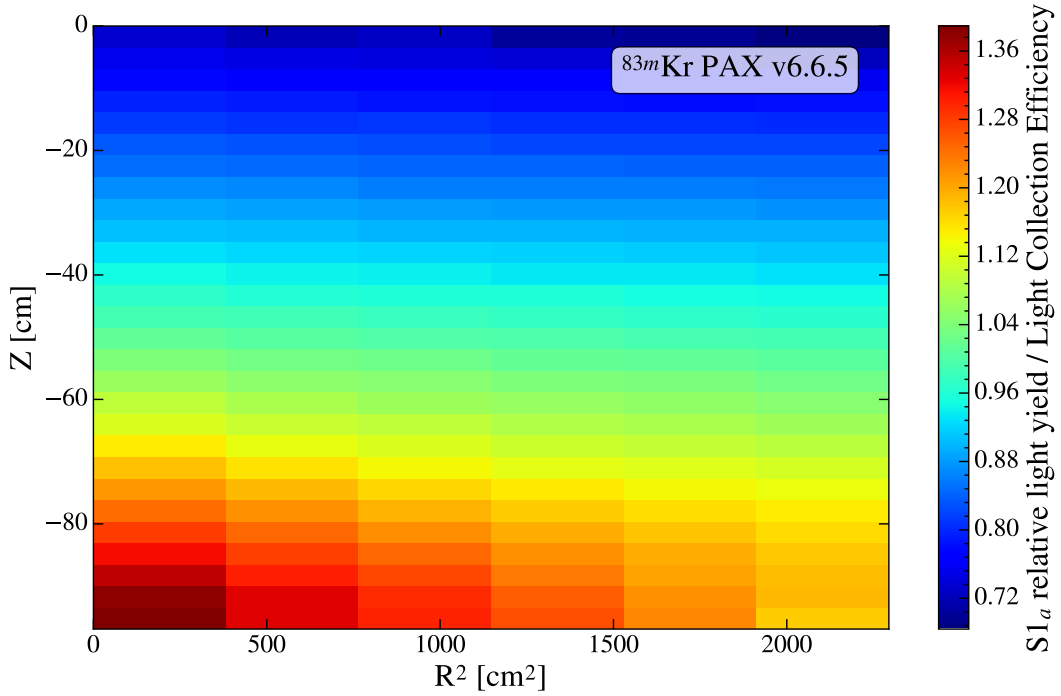

Figure 5.7: The relative Light Collection Efficiency (rLCE) map (see equation (5.4)) derived from the $S1_a$ signal, averaged to the mean of 8.07 pe/keV, as seen in figure 5.6.

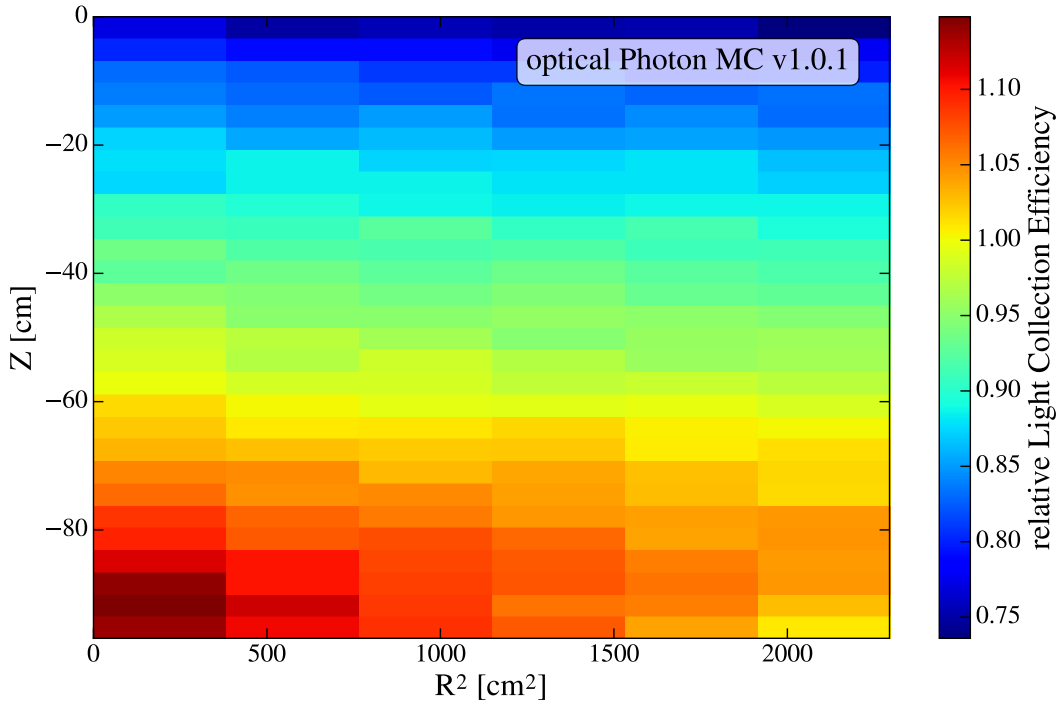

Figure 5.8: The relative Light Collection Efficiency (rLCE) map (see equation (5.4)) of MC simulations with initial optical parameter assumptions, excluding 35 PMTs and including PMT effects. The average LCE is obtained as 31.15 %.

5.3 Direct comparison of data measurements to MC simulations with initial optical parameter assumptions

A direct comparison of MC data to data taken during the *ScienceRun_1* of XENON1T can only be achieved by imitating the real detector conditions in the MC as seen in section 5.1. The LCE maps for MC and measured data in figures 5.4 and 5.6 can not be compared directly because the MC simulation is given in percentage of the initial generated photons and the map from measured data is calculated in pe/keV. A conversion of LCE to *ly* is in case of MC simulations possible but requires additional assumptions like the W-value, as seen in chapter 3. However, the calculation of a LCE value from a measured *ly* is not possible since the amount of initial photons is not known. Therefore both maps are converted to the rLCE by calculating the ratio of a local LCE or *ly* value in certain position to the average value of the full map:

$$\mathrm{rLCE}(x,y,z) = \frac{\mathrm{LCE}(x,y,z)}{\text{average LCE}} = \frac{ly(x,y,z)}{\text{average } ly}. \tag{5.4}$$

The maps generated by this method are directly comparable without additional assumptions.

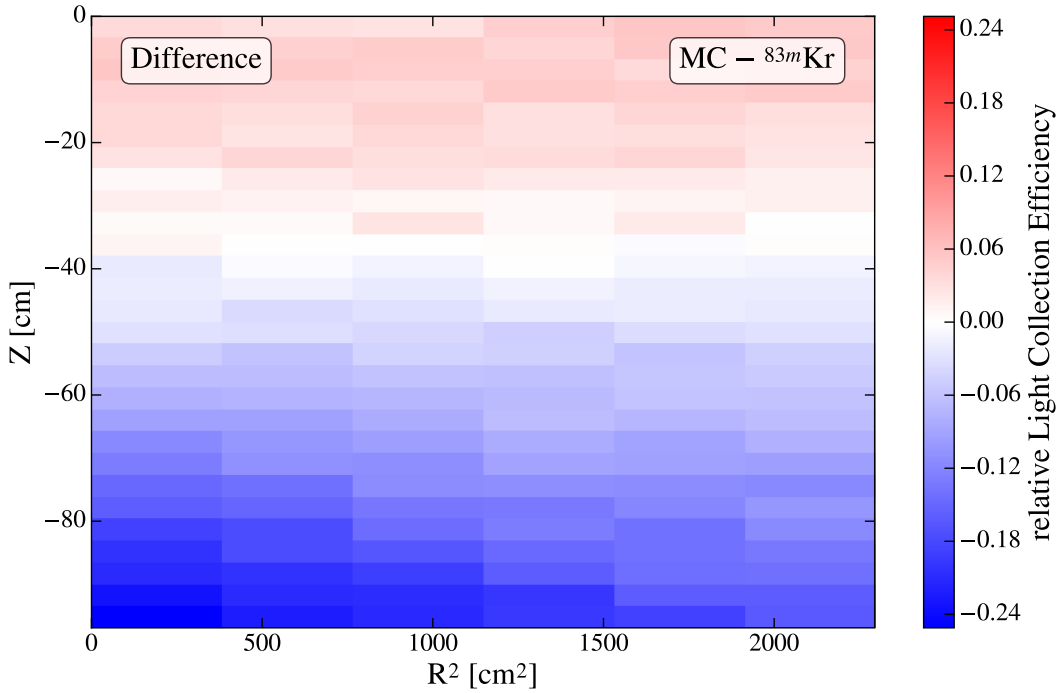

Figure 5.9: Difference of the rLCE maps for MC (figure 5.8) and measured data (figures 5.6 and 5.7).

As seen in figure 5.9, the rLCE in the bottom of the TPC is for measured data 0.24 higher than for MC while the values in the top part have only a difference of 0.03. A detailed comparison of both maps is achieved by comparing the rLCE and *ly* along the z-axis, because both values are not dependent on the radius (see figure A.15). These

observables can be obtained directly from the MC data and are fitted by Gaussian functions for measured data, as given in figures A.16, A.18 and A.19. The resulting values are compared in figures 5.10 and 5.11, showing that the MC simulation is not matching the behavior as observed for measured data. The total light collection in the upper part of the TPC has only a small difference of 0.05 rLCE but is divided different to both PMT arrays so that the rLCE is 0.14 higher for the MC simulation. This also causes the 16 % higher AFT value in figure 5.11. The increase of rLCE in the lower TPC is not connected to the total increase of the light collection. This leads to the conclusion that at least two optical parameters need to be adjusted, which will be presented in the following.

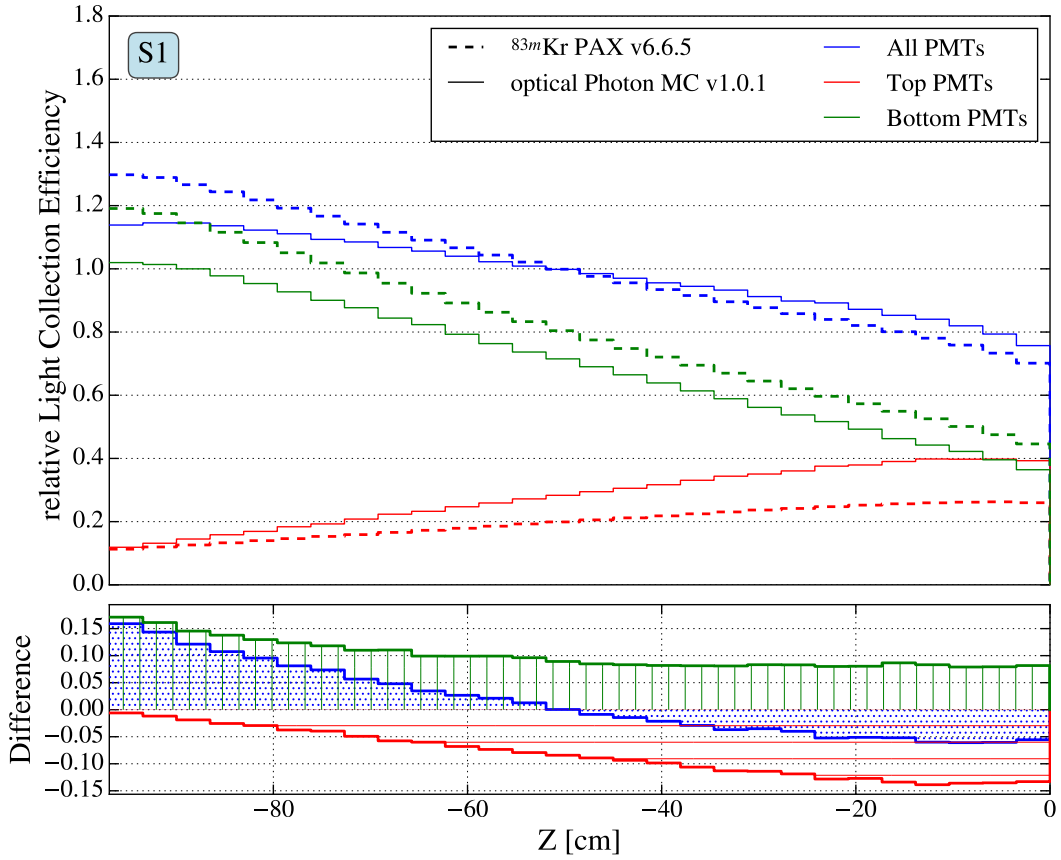

Figure 5.10: Comparison of the S1 rLCE for MC simulation with optical parameters as in table 4.4 (solid lines) and measured data from ^{83m}Kr calibrations (dashed lines).

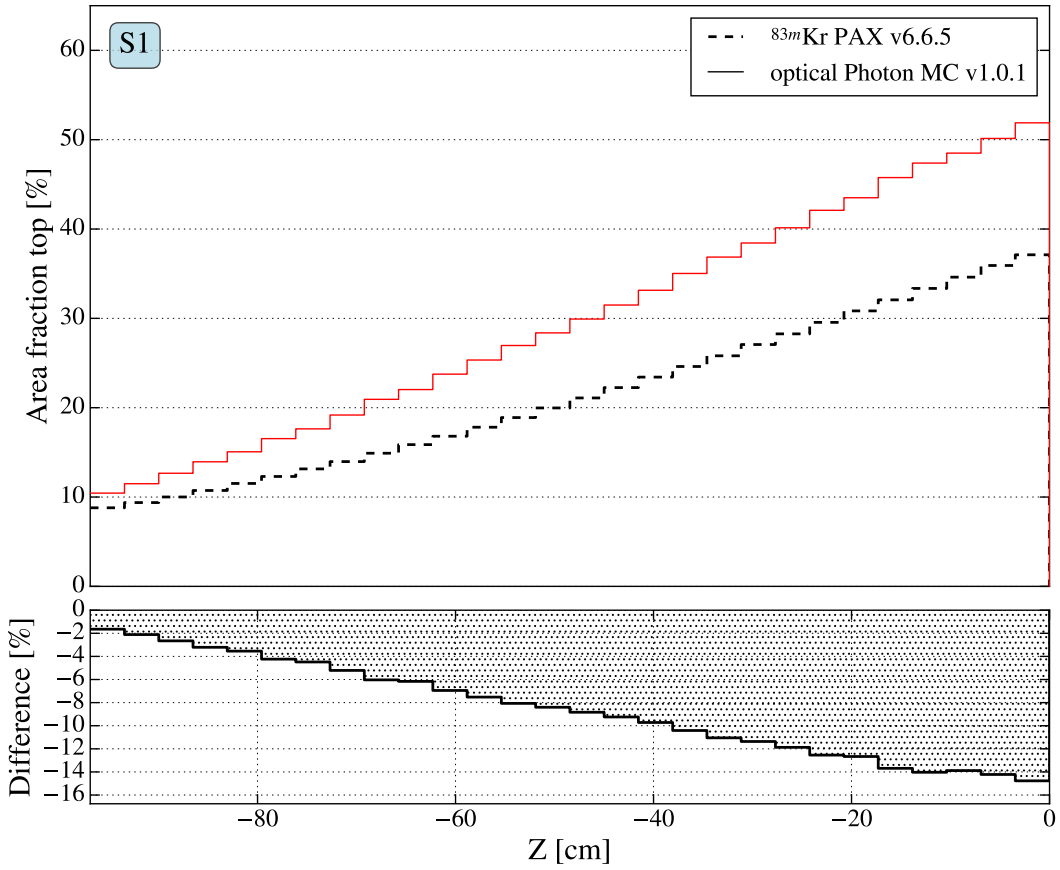

Figure 5.11: Comparison of the S1 AFT for MC simulation with optical parameters as in table 4.4 (solid lines) and measured data from ^{83m}Kr calibrations (dashed lines).

5.4 Fitting simulations to data measurements

MC simulations with the initial optical parameter assumptions (see table 4.4) are not matching the ^{83m}Kr measurements taken during *ScienceRun_1* of XENON1T in terms of rLCE and AFT, as described in the previous section. This leads to the need for an adjustment of the optical parameter settings and revisiting the geometry of the meshes in the MC simulation. Mesh transparency values used to imitate the mesh structure by thin disks were determined from technical drawings. Measurements of the actual wire diameter lead to more precise calculated transparencies given in tables 4.2 and 5.1.

The best matching MC simulation with a minimal difference to data measurements is obtained by scanning through thousands of possible optical parameter settings, which are chosen from the fitting range showed in table 5.1. Two simulations are performed for each parameter setting, one S1 simulation with $2{\cdot}10^7$ initial photons and a second S2 simulation with $2 \cdot 10^6$ events. These simulations and further calculations are performed on a cluster due to the runtime of around one hour per simulation depending on the actual optical parameter setting. These simulations have to be generated only once per MC version if the version is affecting the LCE or AFT. The S1 and S2 observables like the rLCE for top or bottom PMTs and AFT are then calculated for each simulation and saved in a data frame. The actual measurements from ^{83m}Kr calibrations are then compared to each set of observables by calculating the residual for 28 Z-slices and obtaining a root-mean-square deviation (RMSD) for each observable. The calculated RMSD values are then normalized and summed up in order to get the MC simulation with a minimized deviation from data.

Table 5.1: Optical parameter and mesh settings used in previous simulations in comparison to the result of the fitting data measurements to MC simulations. The range in which the parameters allowed to vary during the fitting is given in the last column. The values noted as *fitted values* are set as default optical parameters in the XENON1T MC version 1.0.1.

parameter	init. asm. [37]	fitted values	fitting range
LXe refraction index	1.63	1.69	1.56 to 1.69 [40, 41]
LXe Rayleigh scatter length	30 cm	30 cm	5 cm to 100 cm
LXe absorption length	5000 cm	5000 cm	10 cm to 80 000 cm
GXe absorption length	10 000 cm	50 cm	10 cm to 80 000 cm
LXe PTFE reflectivity	99 %	99 %	80 % to 99 %
GXe PTFE reflectivity	99 %	99 %	80 % to 99 %
top screening mesh	94.5 %	96.5 %	fixed (table 4.4)
anode	92.9 %	89.8 %	fixed (table 4.4)
gate mesh	92.9 %	92.7 %	fixed (table 4.4)
cathode	96 %	97.2 %	fixed (table 4.4)
bottom screening mesh	94.5 %	97.2 %	fixed (table 4.4)

The best matching simulation obtained by using the described fitting method is given in figures 5.12 and 5.13. Corresponding optical parameter settings are noted in table 5.1. These simulations revealed a higher LXe refraction index of 1.69 and a short GXe absorption length of 50 cm, which was expected to show the same behavior as the LXe absorption length. The rLCE is matching the data measurements for both PMT arrays along the Z-axis and exhibits a maximal difference of only 0.03 rLCE in the bottom of the TPC. A similar behavior is seen for the AFT of S1 and S2 photons, where the highest deviation is 2.5 % in the bottom of the TPC. Because of the small GXe absorption length, this approach is called *effective* matching, considering that this value has no physical meaning and was only introduced to match the data also in S2 AFT. It is possible to obtain a similar fitting result neglecting the S2 simulation observables, leading to a GXe absorption length of more than 1 m, where the impact of this optical parameter on the LCE begins to be neglectable (see figure 4.22). This result suggests that the S2 simulations are not performed correctly. A new approach of simulating S2 photons based on electric field simulations is presented in chapter 7. In addition, a hypothesis regarding the influence of the thin disk mesh implementation on the optical simulation was tested. Therefore, the matching was also performed

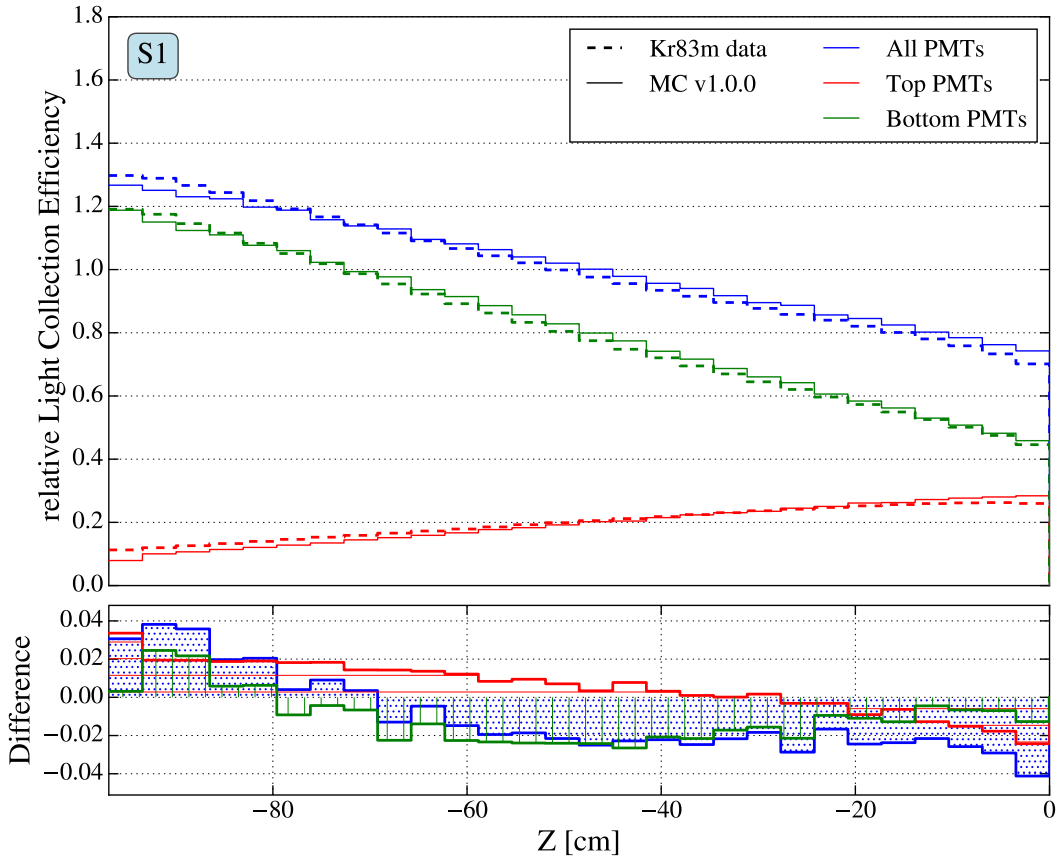

Figure 5.12: Comparison of ^{83m}Kr measurements (dashed lines) and MC simulation (solid lines) using fitted optical parameters and thin disk meshes with adjusted transparency values (see table 5.1).

with the detailed mesh implementation (described in section 4.2.2). Simulations with this detailed mesh implementation do not show differences in the results presented here. As a consequence of this, the thin disk approach is validated for the optical parameter matching.

The obtained optical parameter settings can now used as input for LCE maps and GEANT4 simulations as part of the full MC chain. The matching of optical observables in the full MC chain simulations, which depends on the parameter settings found in this chapter, is presented in the following.

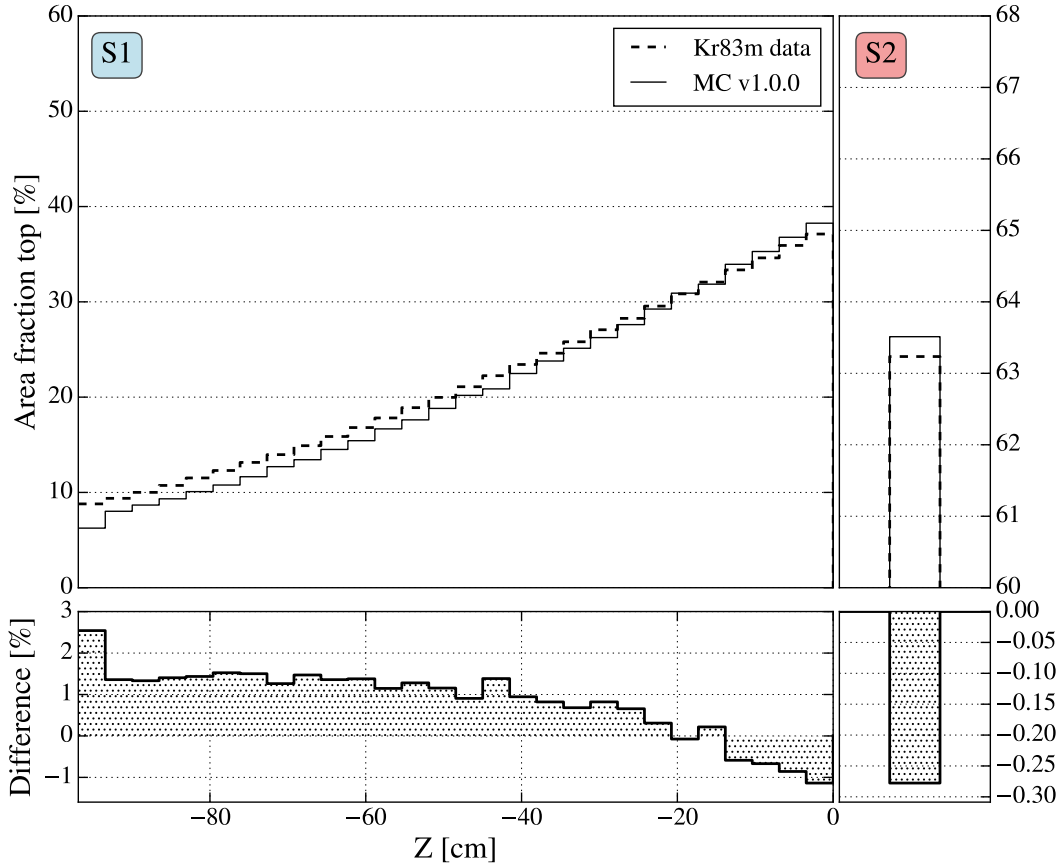

Figure 5.13: Comparison of ^{83m}Kr measurements (dashed lines) and MC simulation (solid lines) using fitted optical parameters and thin disk meshes with adjusted transparency values (see table 5.1). The left side shows the S1 AFT along the Z-axis, while the average AFT value for S2 photons is given on the right.

6 The XENON1T Monte Carlo chain

This chapter will introduce the full MC chain for XENON1T which allows to simulate any particle source through all different simulation stages. The GEANT4 simulations described previously present only the first stage of a fully developed model. The first section will focus on the generation of per-PMT LCE maps using optical photon simulations, which are used as an input to the full MC chain and in position reconstruction algorithms. The second section gives an introduction to the full MC chain and a comparison of ^{83m}Kr simulation to experimental data is performed.

6.1 Per-PMT Light Collection Efficiency maps for the FAke Xenon experiment

The FAke Xenon experiment (FAX) [49] is a waveform simulator for xenon TPCs like XENON1T and is included in PAX. This simulator makes it possible to predict how the actual detector including electronics responds to a release of photons or electrons in the detection region, by simulating PMT signals. FAX is operating as a converter of energy depositions to waveforms and still needs inputs from GEANT4, NEST and others, as illustrated in figure 6.1.

The first step for any FAX simulation is to obtain the number of photons and electrons generated by a particle in the TPC. These electron and photon yields are generated with GEANT4 and NEST [36] using a description of the particle source, like ^{83m}Kr distributed uniformly in the LXe, and the geometry of the detector. The energy depositions, obtained by GEANT4, are then converted by NEST into electrons and photons considering the electric field in the TPC. The XENON1T MC offers the possibility to apply the NEST calculations directly in GEANT4 or as a separated stage. These yields are used in FAX to generate waveforms in three conceptual stages:
In the first stage, the photon generation times of each event in the TPC are determined. These points correspond to the exact time stamp when photons are generated, in case of S1 photons by interactions and for S2 photons by electrons. The electrons generated together with the S1 light are drifted in the electric field, obtaining the time, position and amount of S2 photons. The drifting of electrons includes longitudinal diffusion in LXe and an increased drift velocity in the extraction field. A simplified S2 scintillation model is used, where the scintillation probability is uniform

up to a certain point close to the anode and continuing with $1/r$ up to the anode wire radius. This changing point is about 1 mm below the anode mesh. The scintillation is calculated considering singlet and triplet decays for excimers in GXe.
In the second stage, the PMT hit patterns are calculated, which describe the distribution of photons to the PMTs. The photons are distributed according to so called per-PMT LCE maps, as it will be described in this section.
In the last FAX stage, the information of the first two stages are combined and the actual response of the PMTs to the photons is simulated. This waveform generation includes PMT pulses with time spreads and gain variations from measurements, as

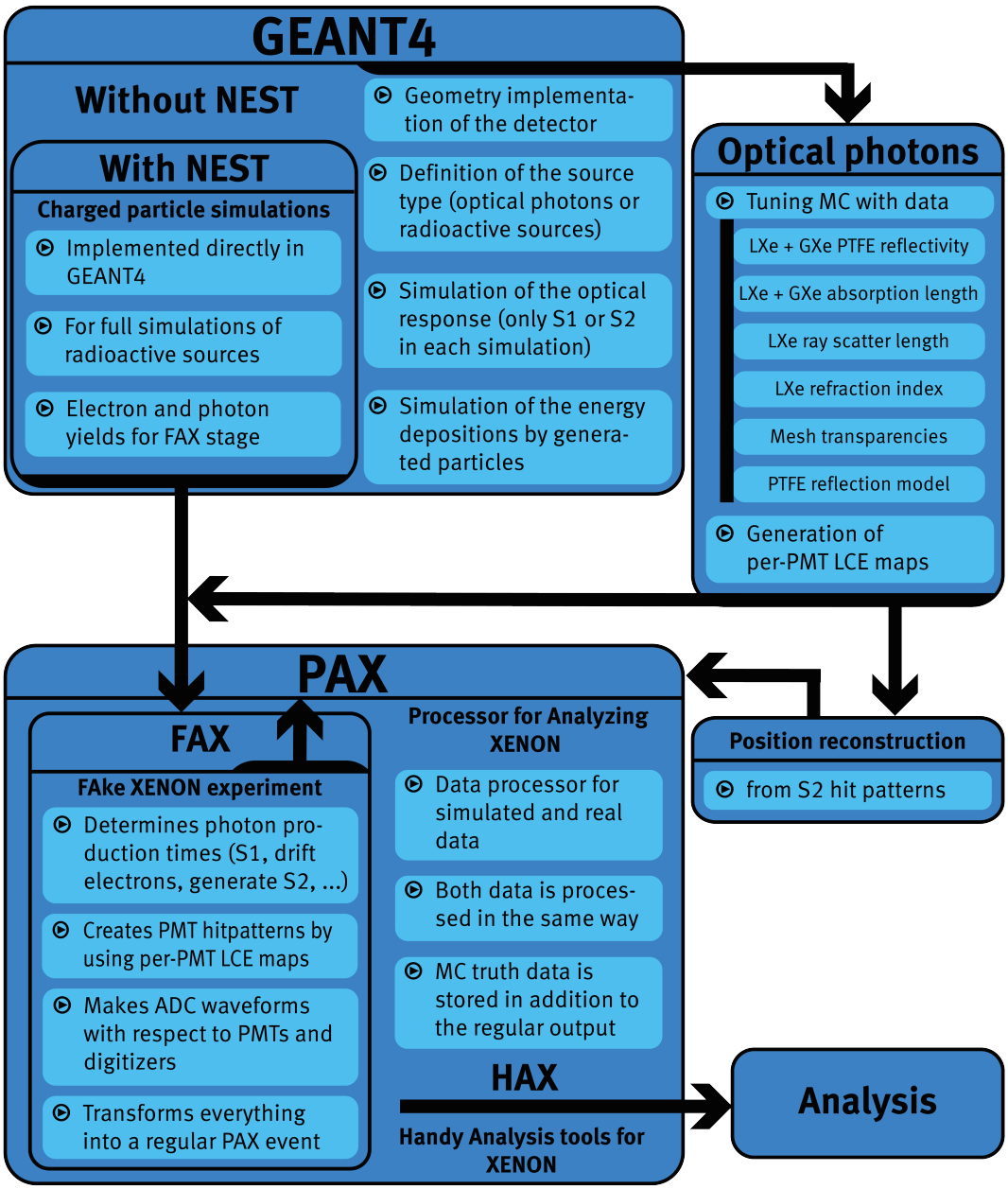

Figure 6.1: Relations between FAX and other XENON1T software tools.

well as real electrical noise from measurements without a light source. These waveforms are then directly processed with PAX and treated as normal measured data. The only difference in PAX is that some data corrections are not needed and that an additional file with MC truth information is generated, which contains information like the exact interaction positions to test the position reconstruction algorithms.

Per-PMT LCE maps are the main inputs of FAX to simulate the full detector response as close as possible. Other inputs are obtained with regard to the reconstructed position that is also obtained with per-PMT maps. The LCE maps need to be matched with data measurements and have to cover the full detection region, separated for S1 and S2 photons. But also most position reconstruction algorithms used in XENON1T rely on per-PMT maps for S2 photons to estimate the initial position by the generated PMT hit pattern. The performance of these algorithm is thus directly linked to the optical parameter matching and accuracy of the simulated detector geometry.

6.1.1 Per-PMT map for S1 photons

Per-PMT maps are generated by optical photon simulation like the previous LCE simulations. The S1 photons are generated between the PMT faces of both PMT arrays in the LXe and GXe. This extend of the S1 volume, defined in figure 4.12, is introduced to simulate S1 signals also for the GXe in FAX. A total amount of 10^9 photons are generated in order to achieve sufficient statistics for each single PMT.

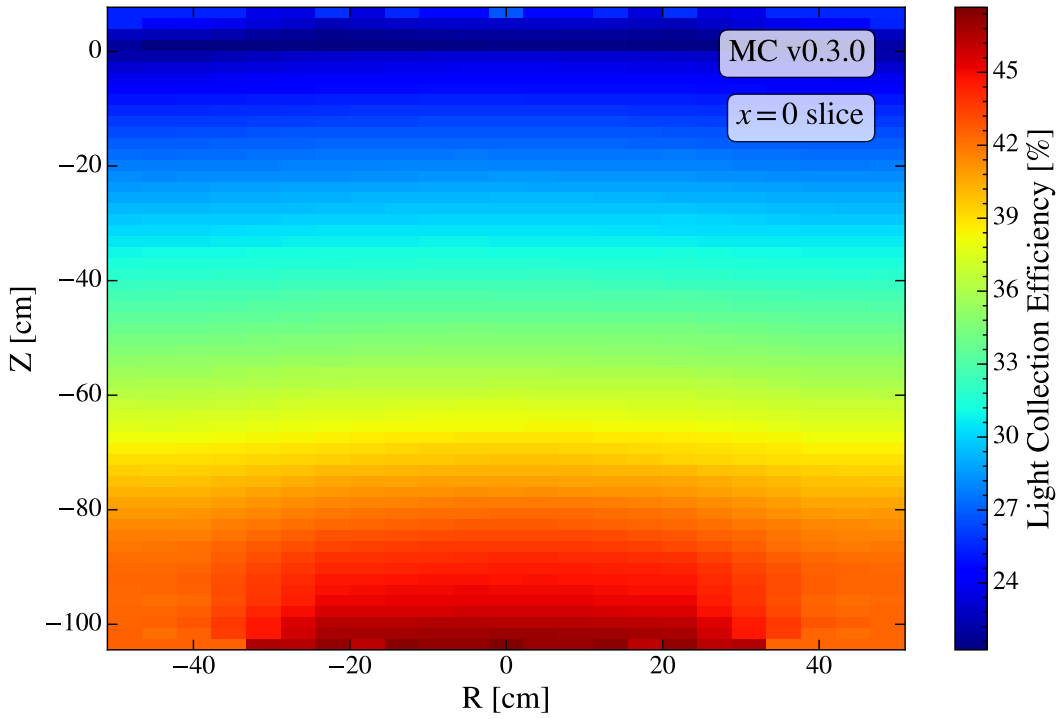

Figure 6.2: Slice of the LCE map through the middle of the simulated detector summed over all PMTs.

The resulting simulation is then stored as a LCE map for each PMT to be included in FAX. It is also possible to extract photon propagation times from the simulation to use them directly in FAX, replacing the current model. The derived summed LCE distribution for a slice of the detector is shown in figure 6.2 and AFT distribution in figure 6.3. Further LCE and AFT distributions for single PMTs are given in appendix A.5.1. Between MC version 0.3.0 and 1.0.1 are no changes regarding the performance of optical photon simulations introduced.

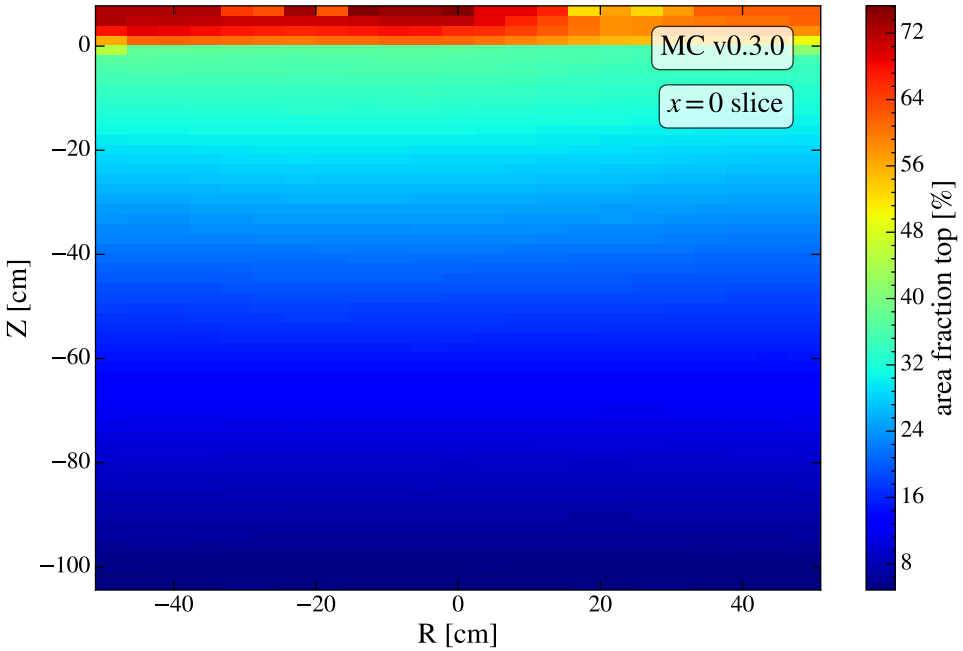

Figure 6.3: Slice of the AFT map through the middle of the simulated detector summed over all PMTs. Due to bin size the LXe/GXe interface appears to be at Z = 0 instead of 2.5 mm above the gate.

6.1.2 Per-PMT map for S2 photons

The per-PMT AFT maps for S2 photons are generated in the same way as the S1 photon maps, except for the photon generation. The S2 simulation uses 10^4 photons per event position in order to get a full PMT hit pattern for each event generated in the GXe below the anode, which is described as the S2 volume in figure 4.12. The resulting simulation is also converted to the FAX/PAX format and can be seen as the sum over all PMTs in figure 6.4. The higher AFT values at the edges of the TPC indicate regions with low statistics due to binning effects. An AFT map excluding 35 PMTs is given in figure 6.5. The exclusion of these PMTs leads to an decrease of the AFT from 63.16 % to 55.93 %. While the impact of the top PMTs can be directly seen, the bottom photons exhibits a broad signal, so that the AFT decreases uniformly by excluding bottom PMTs. Some AFT distributions for single PMTs are given in appendix A.5.2.

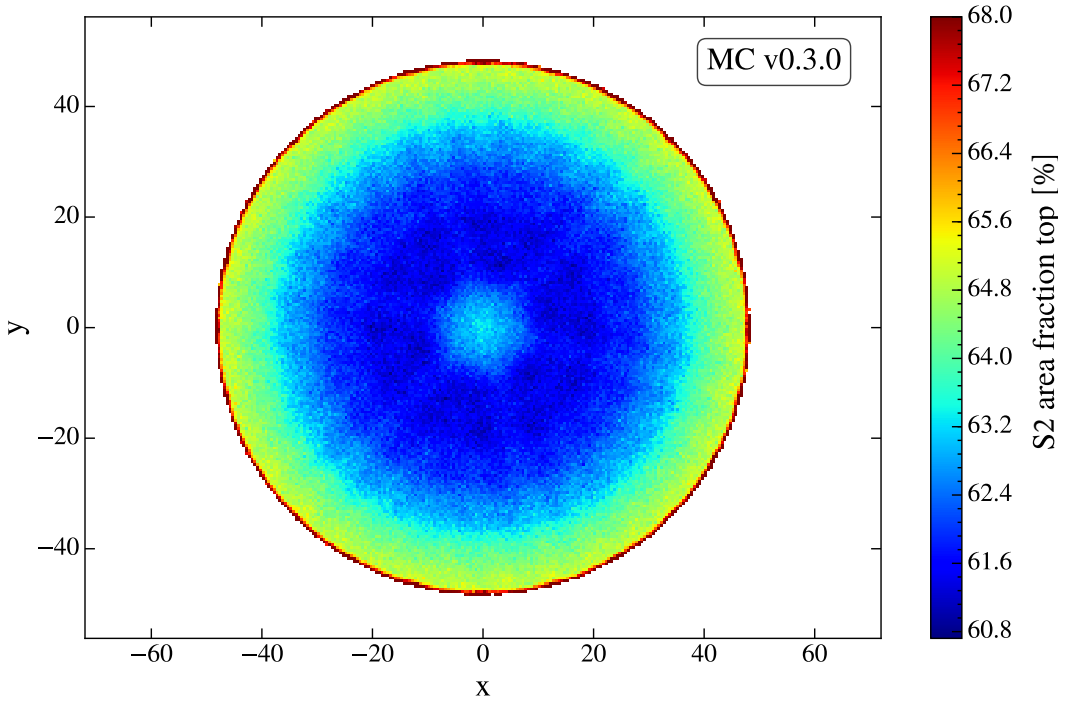

Figure 6.4: Distribution of the AFT for simulated S2 events. Each event contains the average AFT value of 10^4 simulated photons in the S2 area. A higher AFT value at the edges denotes bins with less statistics due to their size.

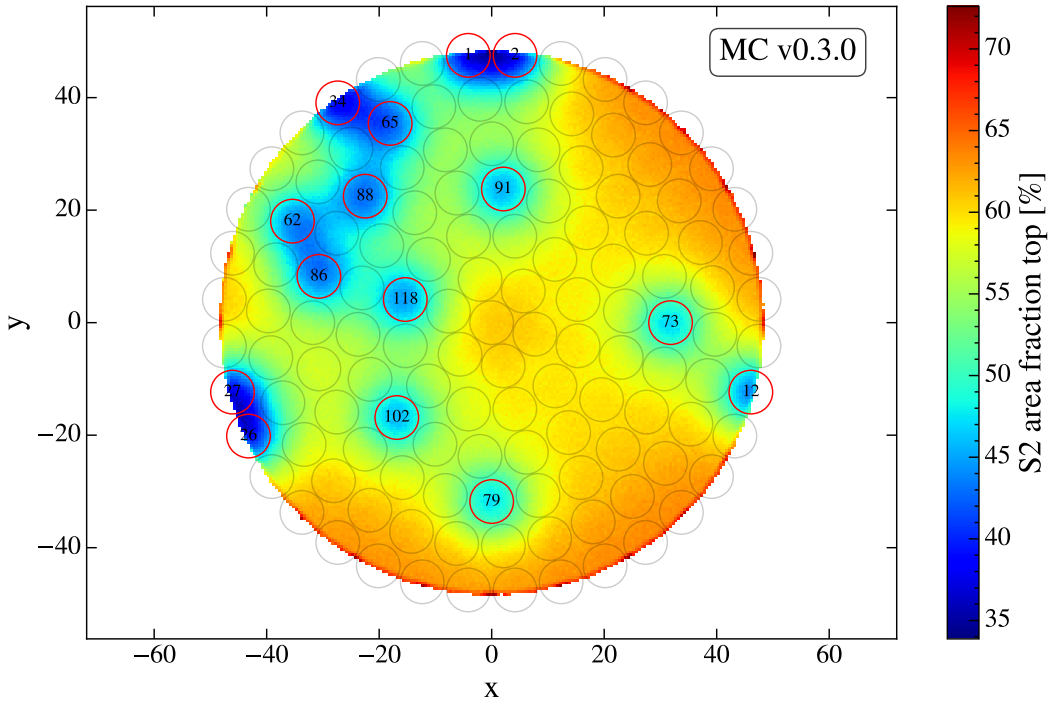

Figure 6.5: Distribution of the AFT for simulated S2 events as given in figure 6.4, excluding 35 PMTs in top and bottom. The excluded PMTs of the top array are marked by read circles.

6.2 Full Monte Carlo chain ^{83m}Kr simulation performance

The full MC chain, illustrated in figure 6.6, is tuned by many inputs from data measurements in order to match data measurements back to the level of waveforms. Various particle source types require a different treatment during the MC chain, resulting in a complex overall structure. The selection of the needed software modules is done by a so called *processing* script with respect to configuration files allowing the production of MC simulations without knowing the entire chain.

The presented optical photon simulations are using exclusively the GEANT4 stage in any available version. Sources like americium-beryllium (AmBe) or the neutron generator [50] (as implemented in GEANT4) are simulated using a GEANT4 version without NEST and a module named *nSort* before sending the charge and light yield to FAX.

The modules *nSort* and *nSort-py* are both converting the deposited energy obtained in GEANT4 to S1 and S2 signals, taken various electronic and nuclear recoil (ER and NR) models into account. Detector models used in *nSort*, described in [37], are outdated since new emission models regarding fits of *ScienceRun_0* measurements are developed. The new emission models are implemented in the module named *nSort-py* which will replace *nSort* in the future.

In addition, *nSort-py* allows to do an effective S1 and S2 simulation including the same data inputs as FAX and performing a macroscopic clustering. This effective

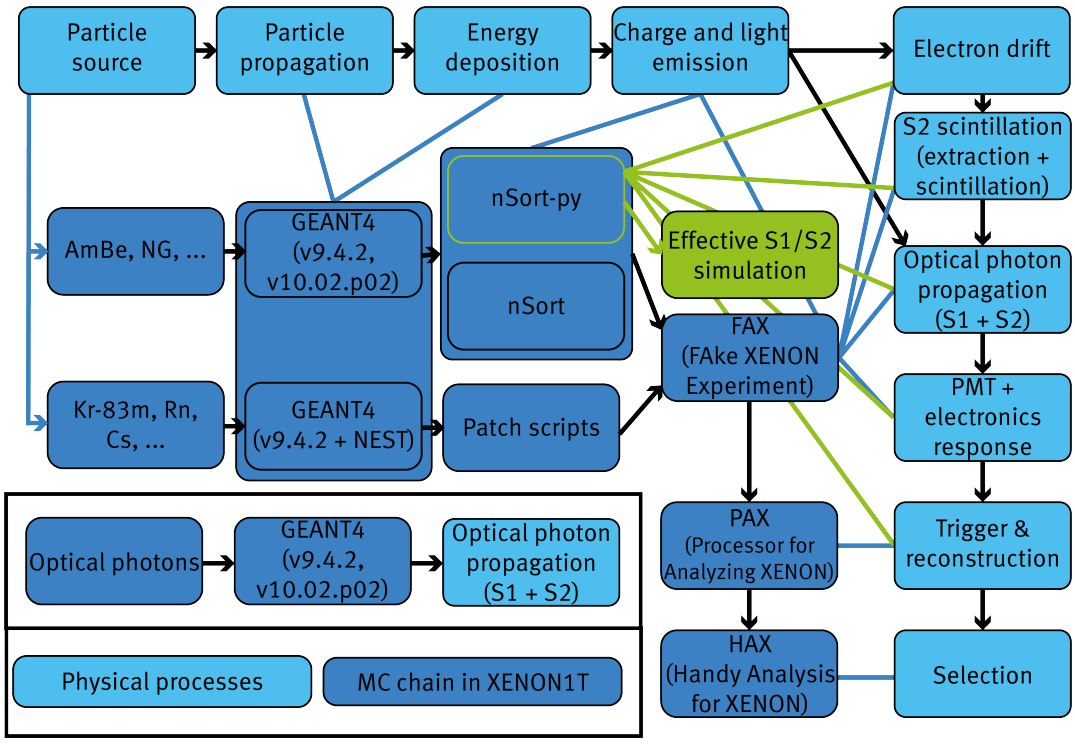

Figure 6.6: Full MC Chain including all submodules and analysis software tools connected to the corresponding physical processes in the real detector.

simulation is bundled with the GEANT4 module, but does not need the time consuming waveform simulation in FAX.
Other sources like ^{83m}Kr, ^{85}Kr, ^{220}Rn, ^{210}Pb or ^{212}Pb are not simulated using *nSort**. A module named *Patch scripts* converts the GEANT4 output of these sources to the FAX format and applies some special corrections for the isotopes such as splitting the 41.5 keV of ^{83m}Kr into two time separated lines. The prepared output from either *n-Sort** or *Patch scripts* are fed into FAX to simulate waveforms as seen in figure 6.7.

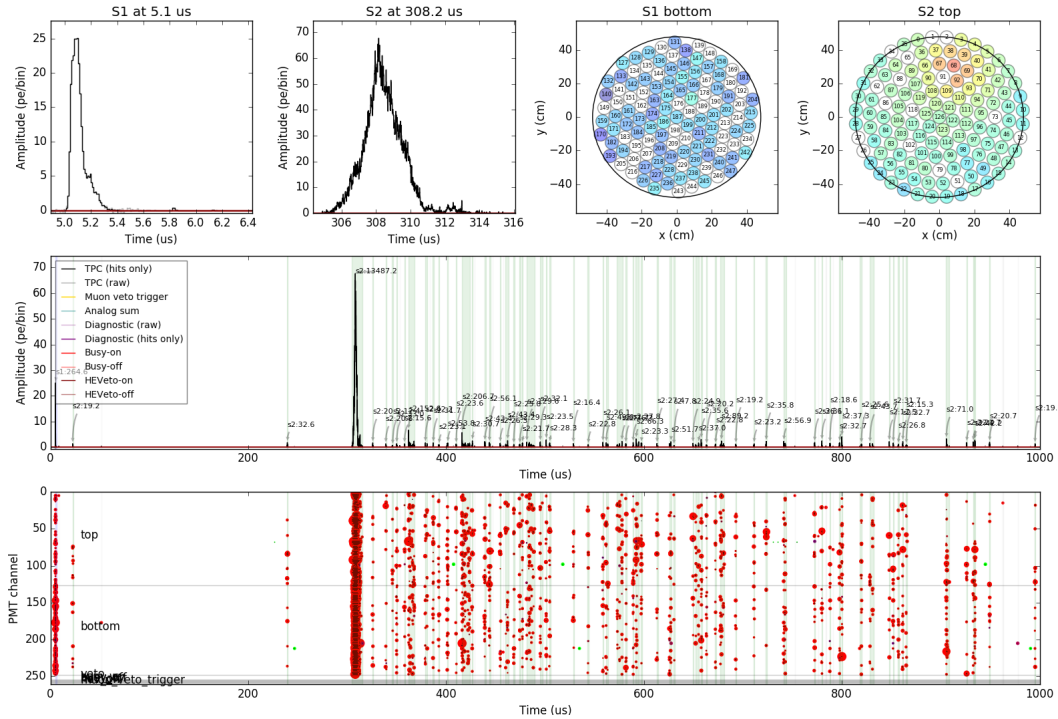

Figure 6.7: Example waveform of the full MC chain ^{83m}Kr simulation using MC version 1.0.1 and FAX/PAX version 6.8.0. A waveform from measured data is given in figure A.23.

In the following, the performance of a full MC chain ^{83m}Kr simulation is compared to actual data measurements. Within this comparison, some input parameters, which are fed into FAX by configuration files, are obtained from MC simulations and data. The

Table 6.1: Parameter settings in FAX different from the default configuration of version 6.8.0.

parameter	value/description
S1 patterns	per-PMT LCE map as before
S2 AFT	63.23 %
diffusion constant (LXe)	31.73 $\mathrm{cm^2/s}$
drift field	82 V/cm
electron drift velocity	1.335 µm/ns
electron lifetime LXe	550 µs

MC simulation is performed with MC version 1.0.1 and FAX/PAX version 6.8.0, while the calibration data is analyzed with PAX 6.6.5. Differences of these PAX versions are only including changes in data correction and thus do not affect the comparison. The PAX output is further processed with HAX version 1.5.0. The MC settings used in case of optical parameters are given by the MC version (as in table 5.1) and other parameters, which are different from FAX default are given in table 6.1.

Both, the MC data and experimental data are processed with a *DoubleScatter treemaker* that identifies events with a first and second interaction inside the detector. The resulting data selection includes events with separated ^{83m}Kr line signals and other interactions triggered by a different double scatter decay or noise. An energy distribution of measured events identified as $cS1_a$ and $cS1_b$, the signals corrected by the LCE map and electron lifetime, is given in figure 6.8. Signals generated by ^{83m}Kr are located in the green area, where the $cS1_a = 32.2\,\text{keV}$ and $cS1_b = 9.4\,\text{keV}$ are.

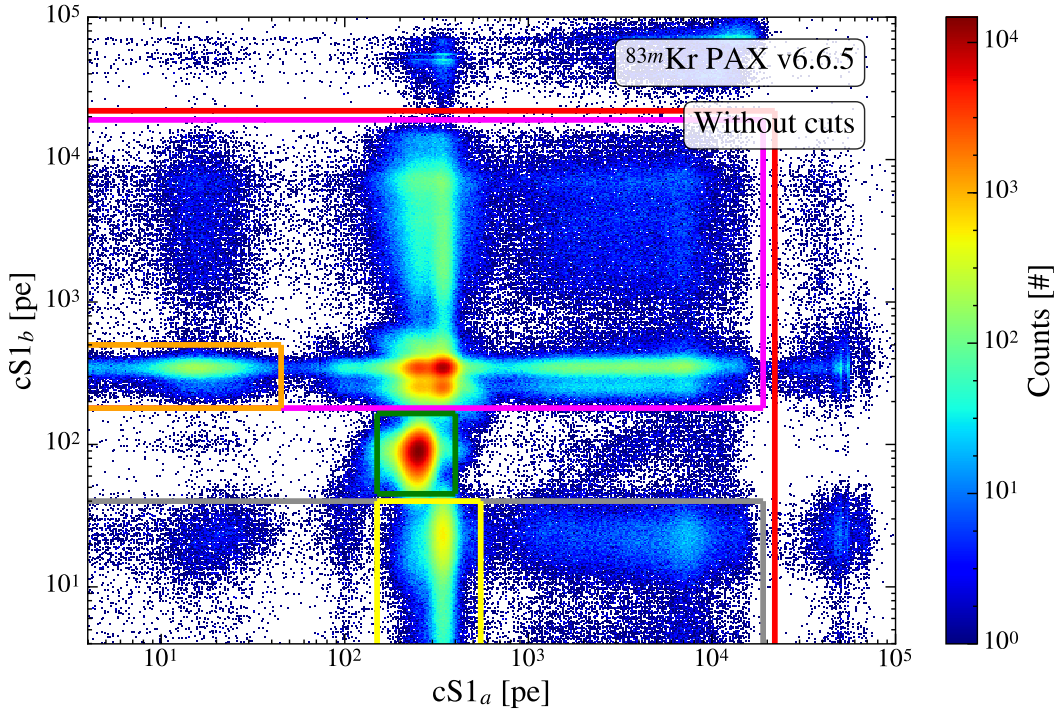

Figure 6.8: Distribution of the energy of events identified as $cS1_a$ versus $cS1_b$. The outer area (red) contains events from alpha decays, the pink area is due to pile-up events, where several signals overlay, the gray area contains afterpulses, the yellow ($cS1_a = 42.6\,\text{keV}$) and orange ($cS1_b = 42.6\,\text{keV}$) areas are triggered by noise and the green corresponds to the ^{83m}Kr signal ($cS1_a = 32.2\,\text{keV}$ and $cS1_b = 9.4\,\text{keV}$).

The ^{83m}Kr can be isolated from the processed data by selecting scatters happening in a specific time window and limiting the amount of coincidental PMTs. The timing cut excludes events with a time difference between $S1_a$ and $S1_b$ less than 600 ns and more than 2000 ns which are mostly pile-up events (see figure A.27). Afterpulses are removed by excluding events with less then three and more than 30 contributing

PMTs to the $S1_b$ signal (see figure A.26). These two selections reduce the amount of selected events in case of the MC from $5.9 \cdot 10^5$ to $1 \cdot 10^5$ (18 %) and for actual data from $6.6 \cdot 10^6$ to $1.5 \cdot 10^6$ (23 %). The cutted event selections are shown in figure 6.9.

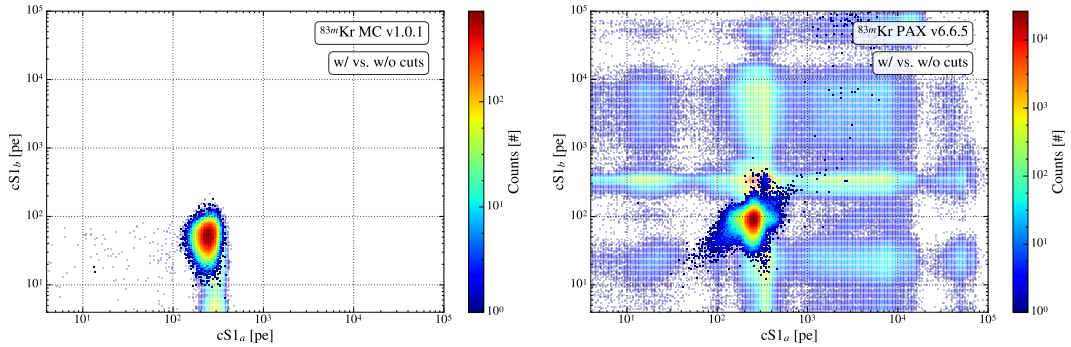

Figure 6.9: Event selection of the MC simulation (left) and calibration data (right) for ^{83m}Kr (for uncorrected signals see figure A.24). The grayed out bins denote the event selection before applying timing and contributing channels cuts.

The full MC simulation of ^{83m}Kr is mainly tuned by optical observables, which are adjusted by the per-PMT LCE maps from section 6.1. The performance of the simulation regarding the optical inputs can be benchmarked by comparing the obtained S1 and S2 signals. First, the correction and distribution of the S1 signal is given in figure 6.10. The distribution of a corrected signal along the Z-position (height) will exhibit a straight line with a certain mean and width, as observed for the MC simulation with a mean value of 243.64 pe and a width of 128.83 pe. The distribution for actual data has a mean of 252.16 pe, varying close to the gate mesh by 20 pe. This denotes that the implemented energy corrections for measured data needs further tuning. Also the width of the cS1 signal becomes smaller with increasing depth, revealing an average width of 90.09 pe. The population of events outside of the signal width with more than 350 pe in cS1 appears due to basic cuts, so that a neglectable amount of background events are still present in the data selection. It can be concluded that

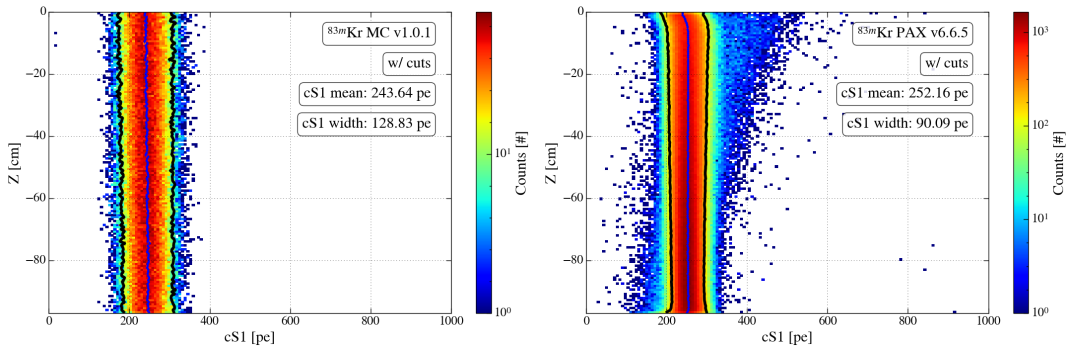

Figure 6.10: Energy of the corrected S1 signal for MC simulation (left) and data (right) along the Z-position inside the TPC, where $Z = 0$ corresponds to the gate mesh level.

the simulated cS1 signal matches the data and that this match will improve with further corrections in new PAX versions, which are already available.

Background events are also visible in the following figures and will not be further discussed. The S1 signal also matches in terms of the AFT the data, as seen in figures 6.11 and 6.12. The mean of the signals is the same as given in figure 6.10. Size and width of the S1 AFT is matching in both figures, indicating the correct implementation and interpolation of the per-PMT LCE maps from section 6.1.

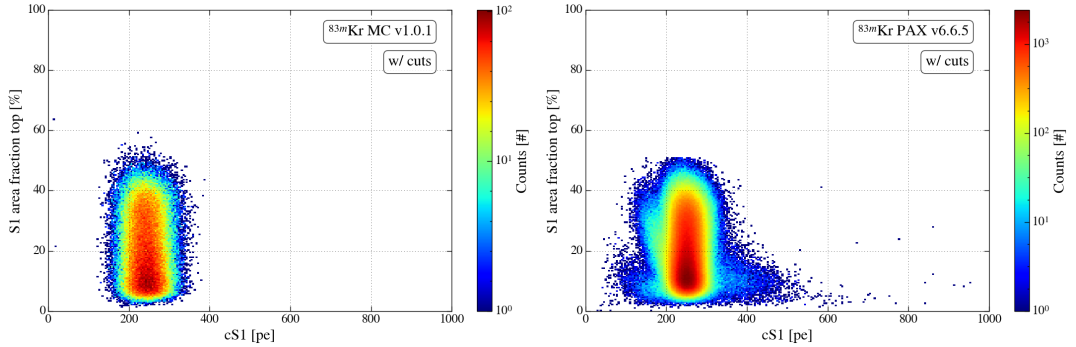

Figure 6.11: S1 AFT per energy in photoelectrons for MC simulation (left) and data (right).

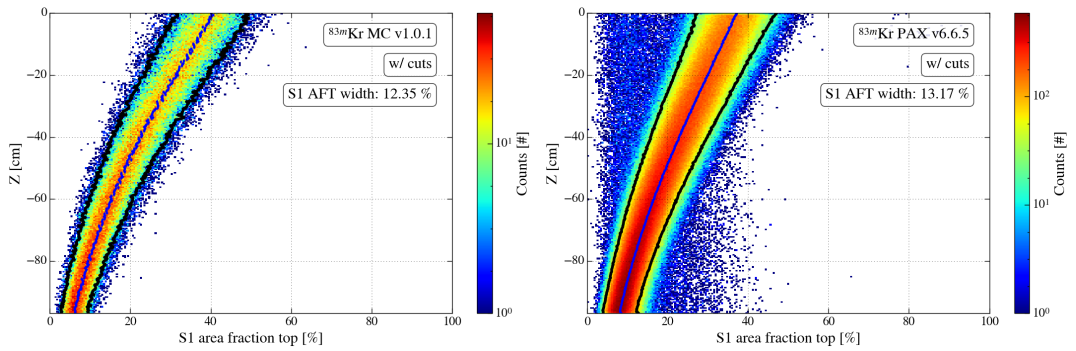

Figure 6.12: S1 AFT for MC simulation (left) and data (right) along the Z-position, inside the active TPC volume.

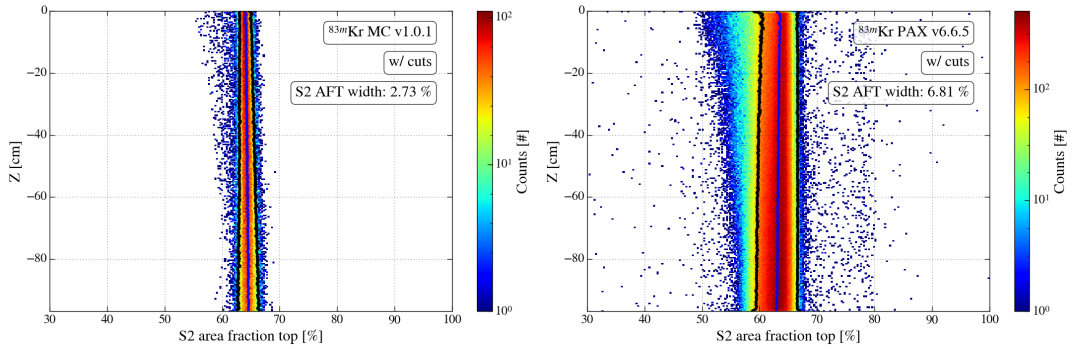

Figure 6.13: S2 AFT for MC simulation (left) and data (right) along the Z-position, inside the active TPC volume.

The comparison of the S2 AFT distribution exhibits a difference between MC simulation and data measurement, given in figure 6.13. This is due to a not adjusted S2 AFT values in the configuration file. The mean and width is simulated using this file and considering the S2 per-PMT map only for hit probabilities of each PMT.

Most of the discussed optical observables can be summarized in the comparison of the *ly* for the $S1_a$ signal, given in figure 6.14. Both *ly* maps are also shown in figure A.32, revealing a highest value of around 10.7 pe/keV for the bottom and 5.5 pe/keV for the top TPC. The $S1_a$ *ly* map is around 0.4 pe/keV higher in the entire TPC, which corresponds to a difference of less than 5 %. Also the S1 AFT maps given on figure A.33 are matching within this range (see figure A.34).

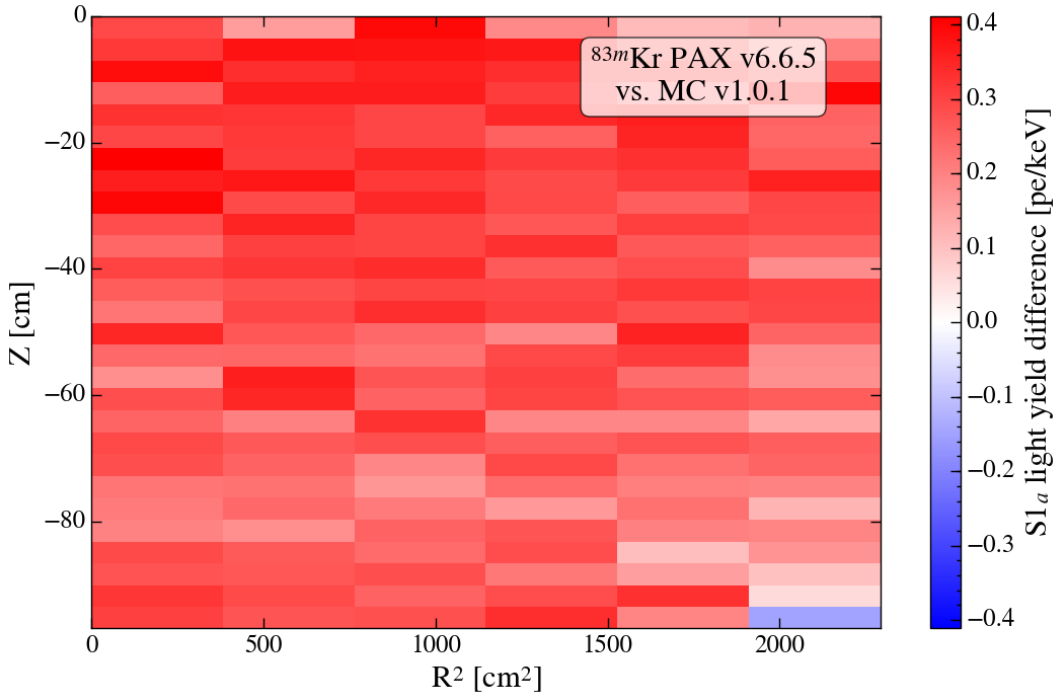

Figure 6.14: Difference of the data analysis of PAX version 6.6.5 to MC simulations for ^{83m}Kr, both maps are shown in figure A.33.

Taking all results of the comparison together, the XENON1T MC can be tuned to match actual data measurements with PAX version 6.6.5. This could be achieved by tuning the optical parameters in GEANT4 with ^{83m}Kr data measurements and using this information as configuration parameters and as per-PMT maps in FAX. This procedure requires a regeneration of the matched optical parameters and MC maps for every new PAX version that introduce changes in clustering, corrections and position reconstruction. A further comparison of the per-PMT maps will be possible as soon as the runtime of all ^{83m}Kr calibrations in XENON1T for a single detector configuration is long enough to obtain data driven per-PMT maps.

The comparison presented in this chapter is still using the *effectively* matched optical parameter settings. The obtained result will improve further by matching the optical

observables of GEANT4 and data measurements without having to manipulate an optical parameter. One could achieve this matching by introducing a new way of simulating S2 photons, as described in the following.

7 Advanced S2 optical photon simulations

This chapter introduces a new method of simulating S2 photons for optical parameter comparisons to avoid the *effective* matching approach discussed in chapter 5. Prior to this chapter, optical photons from the S2 signal are generated in a S2 volume given in figure 4.12. This leads to a low GXe absorption length which is not motivated by hypotheses and which was expected to match the absorption length of LXe. The solution of this problem can be given by using COMSOL Multiphysics® simulations.

The COMSOL Multiphysics® simulation package allows to simulate the generation of S2 photons. It is a general-purpose software platform, based on advanced numerical methods, for modeling and simulating physics-based problems [51]. This modular software allows to generate an electric field simulation of a segment of the XENON1T TPC. Each simulated component can be configured to match the actual physics of

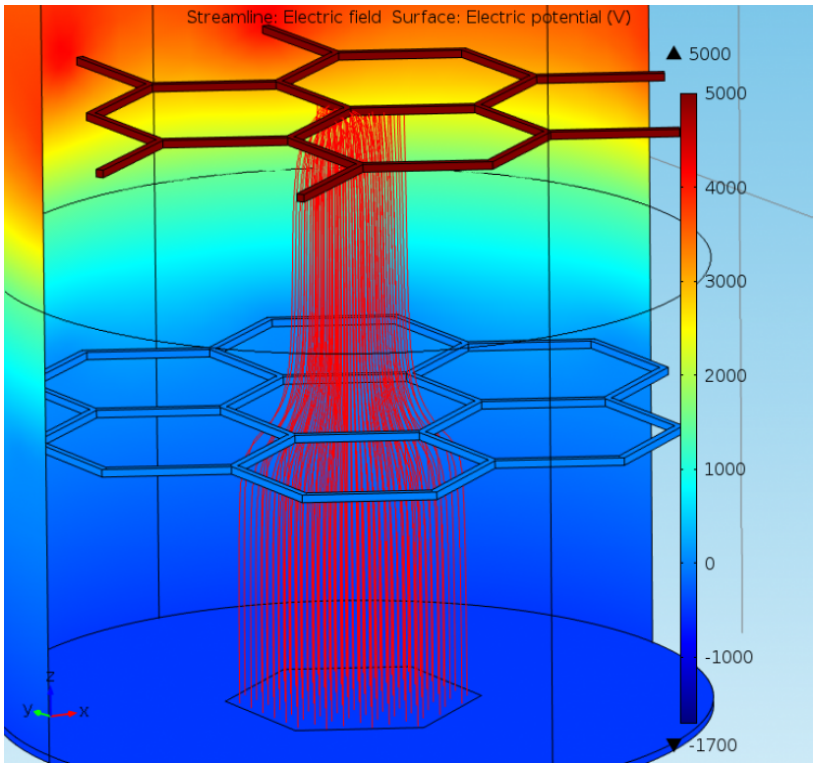

Figure 7.1: Front view of the upper mesh electric field simulation in COMSOL Multiphysics®. The color represents the electric potential in volts and streamlines are shown in red. The circle in between the gate mesh (blue) and anode (red) represents the interface of GXe and LXe.

the experiment. Here, a one mesh cell in the upper TPC is simulated, as given in figure 7.1. This simulation includes the gate mesh at 0 kV and the anode at 5 kV, as well as the LXe and GXe volumes. Electrons reaching the gate mesh are redirected according to the streamlines and focused towards the middle of a gate mesh hexagon, which corresponds to the connection point of three hexagons in the anode mesh. This focusing effect is also shown in figure 7.2, where the drift velocity and thus the S2 scintillation probability is given for various positions in between the gate mesh and anode. In this consideration, the sagging of the meshes due to their size is not considered. The initial position of electrons is given by black dots, 10 mm below the gate mesh. The volume, in which a S2 signal can be generated, is confined by the GXe for which the drift velocity is given in a way, that the highest velocity is visible for each position. From this can be concluded, that the area in which S2 photons are generated is much smaller than the hexagonal cell and that the area with the highest drift velocity and thus highest scintillation probability is mostly covered by the anode wire. Both has an influence on the simulated AFT.

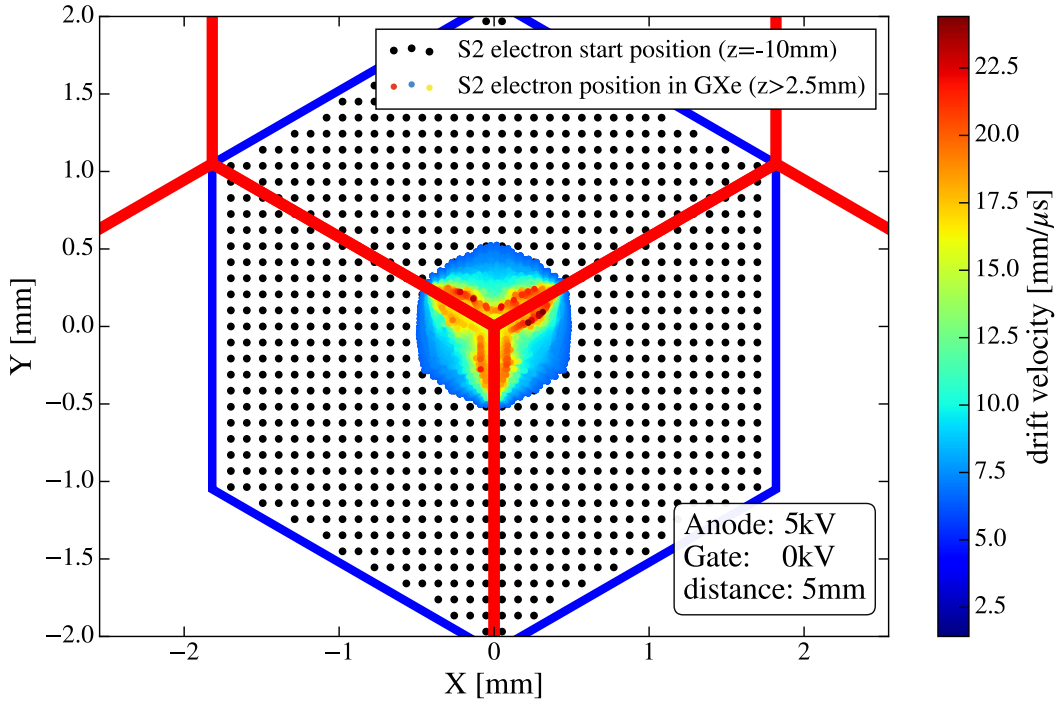

Figure 7.2: Simulation of the electric field streamlines for one cell of the upper TPC meshes in COMSOL Multiphysics®. The GXe/LXe interface is assumed to be in the middle of the meshes at z=2.5 mm, where the gate mesh is shown in blue and the anode in red.

Previously, the GXe absorption length was lowered to 50 cm (see table 5.1) in order to adjust the S2 AFT value to match the one observed in data measurements. As pointed out here, the simulation of S2 photons in a thin disk below the anode (seen in figure 4.12) is not reflecting the actual S2 scintillation process. The full area of the hexagonal cell is used to generate photons which are directly detected by

the top PMTs, increasing the AFT value. This simulation process can be improved by imitating the S2 generation in GEANT4 accordingly to figure 7.2, which should lead to an equal AFT value at a higher GXe absorption length. A brief check of this hypothesis is performed by adding the actual mesh structure, named *detailed meshes* (see section 4.2.2), to the GEANT4 simulation geometry (see figure 4.7) and simulating S2 photons in a mesh-like volume right below the anode (green volume in figure 7.3). This new S2 photon generation volume is also shown in figure 7.4 as a green mesh. A comparison of simulations with thin disks to detailed meshes in appendix A.6 shows that the thin disk approach is valid.

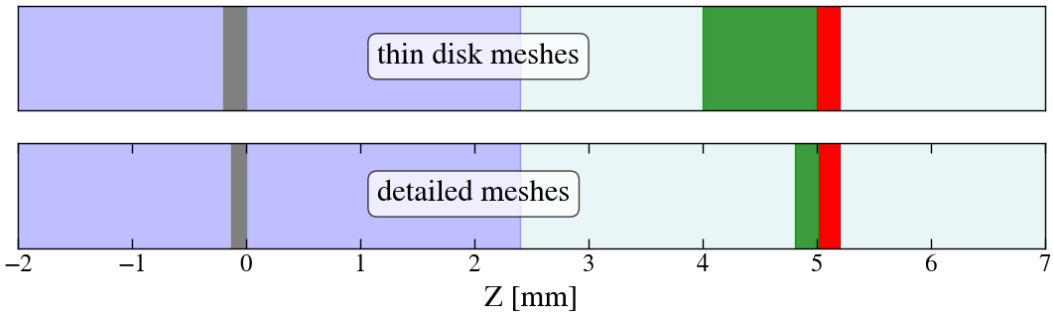

Figure 7.3: Implementation of the meshes in GEANT4 for both approaches. The LXe and GXe is depicted by dark and light blue areas in which the gate mesh (gray), S2 generation volume (green) and anode (red) is placed. The observer is looking up from below on to the top PMT array. The gate mesh is depicted by light gray, the top screening mesh by dark gray, the anode by red and the S2 generation volume by green color.

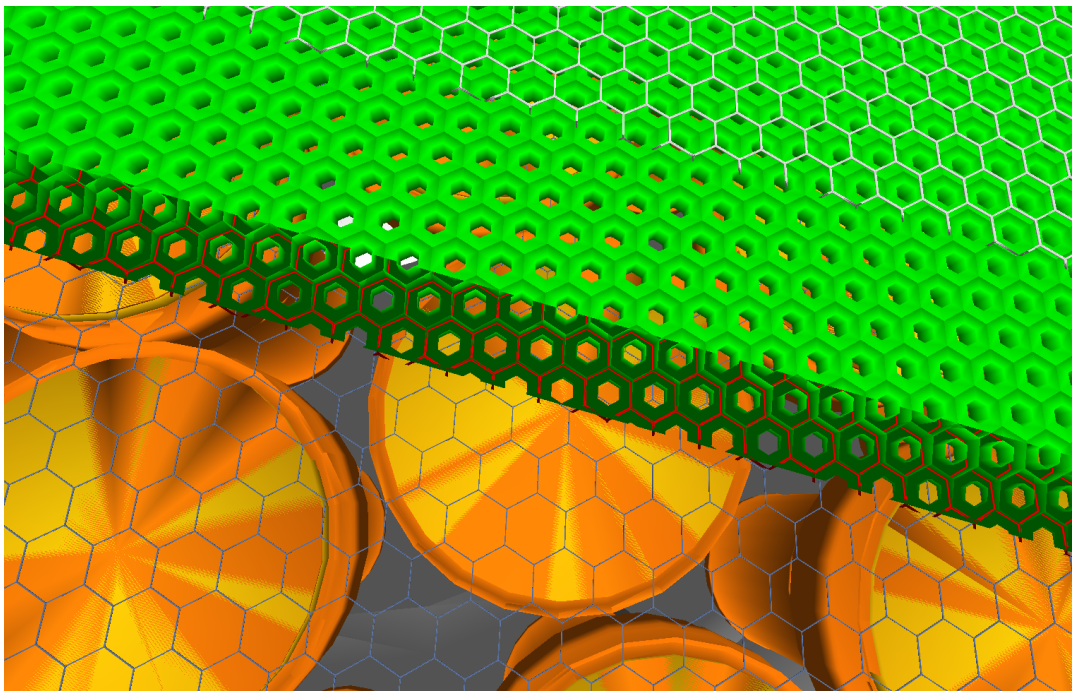

Figure 7.4: Implementation of the S2 generation volume (green) using a detailed mesh structure in MC v1.0.1.

Simulations with S2 photons, generated in a mesh volume with a GXe absorption length of 100 m, are matching the simulation results previously obtained using a thin disk generation volume with an absorption length of 50 cm (see appendix A.6). The GXe absorption length is no longer needed to adjust the S2 AFT value and can be set to the estimation in [37]. This S2 simulation approach is still not representing the actual S2 generation volume, that needs to be defined accordingly to the field distribution in figures 7.1 and 7.2. Further investigation of how this implementation can be achieved in GEANT4 are needed.

8 Conclusion and outlook

In the scope of this thesis optical simulations of the XENON1T experiment were produced and compared to experimental data from ^{83m}Kr calibrations. The introduction highlighted the overall role of optical simulations within the XENON1T MC chain and for data processing.
Chapter two focused on observational evidence for dark matter, such like galaxy rotation curves, cluster collisions and the CMB. Weakly interacting massive particles were introduced as the most promising candidate for direct detection dark matter experiments.
The XENON Dark Matter Project and the detection principle of a dual phase TPC were described in chapter three. Leading experiments in the field of direct WIMP detection are based on dual phase TPCs filled with noble liquids such as xenon. Liquid xenon is used as target material due to scalability, self shielding and purity. The XENON1T detector, part of the XENON Dark Matter Project, is the first operating multi-ton dual phase xenon TPC. The signal generation mechanics of the light and charge channels, as well as the detector design have been outlined.
Chapter four introduced the GEANT4 simulation package of the XENON1T detector, its implemented geometry and optical simulations. The detector geometry was described focusing on components that define the optical response and examine their implementation. The model of the PTFE surfaces was revisited, concluding that a dependence of the incident angle for all reflection types is currently neglected in GEANT4. Only the distribution of optical photons would be affected, preserving the total amount of detected photons. Furthermore, the implementation of the mesh model has been extended from a *thin disk* approach, where the electrode meshes are defined as thin disks with a refraction index imitating the dependence of incident photon angles, to a detailed model that accurately imitates the geometry of the mesh wires. The detailed implementation was used to validate the prior approach with thin disks, showing that both approaches yield identical results. The PMT model was described pointing out that simulations assume that the photo sensors collect every photon hitting the photocathode. Actual PMTs in the XENON1T experiment exhibit an efficiency of about 30 %. Therefore, the efficiency has been modeled with respect to the QE, increase of the QE for temperatures around −100 °C and the CE. Further analyses will have to investigate if the simulated angular response of the PMTs is equivalent to the one extracted from data.

At last, optical simulations have been evaluated calculating the LCE in certain detector regions depending on the signal type that has been simulated. The impact of optical parameters, namely liquid xenon refraction index, liquid xenon Rayleigh scattering length, the liquid and gaseous xenon absorption length and the reflectivity of PTFE, were investigated for S1 and S2 signals. This showed that each parameter changes the light collection as expected from theory.

Chapter five compared optical simulations directly with experimental data and developed a new method of matching them. Previously published simulations of the XENON1T experiment were based on optical parameter assumptions that were made before the construction of the experiment in 2015. Calibration measurements with ^{83m}Kr between February and August 2017 allow to directly compare these a priori assumptions to actual measurements.

Optical simulations have been corrected by PMT efficiencies and excluding PMTs that are not used in measurements. The obtained LCE and rLCE maps from simulations are compared to experimental data, showing that the optical parameters, used for simulations prior to this work, are not matching the actual detector response.

The deviation of up to 0.15 rLCE and 16 % AFT was adjusted by a matching algorithm that fits optical parameters to data which is trained by simulation samples. This algorithm revealed a best matching simulation with a difference of up to 0.04 rLCE and 2 % AFT. The fitted optical parameters gave a liquid xenon refraction index of 1.69 and a gaseous xenon absorption length of 50 cm, while the liquid xenon absorption length was fitted to 50 m. This unphysical mismatch has been resolved by a new method for simulating S2 photons, as described in the last chapter. The fitted parameters were implemented in the XENON1T GEANT4 simulation and used for further simulations.

Chapter six described the generation of per-PMT maps and the dependence of the full MC chain on optical simulations. The position reconstruction algorithms as well as the FAX package rely on per-PMT LCE maps. These maps describe the light collection from every position in the TPC for each PMT and thus the probability of a photon to reach a certain PMT.

The performance of the full MC chain was tuned with per-PMT maps and evaluated by a direct comparison with data. Therefore, a full simulation of the ^{83m}Kr calibration source was performed. For this purpose, a dependence of the light and charge yield on the electric field was implemented in the full MC chain. This implementation will also allow to perform further studies of field variations in XENON1T. The simulation of the electric field is based on NEST calculations. Both the simulated and experimental data were processed with the same PAX version to exclude dependencies of the optical observables on the data processor. The comparison showed that the optical observables for S1 signals, such as the energy distribution or AFT along the z-position, match while the simulated S2 AFT distribution has a 4 % smaller width and needs further tuning.

The full chain simulation used photon timing distributions implemented in FAX by approximated functions. These distribution have to be further adjusted by photon times directly extracted from per-PMT simulations with GEANT4.

The position reconstruction algorithms currently use PMT hit distributions obtained from the generated per-PMT maps. This approach does not take the detector conditions, such as afterpulses, trigger thresholds or the actual resolution into account. The algorithms are based on relative PMT hits, neglecting any energy dependence of the light collection. The training of these algorithms could be improved by performing optical simulations with FAX. This means, that optical simulations with GEANT4 have to be used in FAX to distribute photons and to generate actual waveforms. This new approach of simulating optical photons would use all aspects of the actual detector response which have already been included in FAX, such as energy dependencies, electronics and PMT effects.
Further improvements of the optical simulations in GEANT4 as well as in FAX can be achieved by simulating S2 photons in an volume motivated by electric field simulations. It was pointed out in chapter seven, that the fitted optical parameters depend on the actual generation volume of S2 photons. This volume has been determined by COMSOL Multiphysics® simulations. A full description of this generation volume can only be achieved by simulating the electric field of the XENON1T detector, including collisions of the electrons with xenon atoms. This steps requires the use of additional simulation software. The obtained generation volume will be a crucial input to future optical simulations, which will improve the full MC chain and position reconstruction methods.

A Appendix

A.1 Optical simulations of the XENON1T detector

The definition of the S1 and S2 optical photon generation volumes as seen in figure 4.12, used in GEANT4 is given in listings A.1 and A.3.

Listing A.1: Definition of the S1 optical photons volume (LXe volume) to which they are confined. The $z = 0$ level is defined as the gate mesh position.

```
/xe/gun/particle opticalphoton
/xe/gun/energy 6.98 eV

/xe/gun/type Volume
/xe/gun/shape Cylinder
/xe/gun/center 0. 0. -522.3 mm
/xe/gun/halfz 522.3 mm
/xe/gun/radius 479.25 mm
/xe/gun/confine LXe

/analysis/settings/setPMTdetails true
```

Listing A.2: Definition of the thin disk S2 optical photons volume (GXe volume) to which they are confined. The $z = 0$ level is defined as the gate mesh position.

```
/xe/gun/particle opticalphoton
/xe/gun/energy 6.98 eV
/xe/gun/numberofparticles 10000

/xe/gun/type Volume
/xe/gun/shape Cylinder
/xe/gun/center 0. 0. 4.5 mm
/xe/gun/halfz 0.5 mm
/xe/gun/radius 481.25 mm
/xe/gun/confine GXe

/analysis/settings/setPMTdetails true
```

A.2 Optical parameters of materials

The influence of optical parameters on the average LCE and AFT is discussed in [**?**], the following section will analyze the behavior along the Z-position for a small selection of possible parameter values. The simulations used for this analysis are generated by simulating 10^7 events in GEANT4 version 1.0.1 and varying a single optical parameter. For each event is one 7 eV photon generated inside the LXe volume. The macros used for these simulations are given inside the XENON1T MC simulation code repository, implemented as in listings A.1 and A.3 (*preinit_TPC.mac*, *setup_optical.mac* and *run_optPhot.mac*).

Listing A.3: Default optical parameter settings used for parameter influence studies. This parameters are also called initial assumption in table 5.1 and [37].

```
1  /Xe/detector/setTeflonReflectivity 0.99
2  /Xe/detector/setGXeTeflonReflectivity 0.99
3  /Xe/detector/setLXeAbsorbtionLength 50 m
4  /Xe/detector/setGXeAbsorbtionLength 100 m
5  /Xe/detector/setLXeRayScatterLength 30 cm
6  /Xe/detector/setLXeRefractionIndex 1.63
7
8  /Xe/detector/setTopScreeningMeshTransparency 0.945
9  /Xe/detector/setBottomScreeningMeshTransparency 0.945
10 /Xe/detector/setAnodeMeshTransparency 0.929
11 /Xe/detector/setGateMeshTransparency 0.929
12 /Xe/detector/setCathodeMeshTransparency 0.96
```

A.2.1 Liquid xenon refraction index

The LXe refraction index can be adjusted in GEANT4 by the messenger function */Xe/detector/setLXeRefractionIndex*. The following figures show the evolution of the LCE and AFT along the Z-position for a selection of parameter values.

It can be seen, that for a refraction index of 1.56 the amount of detected photons by the top PMTs out of the upper part of the LXe increases, but also that more photons are detected out of the bottom TPC. The increase of the light detected in the bottom PMTs is only visible for refractive indices smaller than the one for the PMT quartz window (1.59) which is a strong evidence that reflection on the window is affecting the LCE in other cases.

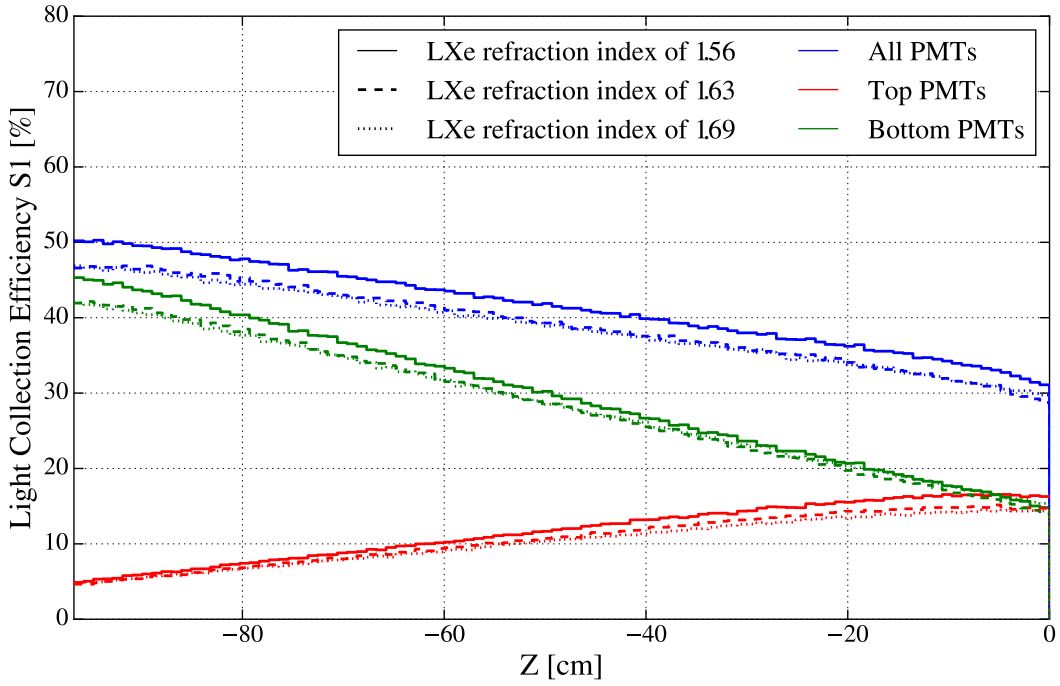

Figure A.1: Evolution of the LCE for S1 photons along the Z-position in the TPC. An total increase of the LCE for a LXe refraction index of 1.56 is obtained, which is divided by the PMT array for the top and bottom TPC.

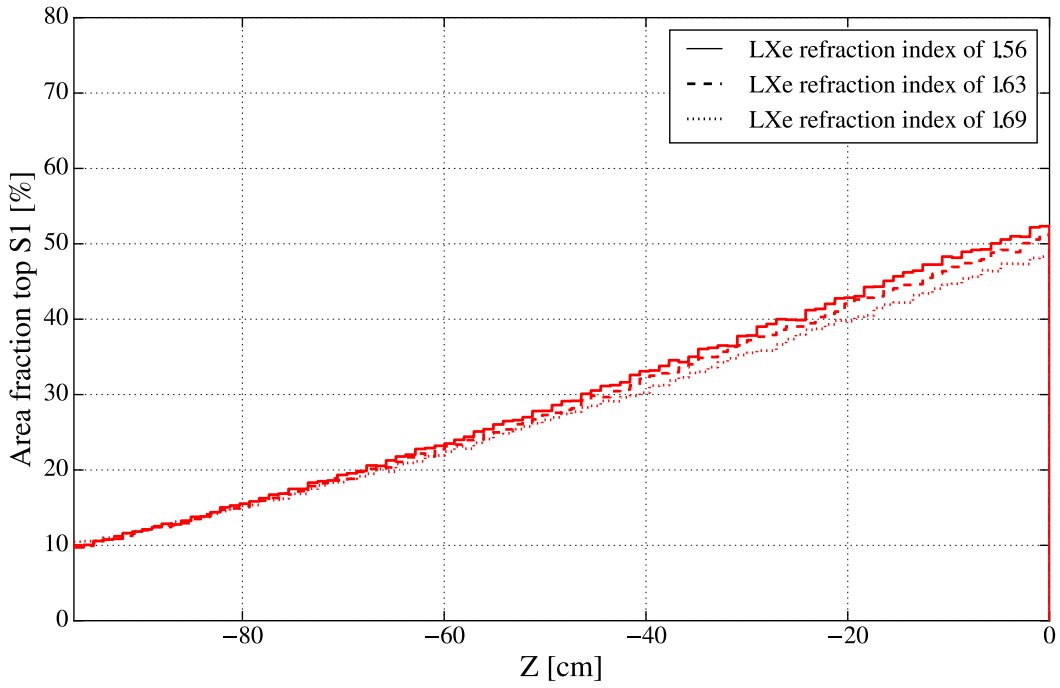

Figure A.2: Evolution of the AFT for S1 photons along the Z-position in the TPC.

A.2.2 Liquid xenon Rayleigh scattering length

The LXe Rayleigh scattering length can be adjusted in GEANT4 by the messenger function */Xe/detector/setLXeRayScatterLength*. The following figures show the evolution of the LCE and AFT along the Z-position for a selection of parameter values.

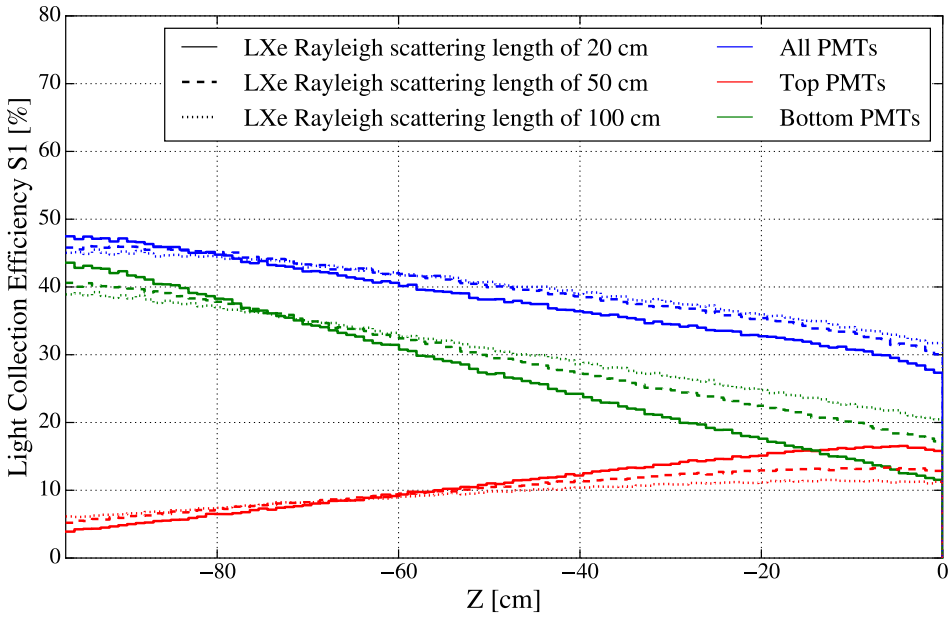

Figure A.3: Evolution of the LCE for S1 photons along the Z-position in the TPC.

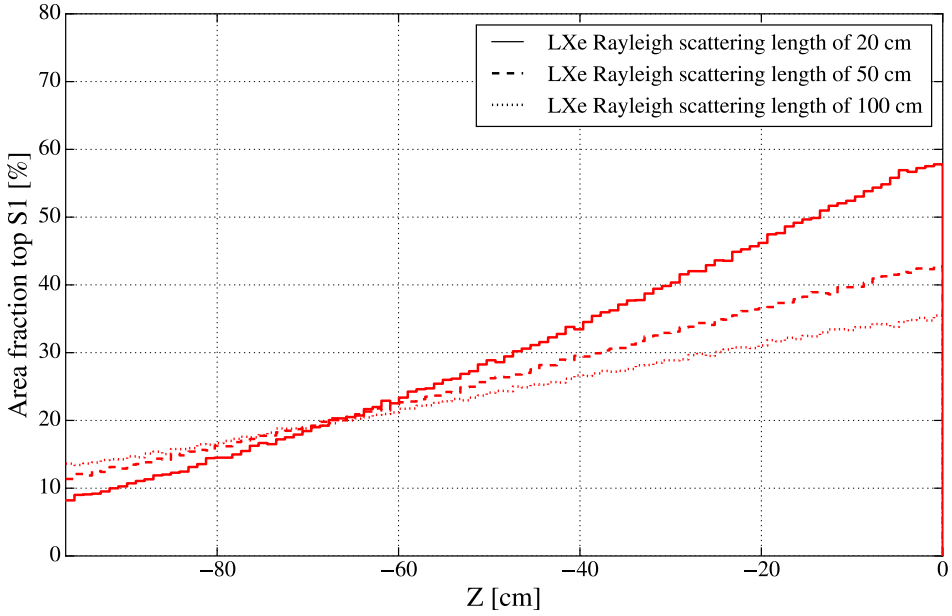

Figure A.4: Evolution of the AFT for S1 photons along the Z-position in the TPC.

A.2.3 Liquid and gaseous xenon absorption length

The xenon absorption length can be adjusted in GEANT4 by the messenger functions */Xe/detector/setLXeAbsorbtionLength* and */Xe/detector/setGXeAbsorbtionLength*. The following figures show the evolution of the LCE and AFT along the Z-position for a selection of parameter values.

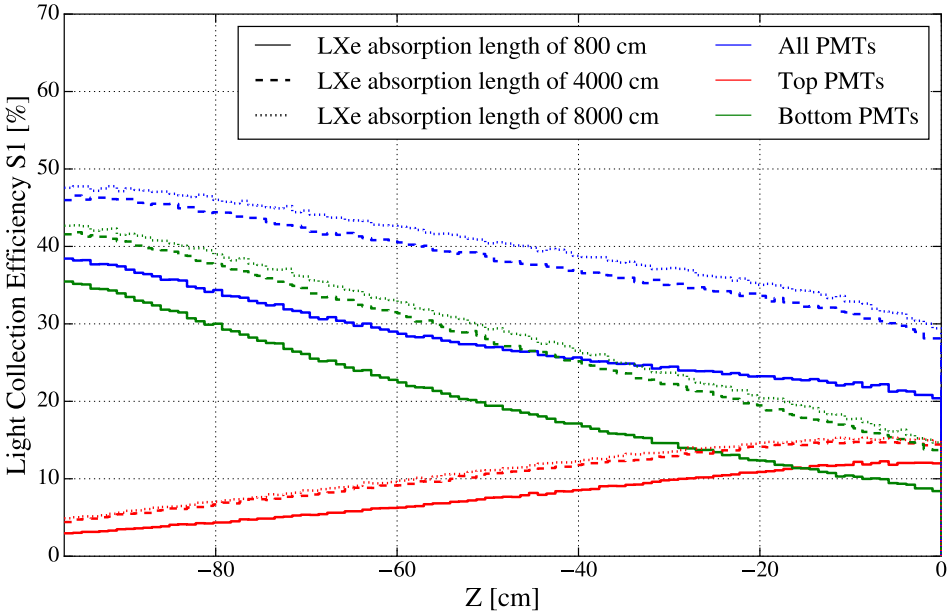

Figure A.5: Evolution of the LCE for S1 photons along the Z-position in the TPC.

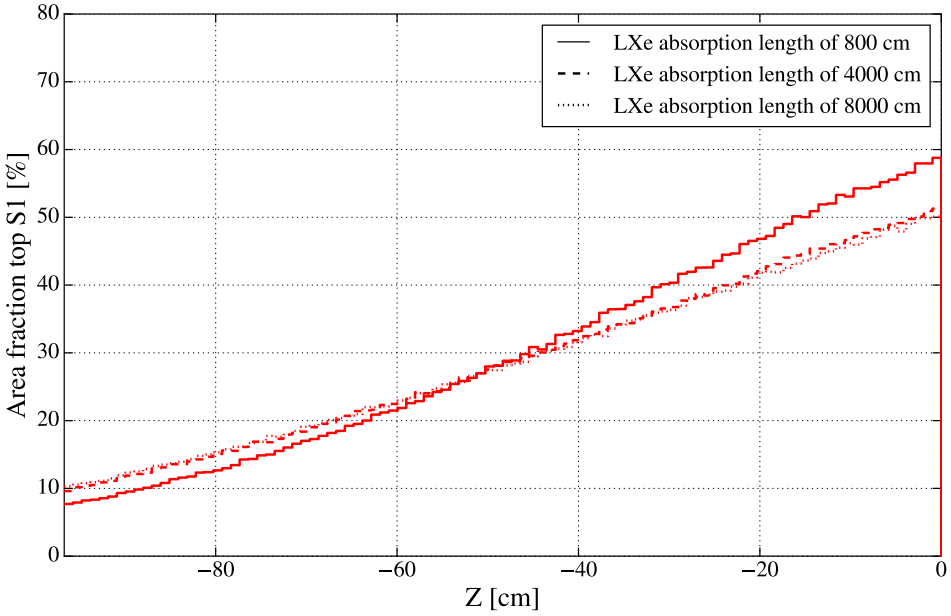

Figure A.6: Evolution of the AFT for S1 photons along the Z-position in the TPC.

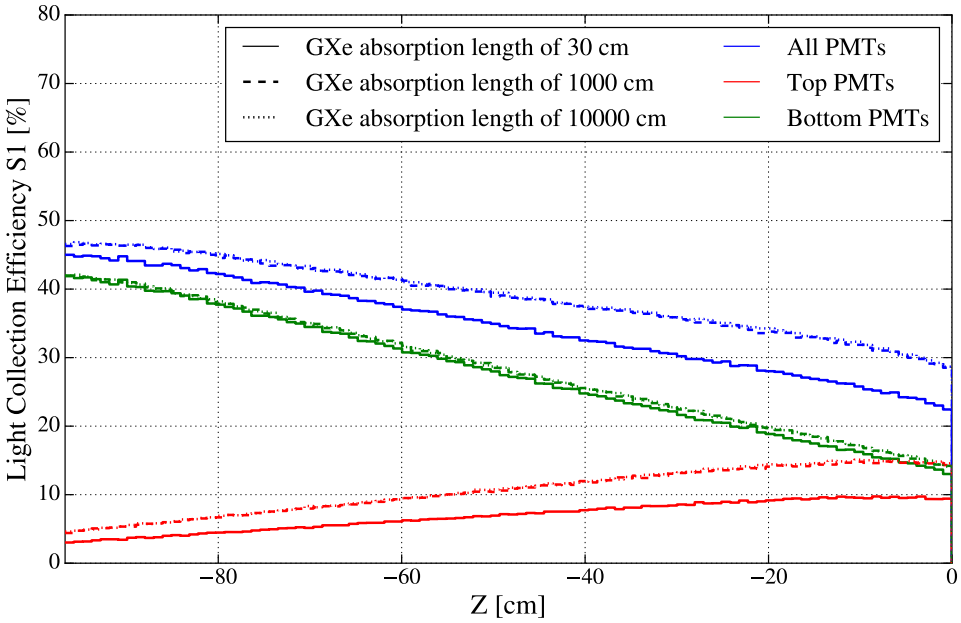

Figure A.7: Evolution of the LCE for S1 photons along the Z-position in the TPC.

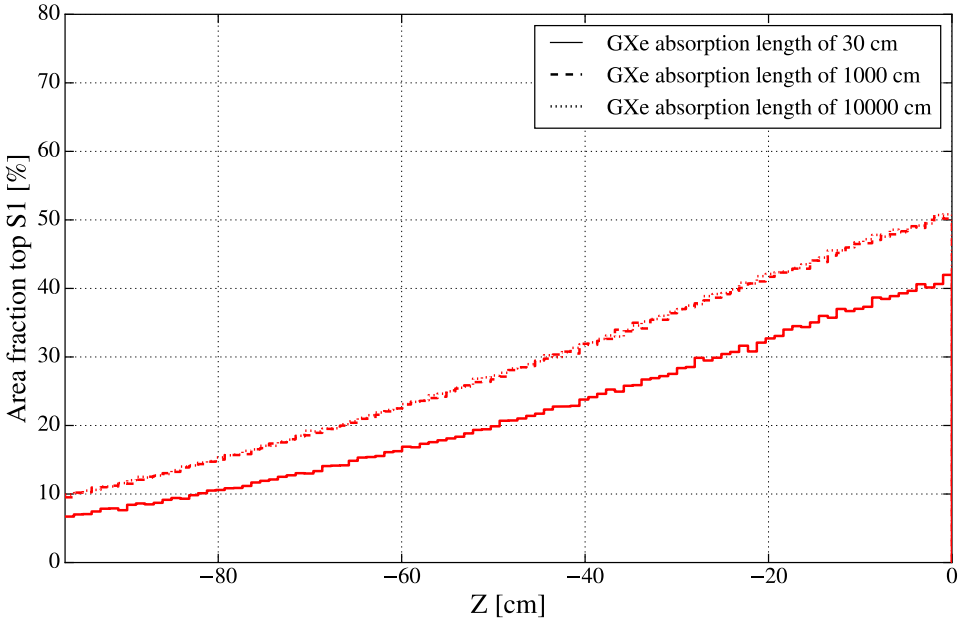

Figure A.8: Evolution of the AFT for S1 photons along the Z-position in the TPC.

A.2.4 Polytetrafluoroethylene reflectivity

The PTFE reflectivity can be adjusted in GEANT4 by the messenger functions */Xe/detector/setTeflonReflectivity* and */Xe/detector/setGXeTeflonReflectivity*. The following figures show the evolution of the LCE and AFT along the Z-position for a selection of parameter values.

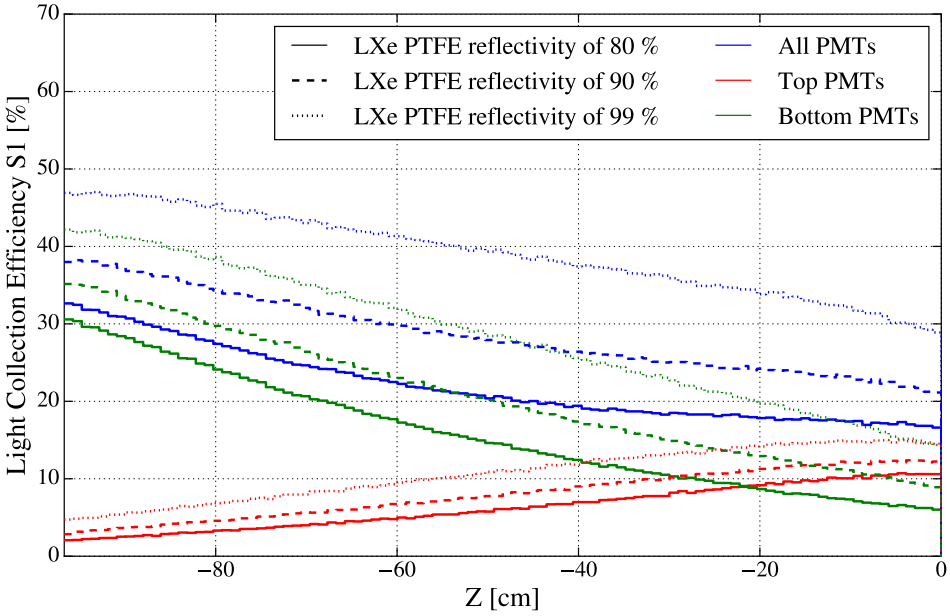

Figure A.9: Evolution of the LCE for S1 photons along the Z-position in the TPC.

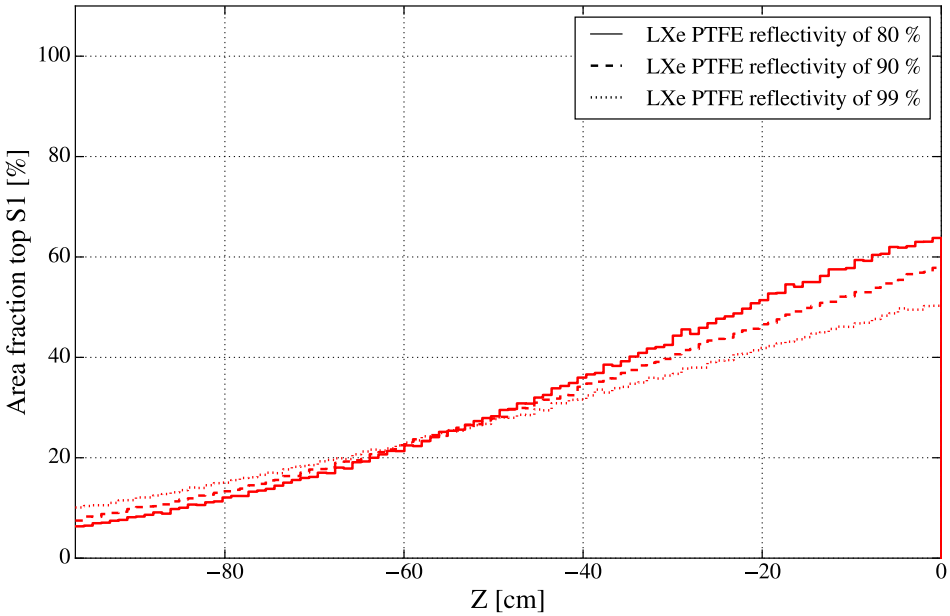

Figure A.10: Evolution of the AFT for S1 photons along the Z-position in the TPC.

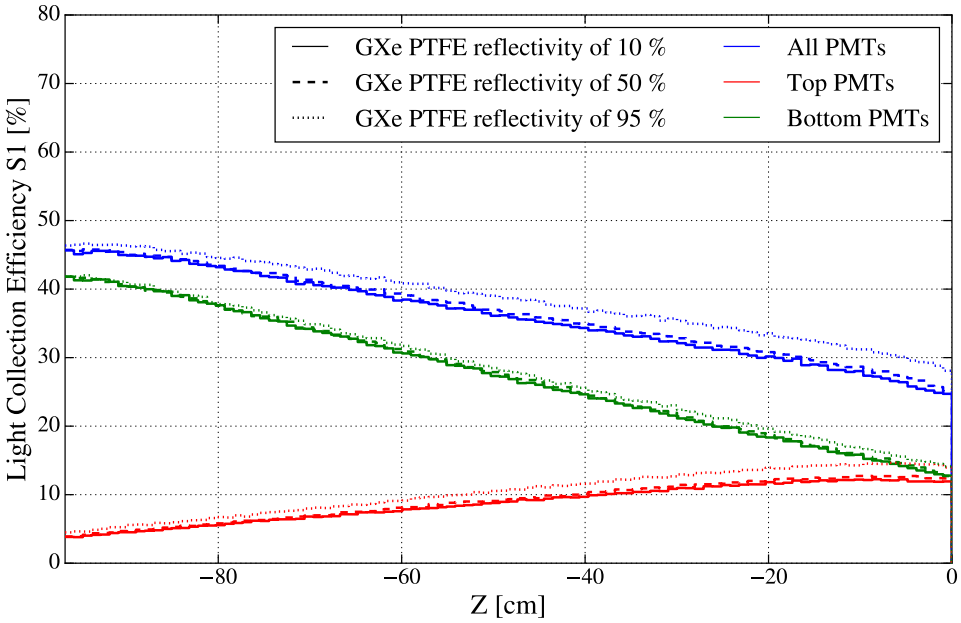

Figure A.11: Evolution of the LCE for S1 photons along the Z-position in the TPC.

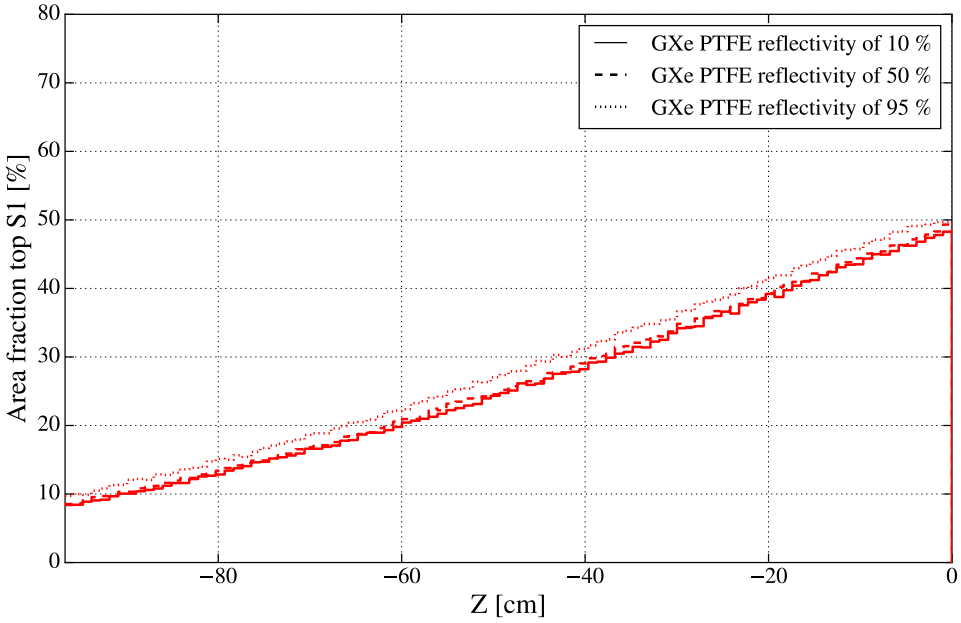

Figure A.12: Evolution of the AFT for S1 photons along the Z-position in the TPC.

A.3 Corrected optical photon simulations

The PMT hits fraction of S1 and S2 simulations strongly depends on the optical parameter settings used for the simulation production and applied PMT corrections. While figures 4.13 and 4.14 uses the fitted optical parameter setting obtained in table 5.1, shows figure A.13 the hits fraction from a simulation with the initial parameter assumptions (see [37]). The maximum fraction of PMT hits seen by the top PMT array is increased by 16 % and the minimum fraction by 10 %. The fraction of PMT hits in figure A.14 is corrected by the QE as in figure 5.2, a QE increase of 10 % and a CE of 90 %.

List of PMTs excluded because the HV is turned off: 1, 2, 12, 26, 34, 62, 65, 79, 86, 88, 102, 118, 130, 134, 135, 139, 148, 150, 152, 162, 178, 183, 190, 198, 206, 213, 214, 234, 239, 244 (29 PMTs).

List of PMTs excluded because of low single photoelectron acceptance: 27, 73, 91, 137, 167, 203 (6 PMTs).

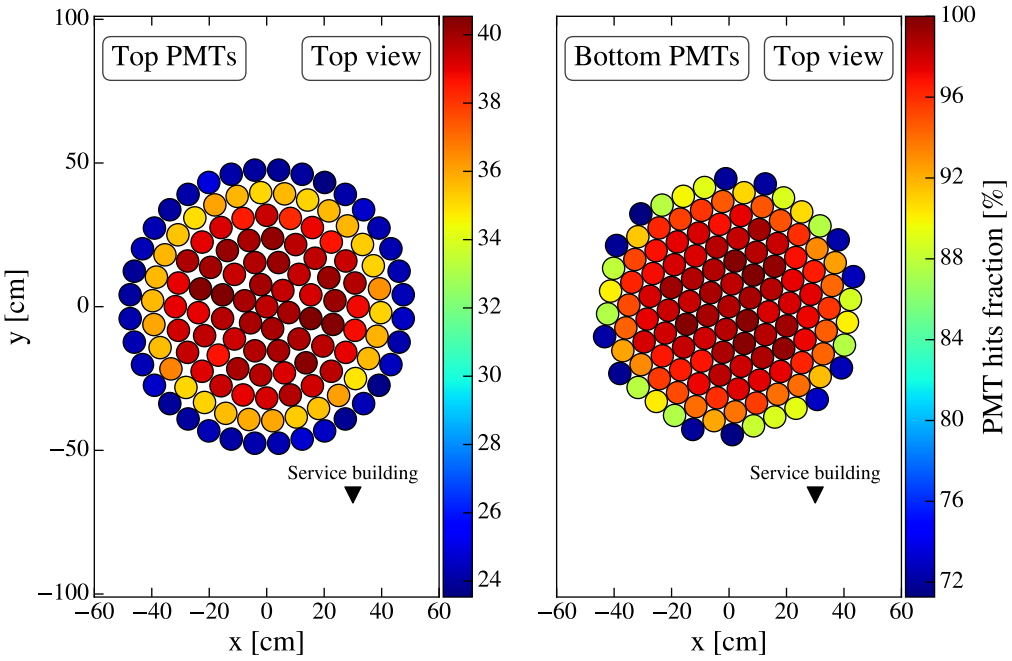

Figure A.13: Fraction of S1 light or photons seen by each PMT for the top and bottom PMT array normalized to the PMT which sees the most photons. Generated with the optical parameter settings of [37] without PMT corrections.

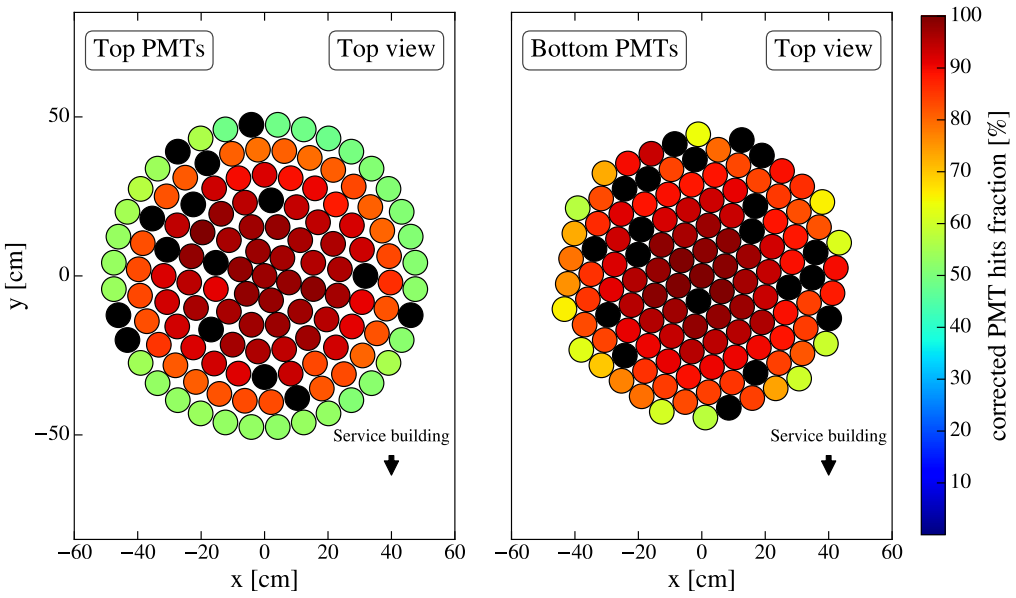

Figure A.14: Fraction of S1 photons seen by each PMT normalized to the PMT which sees the most photons (MC version 1.0.0 with optical settings of [37]). The amount of detected photons is corrected by several PMT effects.

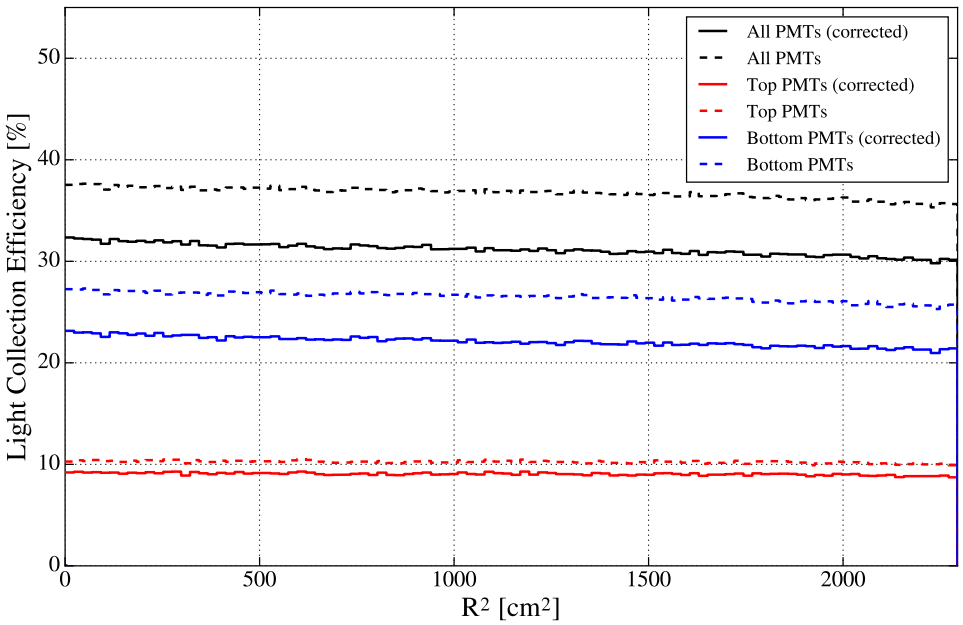

Figure A.15: LCE obtained along R^2-positions inside the TPC where $R^2 = 0$ corresponds to the middle of the TPC. Dashed lines indicates a LCE with *perfect* PMTs and solid lines for PMTs including the described correction (QE,CE and excluded PMTs).

A.4 Optical observables from ^{83m}Kr measurements

Optical observables used for matching with MC simulations are obtained from calibration measurements with ^{83m}Kr. The data selection used contains 282 datasets from eleven ^{83m}Kr calibrations during *ScienceRun_1* of XENON1T with an average *ly* of 8.07 pe/keV, excluding 35 PMTs (figure 5.2). The datasets are processed with PAX 6.6.5 using the included *DoubleScatter* analysis tools. The $S1_a$ *ly*, $S1_a$ AFT and S2 AFT are extracted using Gaussian fits for each slice along the Z-position, as seen in the following figures. Other observables like the fraction of light seen by the bottom PMT array or the rLCE can be directly calculated from the obtained values. Additionally, maps for the full TPC volume are extracted to quantify the evolution of the observable along the TPC radius during matching with simulation.

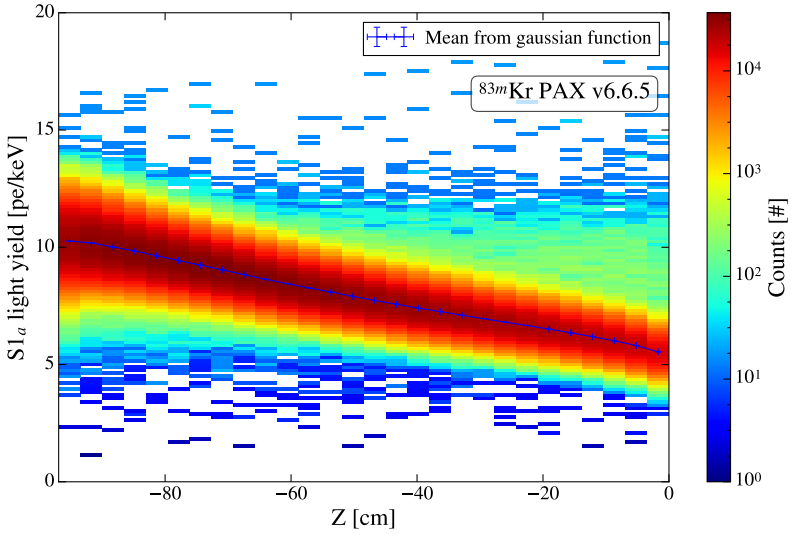

Figure A.16: Fit of the $S1_a$ *ly* along the Z-position inside the TPC for ^{83m}Kr.

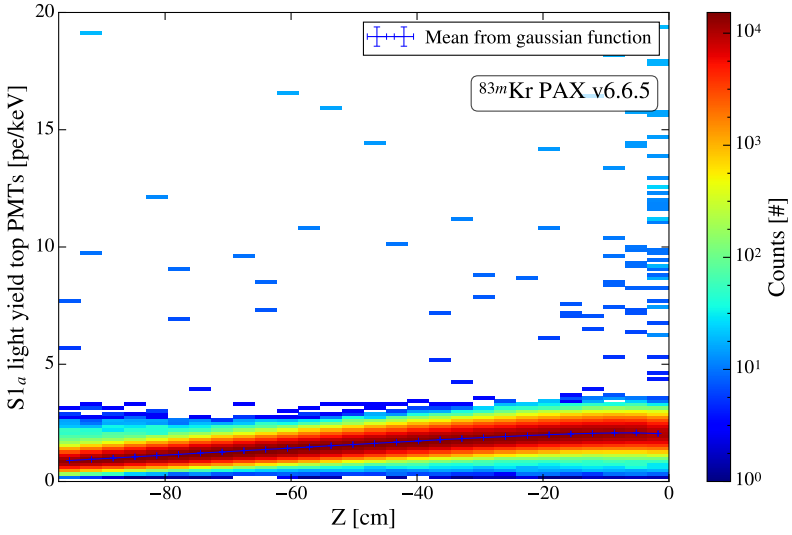

Figure A.17: Fit of the $S1_a$ *ly* for top PMTs along the Z-position inside the TPC for ^{83m}Kr.

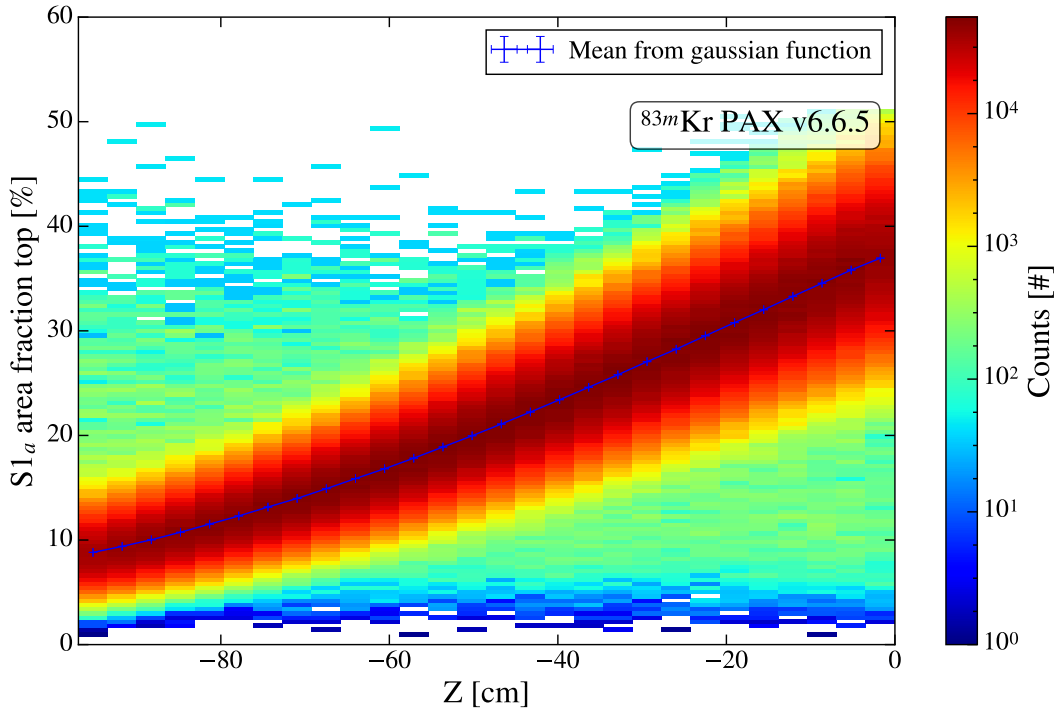

Figure A.18: Fit of the $S1_a$ AFT along the Z-position inside the TPC for ^{83m}Kr.

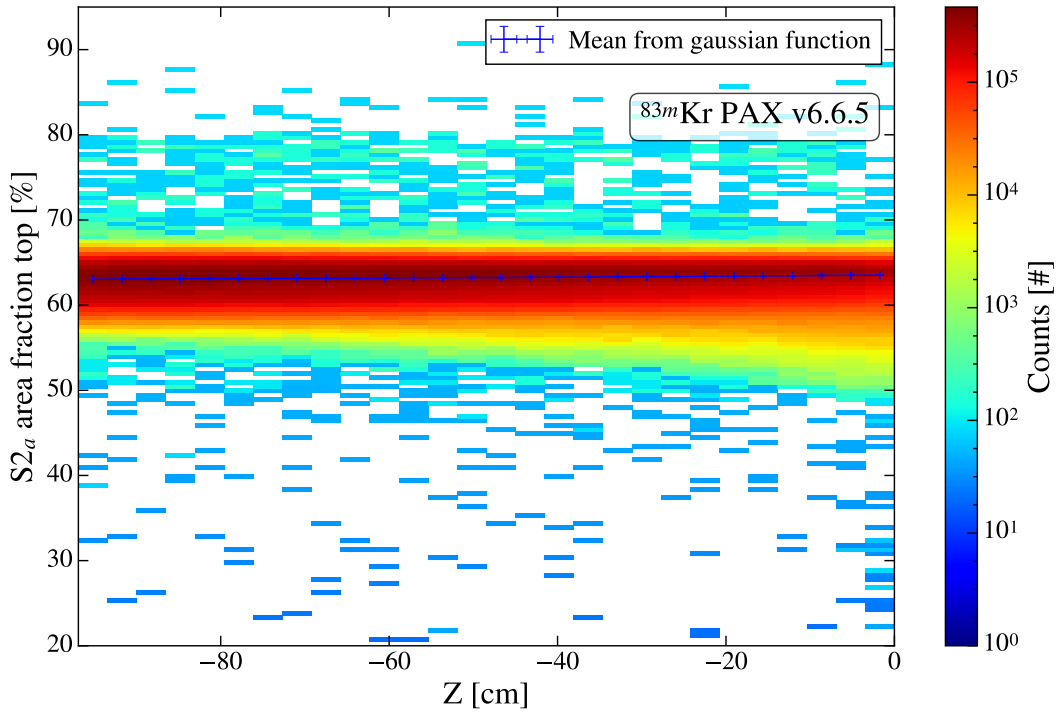

Figure A.19: Fit of the $S2_a$ AFT along the Z-position inside the TPC for ^{83m}Kr.

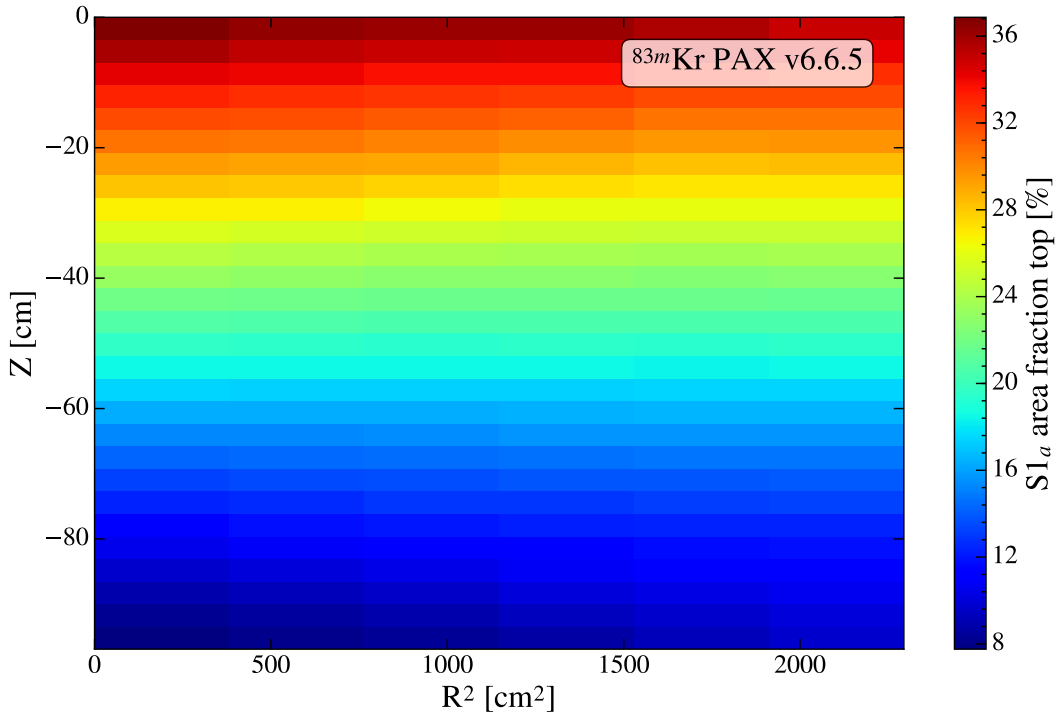

Figure A.20: AFT map derived from the $S1_a$ signal.

A.5 The XENON1T Monte Carlo chain

A.5.1 Per-PMT maps for S1 photons

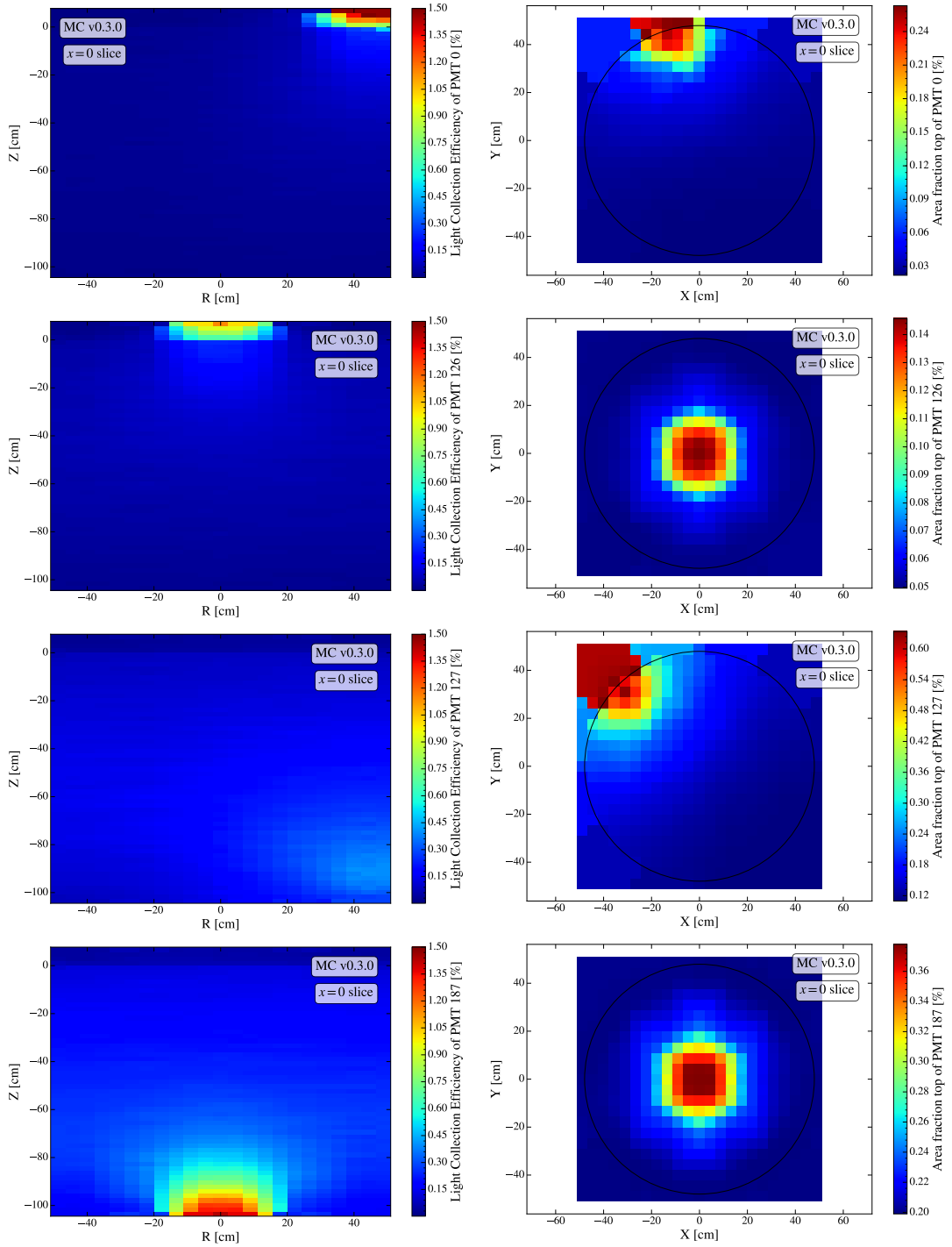

Figure A.21: LCE and AFT maps for PMT 0, 126, 127 and 187.

A.5.2 Per-PMT maps for S2 photons

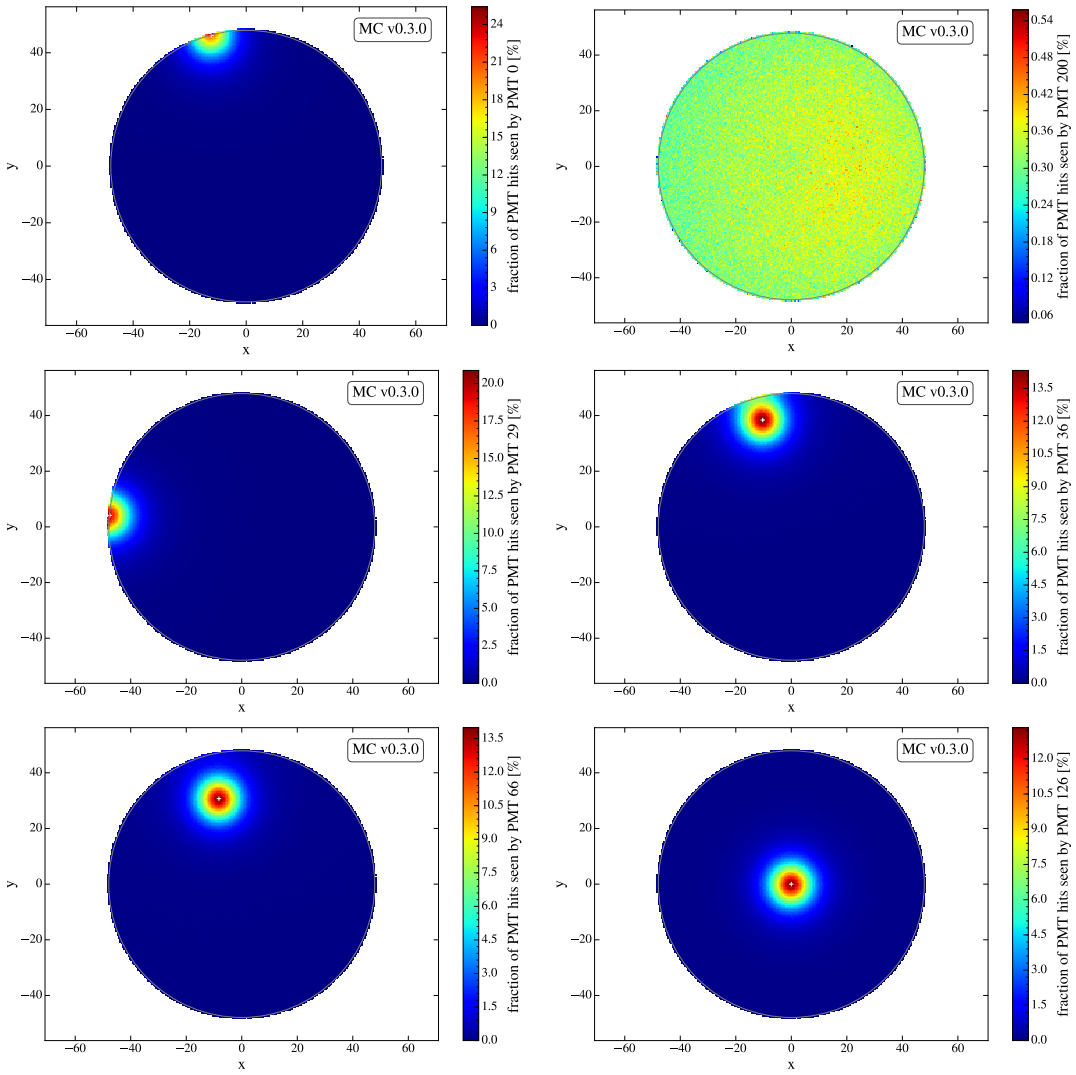

Figure A.22: AFT maps for PMT 0, 200, 29, 36, 66 and 126.

A.5.3 Full Monte Carlo chain ^{83m}Kr simulation performance

A direct comparison of ^{83m}Kr data measurements and MC simulations is necessary to estimate the performance of the simulation and to detect observables that needs further tuning. The discussion in section 6.2 uses ^{83m}Kr data from 282 datasets recorded in eleven calibrations during *ScienceRun_1* of XENON1T. The datasets are processed with PAX 6.6.5 using the included *DoubleScatter* analysis tools. The cuts used to select only ^{83m}Kr events and some additional comparisons are given within this section.

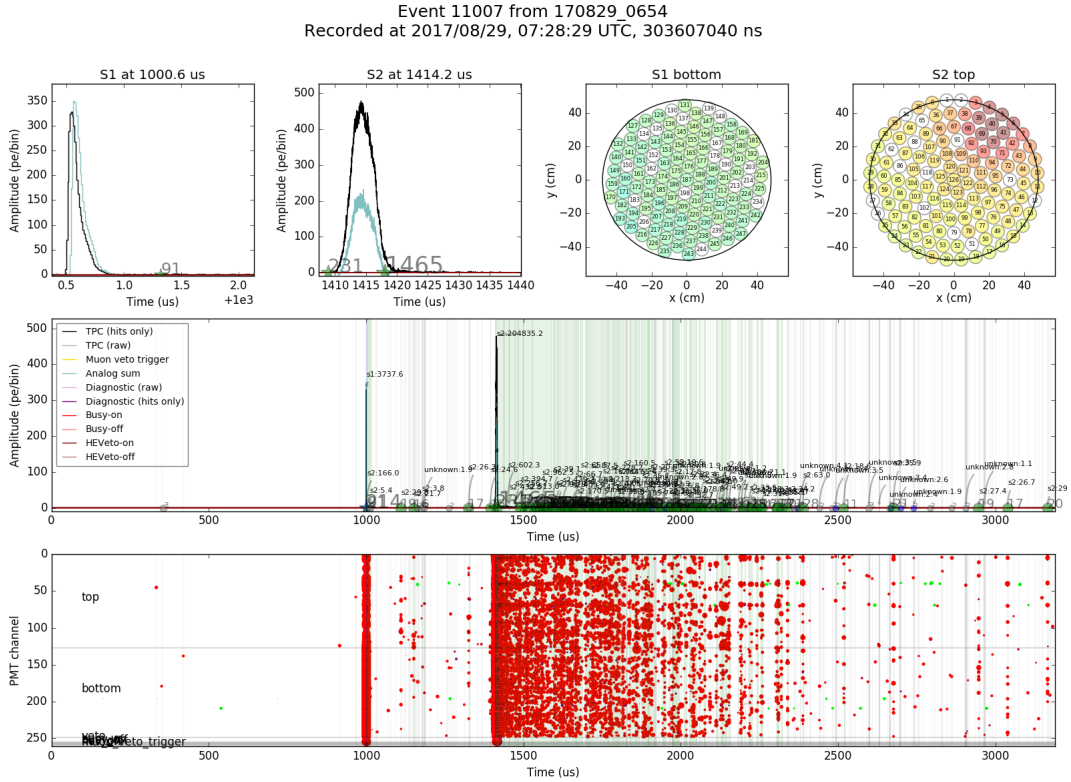

Figure A.23: Example waveform of ^{83m}Kr calibration in XENON1T using PAX version 6.6.5. The corresponding simulated waveform is given in figure 6.7.

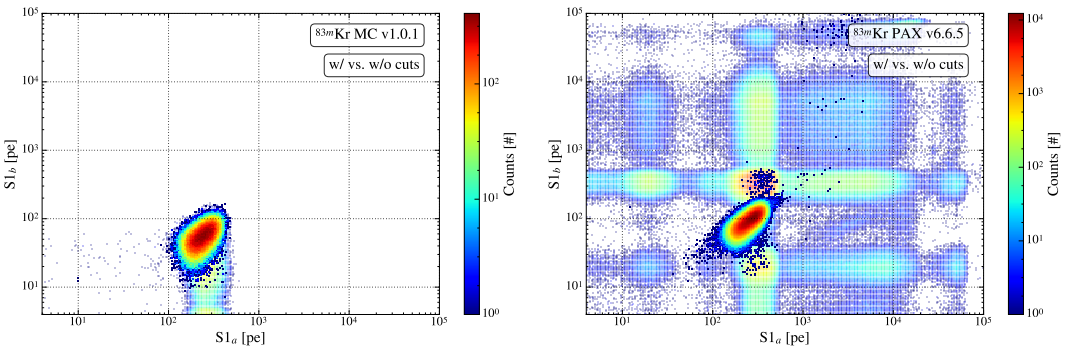

Figure A.24: Selection of ^{83m}Kr events for MC (left) and actual data (right) after applying the cuts discussed in figures A.25 to A.27.

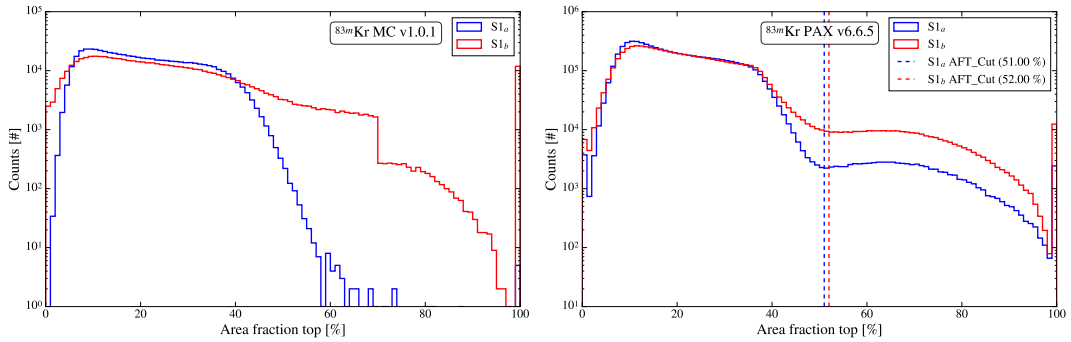

Figure A.25: Distribution of the AFT for MC (left) and actual data (right) divided in $S1_a$ (blue) and $S1_b$ (red). A cut of all events with an AFT higher than the first minimum is applied to remove gas events, that have a very high AFT value. This cut can be neglected for MC simulation, since that there are no gas events simulated.

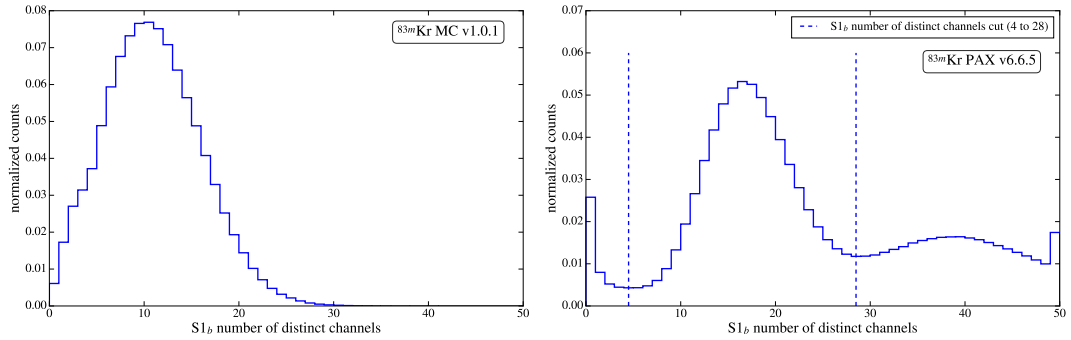

Figure A.26: Distribution of $S1_b$ number of distinct channels for MC (left) and actual data (right). A cut of all events with low and high number of distinct channels removes triggered afterpulses. The total number of events that are cutted is low, since that afterpulses must be triggered by an initial signal.

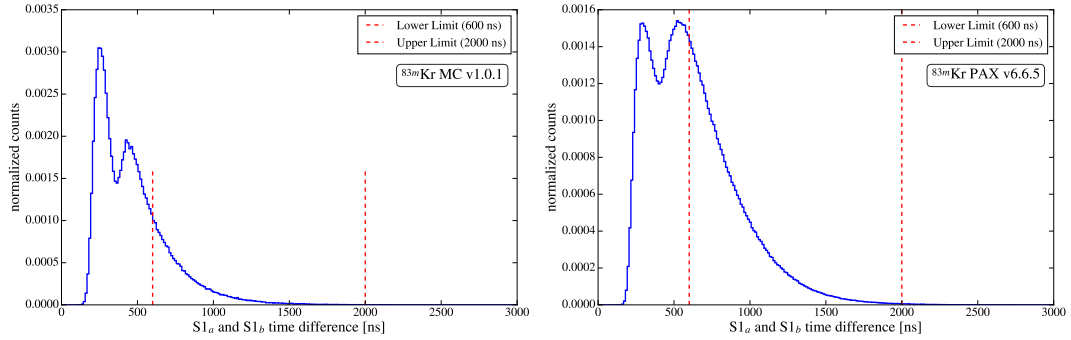

Figure A.27: Time difference of the $S1_a$ and $S1_b$ signal. Events with a difference lower than 600 ns are not correctly separated by PAX.

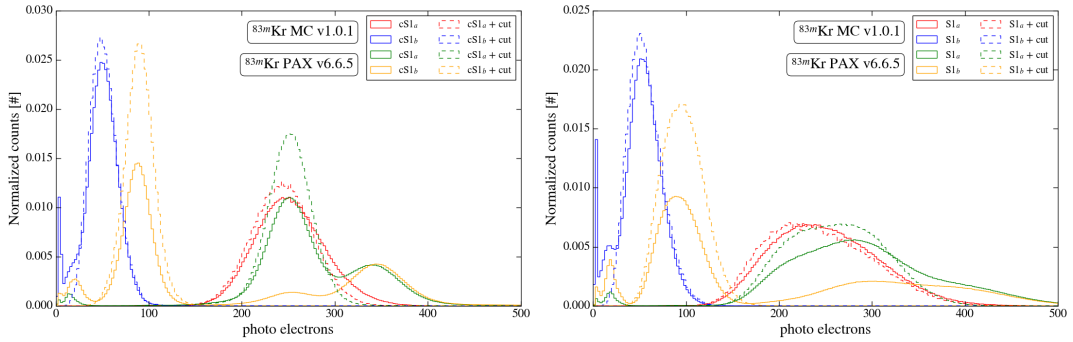

Figure A.28: Spectra of the S1 signals in photo electrons before and after cuts, as well as before and after energy correction.

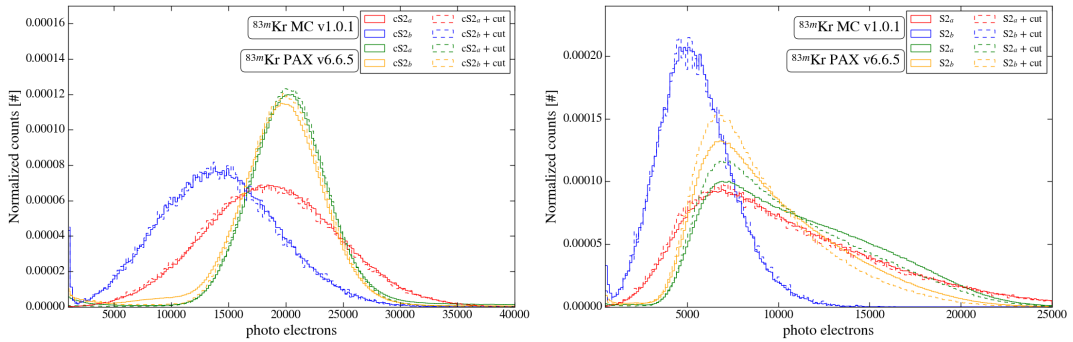

Figure A.29: Spectra of the S2 signals in photo electrons before and after cuts, as well as before and after energy correction.

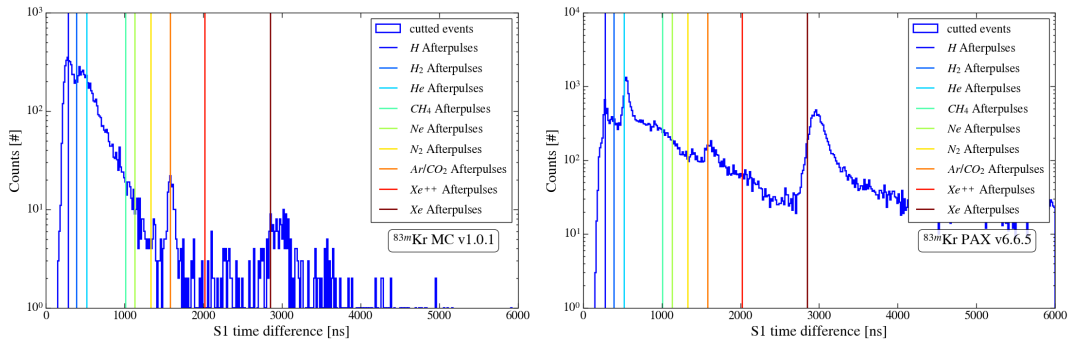

Figure A.30: Afterpulses cutted by the cut in figure A.26.

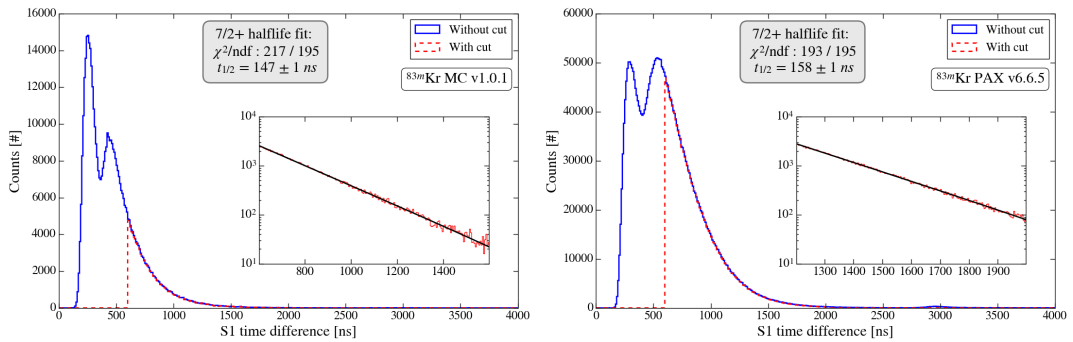

Figure A.31: Fit of the ^{83m}Kr half life for MC (left) and actual data (right).

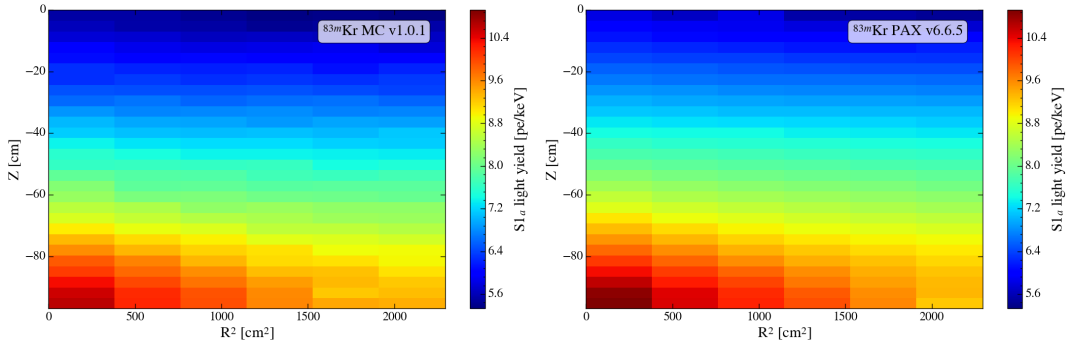

Figure A.32: Map of the $S1_a$ *ly* inside the TPC from MC (left) and actual data (right).

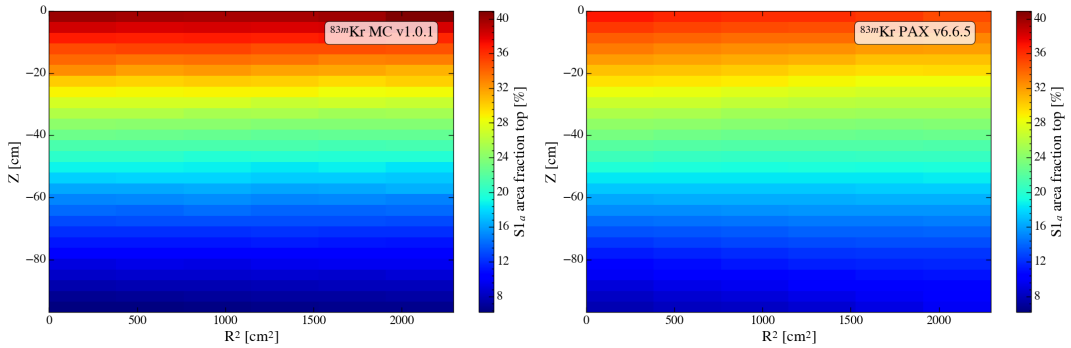

Figure A.33: Map of the $S1_a$ AFT inside the TPC from MC (left) and actual data (right).

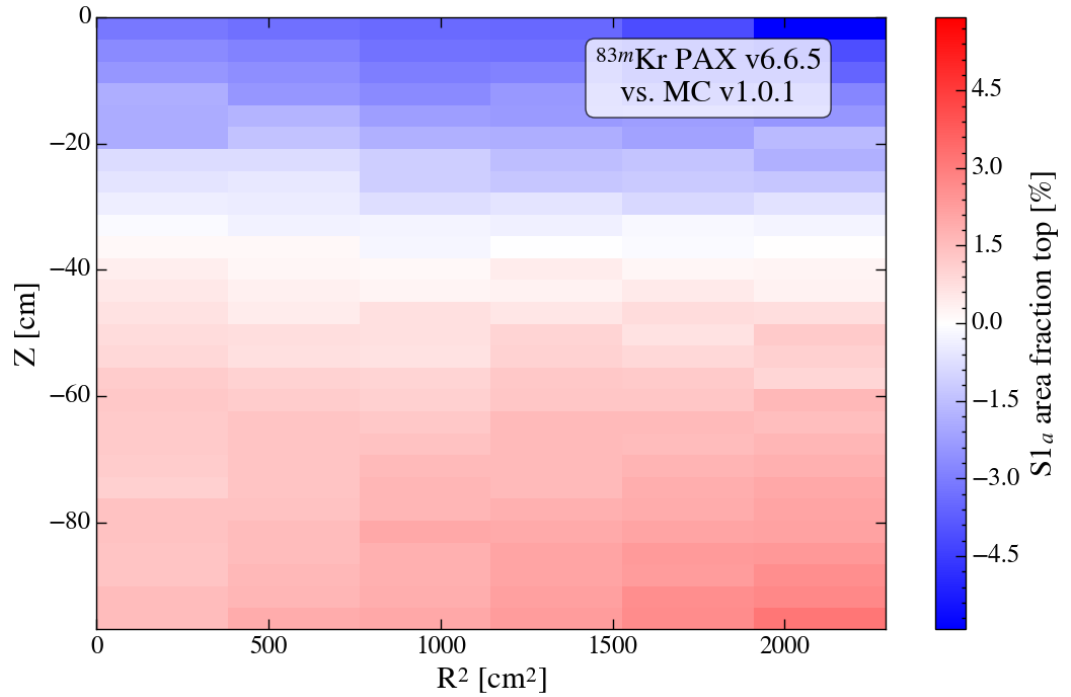

Figure A.34: Map of the $S1_a$ AFT difference inside the TPC from MC (left) and actual data (right).

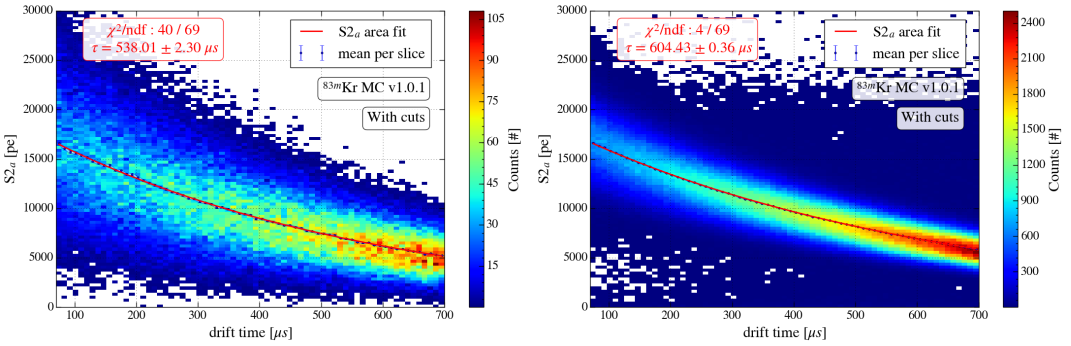

Figure A.35: Fit of the electron lifetime for MC (left) and actual data (right). The lifetime is set to 550 µs in the MC and changes over time in the XENON1T experiment.

A.6 Advanced S2 optical photon simulations

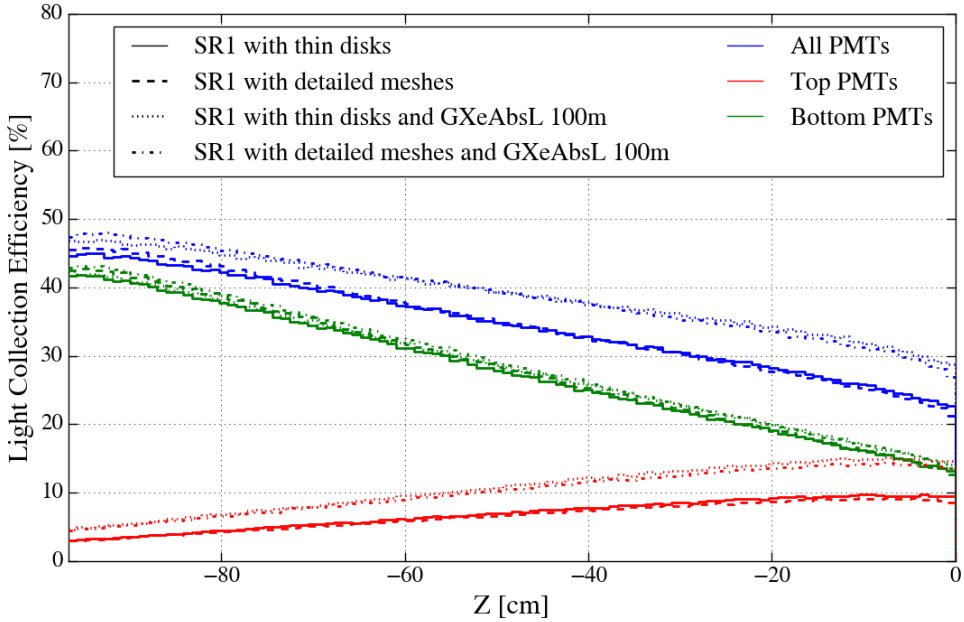

Figure A.36: Evolution of the LCE along the Z-position inside the TPC for different mesh geometry configuration in the MC simulation.

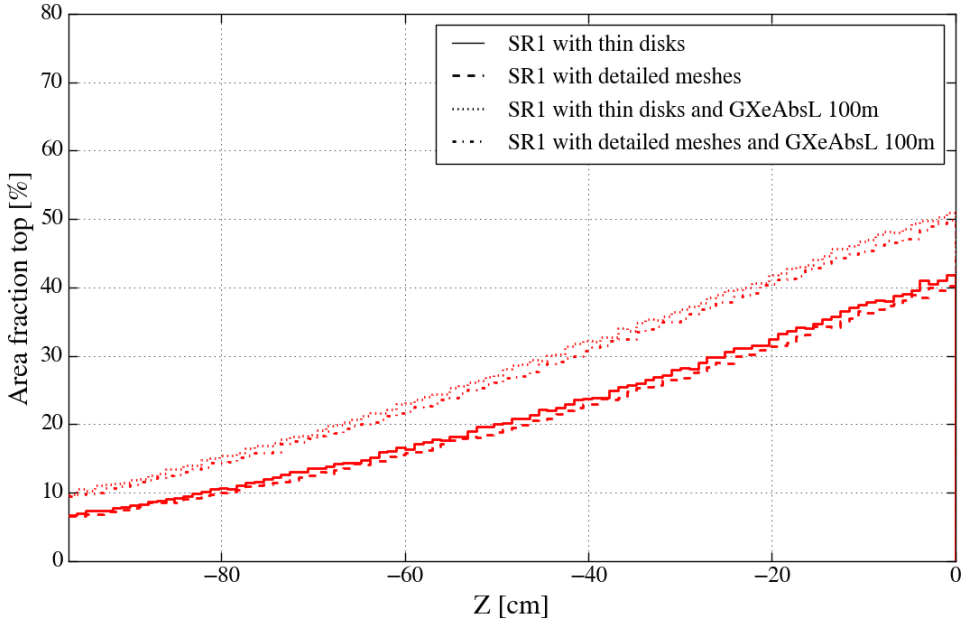

Figure A.37: Evolution of the AFT along the Z-position inside the TPC for different mesh geometry configuration in the MC simulation.

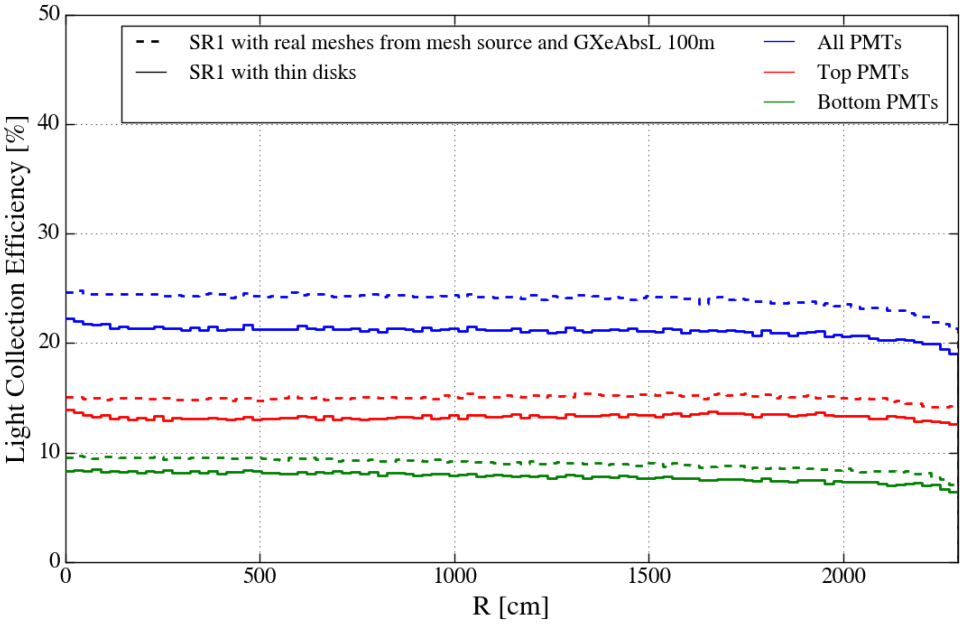

Figure A.38: Direct LCE comparison of the simulation with thin disk photon generation volume, thin disk meshes and a GXe absorption length of 20 cm against the simulation with detailed meshes, photons generated from a mesh like volume and a GXe absorption length of 100 m.

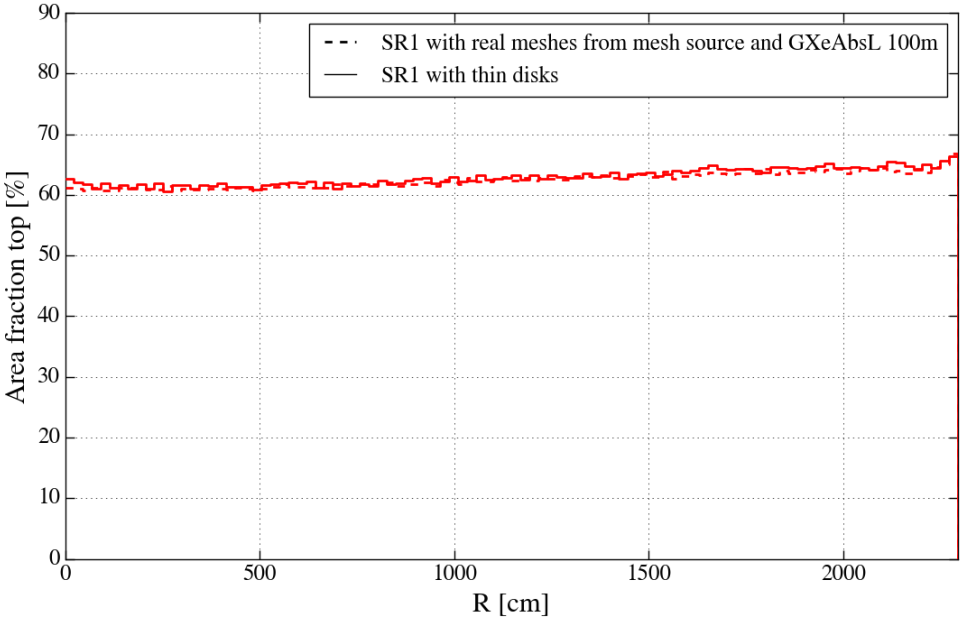

Figure A.39: Direct AFT comparison of the simulation with thin disk photon generation volume, thin disk meshes and a GXe absorption length of 20 cm against the simulation with detailed meshes, photons generated from a mesh like volume and a GXe absorption length of 100 m.

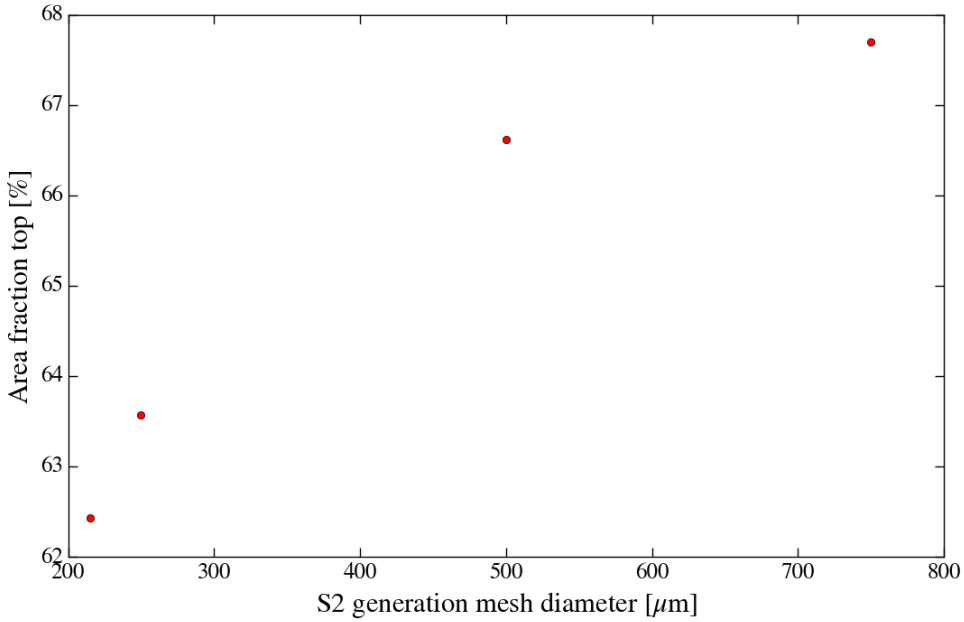

Figure A.40: Size of the S2 generation mesh diameter against the AFT value achieved by S2 simulations.

List of abbreviations

WIMP	weakly interacting massive particle
CMB	cosmic microwave background
ΛCDM	Λ cold dark matter
LXe	liquid xenon
GXe	gaseous xenon
TPC	Time Projection Chamber
LNGS	Laboratori Nazionali del Gran Sasso
VUV	vacuum ultraviolet
FWHM	Full width at half maximum
OFHC	oxygen-free high thermal conductivity
PTFE	polytetrafluoroethylene
PMT	photomultiplier tube
SS	stainless steel
MC	Monte Carlo
GEANT4	Geometry and Tracking
QE	quantum efficiency
CE	collection efficiency
LCE	Light Collection Efficiency
AFT	area fraction top
ly	light yield
NEST	Noble Element Simulation Technique
PAX	Processor for Analyzing XENON
HAX	Handy Analysis for XENON
ADC	analog-to-digital converter
rLCE	relative Light Collection Efficiency
RMSD	root-mean-square deviation
FAX	FAke Xenon experiment

Bibliography

[1] Y. Yang and W. B. Yeung. A Yang-Mills Type Gauge Theory of Gravity and the Dark Matter and Dark Energy Problems. 2012. 3

[2] J. C. Kapteyn. First Attempt at a Theory of the Arrangement and Motion of the Sidereal System. *Astrophys. J*, 55:302–328, 1922. 3

[3] J. H. Oort. The force exerted by the stellar system in the direction perpendicular to the galactic plane and some related problems. *Bulletin of the Astronomical Institutes of the Netherlands*, 6:249, 1932. 3

[4] F. Zwicky. Die Rotverschiebung von extragalaktischen Nebeln. *Helv. Phys. Acta*, 6:110–127, 1933. 3

[5] V. C. Rubin, N. Thonnard, and J. Ford. Extended rotation curves of high-luminosity spiral galaxies. *Astrophys. J*, 1978. 4

[6] ESA/Hubble. 1es 0657-55.8, 2012. 4

[7] F. Zwicky. Nebulae as Gravitational lenses. *Physical Review*, 54, 1937. 4

[8] D. Clowe et al. A Direct Empirical Proof of the Existence of Dark Matter. *The Astrophysical Journal Letters*, 648(2):L109, 2006. 5

[9] G. Hinshaw et al. Nine-year Wilkinson Microwave Anisotropy Probe (WMAP) Observations: Cosmological Parameter Results. *Astrophys. J. Suppl.*, 2013. 5

[10] P. A. R. Ade et al. Planck 2015 results. XIII. Cosmological parameters. *Astron. Astrophys.*, 2016. 5, 6

[11] S. Dodelson and L. M. Widrow. Sterile neutrinos as dark matter. *Physical Review Letters*, 1994. 6

[12] L. Covi, H. B. Kim, J. E. Kim, and L. Roszkowski. Axinos as dark matter. *Journal of High Energy Physics*, 2001(05):033, 2001. 6

[13] L. Bergström. Non-baryonic dark matter: observational evidence and detection methods. *Rep. Prog. Phys.*, 2000. 6

[14] T. M. Undagoitia and L. Rauch. Dark matter direct-detection experiments. 2015. 6, 7

[15] J. Lewin and P. Smith. Review of mathematics, numerical factors, and corrections for dark matter experiments based on elastic nuclear recoil. *Astropart. Phys.*, 1996. 7

[16] E. Aprile et al. The xenon1t dark matter experiment. *European Physical Journal C*, 2017. 9, 13, 26

[17] Gianfranco Bertone. *Particle Dark Matter: Observations, Models and Searches*. Cambridge: Cambridge Univ. Press, 2010. 11

[18] A. Hitachi, T. Doke, and A. Mozumder. Luminescence quenching in liquid argon under charged-particle impact: Relative scintillation yield at different linear energy transfers. *Physical Review B*, 1992. 11

[19] A. G. Manalaysay. Studies of the Scintillation and Ionization Properties of the Liquid Xenon for Dark Matter Detection. 2006. 11

[20] E. Aprile et al. The XENON100 dark matter experiment. *Astroparticle Physics*, 35:573–590, April 2012. 13, 22

[21] S. Agostinelli et al. Geant4 - a simulation toolkit. *Nuclear Instruments and Methods in Physics Research Section A: Accelerators, Spectrometers, Detectors and Associated Equipment*, 506(3):250 – 303, 2003. 16

[22] R. K. Kirby. Thermal expansion of polytetrafluoroethylene (teflon) from -190 to +300 °C. *Journal of Research of the National Bureau of Standards, vol. 57, no. 2, pp. 91–94*, 1956. 18

[23] J. Jortner, L. Meyer, S. A. Rice, and E. G. Wilson. Localized excitations in condensed Ne, Ar, Kr, and Xe. *The Journal of Chemical Physics, vol. 42, no. 12, pp. 4250–4253*, 1965. 19

[24] C. Levy. *Light Propagation and Reflection off Teflon in Liquid Xenon Detectors for the XENON100 and XENON1T Dark Matter Experiments*. PhD thesis, 2014. 19, 20

[25] E. Aprile et al. Material screening and selection for XENON100. *Astroparticle Physics, vol. 35, no. 2, pp. 43 – 49*, 2011. 19

[26] D. Akerib et al. Radiogenic and muon-induced backgrounds in the LUX dark matter detector. *Astroparticle Physics, vol. 62, pp. 33 – 46*, 2015. 19

[27] K. Poole and M. Michaelis. Hialvac and Teflon outgassing under ultra-high vacuum conditions. *Vacuum, vol. 30, no. 10, pp. 415 – 417*, 1980. 19

[28] M. Yamashita, T. Doke, K. Kawasaki, J. Kikuchi, and S. Suzuki. Scintillation response of liquid Xe surrounded by PTFE reflector for gamma rays. *Nucl. Instrum. Meth., vol. A535, no. 3, pp. 692 – 698*, 2004. 19

[29] F. Neves et al. Performance of a chamber for studying the liquid xenon response to gamma-rays and nuclear recoils. *IEEE Transactions on Nuclear Science, vol. 52, no. 6, pp. 2793–2800*, 2005. 19

[30] F. Neves et al. Measurement of the absolute reflectance of polytetrafluoroethylene (PTFE) immersed in liquid xenon. *Journal of Instrumentation*, 2016. 19, 20

[31] M. Janecek. Simulating scintillator light collection using measured optical reflectance. *IEEE Transactions on Nuclear Science*, 2010. 20

[32] F. V. Massoli. *The XENON1T experiment: Monte Carlo background estimation and sensitivity curves study.* PhD thesis, University of Bologna, 2016. 23

[33] P. Barrow et al. Qualification tests of the r11410-21 photomultiplier tubes for the xenon1t detector. *Journal of Instrumentation*, 2016. 26, 27

[34] K. Lung et al. Characterization of the Hamamatsu R11410-10 3-Inch Photomultiplier Tube for Liquid Xenon Dark Matter Direct Detection Experiments. *Nuclear Instruments and Methods in Physics*, 2012. 27

[35] A. Lyashenko, T. Nguyen, A. Snyder, H. Wang, and K. Arisaka. Measurement of the absolute Quantum Efficiency of Hamamatsu model R11410-10 photomultiplier tubes at low temperatures down to liquid xenon boiling point. *Journal of Instrumentation*, 2014. 27, 44

[36] M. Szydagis, A. Fyhrie, D. Thorngren, and M. Tripathi. Enhancement of nest capabilities for simulating low-energy recoils in liquid xenon. *Journal of Instrumentation*, 8(10):C10003, 2013. 28, 57

[37] E. Aprile et al. Physics reach of the XENON1T dark matter experiment. *Journal of Cosmology and Astroparticle Physics*, 2015. 30, 31, 32, 34, 36, 39, 43, 44, 45, 54, 62, 72, 78, 85, 86

[38] I. Malitson. Interspecimen comparison of the refractive index of fused silica. *JOSA 55*, 1965. 31

[39] R. Kitamura, L. Pilon and M. Jonasz. Optical constants of silica glass from extreme ultraviolet to far infrared at near room temperature. *Appl. Opt. 46*, 2007. 31

[40] L. Barkov, A. Grebenyuk, N. Ryskulov, P. Y. Stepanov and S. Zverev. Measurement of the refractive index of liquid xenon for intrinsic scintillation light. *Nucl. Instrum. Meth.*, 1996. 32, 54

[41] V. Solovov, V. Chepel, M. Lopes and A. Hitachi. Measurement of the refractive index and attenuation length of liquid xenon for its scintillation light. *Nucl. Instrum. Meth.*, 2004. 32, 34, 54

[42] G. M. Seidel and R. E. Lanou and W. Yao. Rayleigh Scattering in Rare Gas Liquids. *Nucl. Instrum. Meth.*, 2002. 34, 35

[43] A. Braem et al. Observation of the UV scintillation light from high-energy electron showers in liquid xenon. *Nucl. Instrum. Meth.*, 1992. 34

[44] V. Y. Chepel, M. Lopes, R. F. Marques and A. Policarpo. Purification of liquid xenon and impurity monitoring for a PET detector. *Nucl. Instrum. Meth.*, 1994. 34

[45] V. Chepel and H. Araújo. Liquid noble gas detectors for low energy particle physics. *Journal of Instrumentation*, 2013. 36

[46] V. Hannen et al. Limits on the release of rb isotopes from a zeolite based 83m kr calibration source for the xenon project. *Journal of Instrumentation*, 6(10):P10013, 2011. 47

[47] A. Manalaysay et al. Spatially uniform calibration of a liquid xenon detector at low energies using 83m-Kr. 2009. 47

[48] Processor for Analyzing XENON. http://xenon1t.github.io/pax. 47, 48

[49] FAke Xenon experiment. http://xenon1t.github.io/pax/simulator.html. 57

[50] R. F. Lang et al. Characterization of a deuterium-deuterium plasma fusion neutron generator. 2017. 62

[51] Comsol. https://www.comsol.com/comsol-multiphysics. 69